SYNTHESIS AND CHARACTERIZATION OF NANOPOROUS MATERIALS AND THEIR FILMS WITH CONTROLLED MICROSTRUCTURE

A Dissertation

by

IN HO LEE

Submitted to the Office of Graduate Studies of
Texas A&M University
in partial fulfillment of the requirements for the degree of

DOCTOR OF PHILOSOPHY

August 2010

Major Subject: Chemical Engineering

Synthesis and Characterization of Nanoporous Materials and Their Films with Controlled Microstructure

SYNTHESIS AND CHARACTERIZATION OF NANOPOROUS MATERIALS AND THEIR FILMS WITH CONTROLLED MICROSTRUCTURE

A Dissertation

by

IN HO LEE

Submitted to the Office of Graduate Studies of
Texas A&M University
in partial fulfillment of the requirements for the degree of

DOCTOR OF PHILOSOPHY

Approved by:

Chair of Committee,	Hae-Kwon Jeong
Committee Members,	Daniel F. Shantz
	Zhengdong Cheng
	Hongcai (Joe) Zhou
Head of Department,	Michael Pishko

August 2010

Major Subject: Chemical Engineering

ABSTRACT

Synthesis and Characterization of Nanoporous Materials and Their Films with Controlled Microstructure. (August 2010)

In Ho Lee, B.S., Sogang University; M.S., Sogang University

Chair of Advisory Committee: Dr. Hae-Kwon Jeong

Nanoporous materials have attracted tremendous interest, investment and effort in research and development due to their potential applications in various areas such as membranes, catalysis, sensors, delivery, and micro devices. Controlling a nanoporous material's microstructure is of great interest due to the strong influence on efficiency and performance. For particles, microstructure refers to particle size, shape, surface morphology, and composition. When discussing thin films, microstructure includes film thickness, crystal orientation and grain boundaries. In this respect, we focus to develop novel methods for the synthesis and characterization of nanoporous materials and their films, which are capable of controlling the microstructure of material. This dissertation is composed of two main sections and each explores the fabrication of a different nanoporous material: 1) A simple fabrication method for producing oriented MFI zeolite membranes with controlled thickness, orientation, and grain boundary; 2) A microfluidic synthesis of ordered mesoporous silica particles with controllable size, shape, surface morphology, and composition.

The first section of this dissertation demonstrates a simple and commercially viable method termed the micro-tiles-and-mortar method to make continuous *b*-oriented MFI membranes with controlled membrane microstructure. This simple method allows for control of the thickness of the membrane by using plate-like seed crystals with different thicknesses along the *b*-axis (0.5 μm to 2.0 μm), as well as to manipulate the density and structure of grain boundaries. Microstructural effects of silicalite-1 membranes on the gas separation are investigated by measuring the permeation and separation for xylene isomers.

In the second section of this dissertation, a new synthesis method for the ordered mesoporous silica particles with controllable microstructure is demonstrated. This novel method combines a microfluidic emulsification technique and nonaqueous inorganic synthesis with a diffusion-induced self-assembly (DISA). The systematic control of the particle microstructure such as size, shape, and surface morphology is shown by adjusting microfluidic conditions.

To my loving wife Soeun, daughter Seohyun, and son Hyukjoon

ACKNOWLEDGEMENTS

I wish to express special thanks to my advisor Dr. Hae-Kwon Jeong for his guidance and support throughout the course of this research. Without his guidance and persistent help this dissertation would not have been possible. I would like to thank to my committee members, Dr. Daniel F. Shantz, Dr. Zhengdong Cheng, and Dr. Hongcai (Joe) Zhou. Their valuable comments and suggestions have been dissolved in this dissertation to make better scientific work. I wish to thank to Dr. Dawei Lou and Dr. Jeongyun Kim for their help on fabrication of microfluidic device. I also thank my colleagues Yeonshick, Colin, and Victor in the Jeong group for their help, advice, and collaborations.

Finally, I thank to my mother, father, and father-in-law for their encouragement and to my wife, Soeun, for her patience and love.

TABLE OF CONTENTS

CHAPTER Page

Page

LIST OF FIGURES

FIGURE Page

FIGURE Page

FIGURE Page

FIGURE Page

FIGURE Page

FIGURE Page

LIST OF TABLES

CHAPTER I

INTRODUCTION

1.1 Motivation and objectives

A major scientific and societal challenge of the 21st century is converting our major source of energy from fossil fuels to carbon-free renewable sources. In 2007, the average global power consumption was approximately 14 terawatts (TW), with more than 80% of this energy coming from carbon-dioxide emitting fossil fuels and less than 1% coming from carbon-free renewable power such as geothermal, wind, solar power, and biofuels.[1] If the power provided by fossil fuels remains at the current level of ~80%, the loading of CO_2 into the atmosphere will pose a grave environmental threat to human civilization.

Nanoporous materials such as zeolite and ordered mesoporous silica (OMS) have a great potential to help address this grand environmental challenge due to their unique properties, which include a high surface area to volume ratio, well-ordered pore structure, fluid permeability, and molecular sieving effects. For example, nanoporous materials are being used as catalysts and electrode materials, and they are being developed and tested for use in various areas such as hydrogen production, solar cells, fuel cells, and advanced batteries.[2] Despite the strong potential of nanoporous materials for energy and environmental technologies, there are still many challenges and opportunities ahead.

This dissertation follows the style of *Nano Letters.*

1.1.1 Nanoporous films: zeolite membranes

Zeolite membranes have attracted a great deal of research and particular commercial interest due to their potential energy-efficient alternatives to current processes of distillation, crystallization, and others. Despite the recent success of zeolite membranes as highly selective gas separation membranes,[3] several challenges such as poor reproducibility, high manufacturing cost, and no easy crack healing remain to be solved. The goal of this dissertation is to develop an innovative method that can address these challenges, specifically to rapidly prepare highly oriented submicron-thick zeolite membranes.

Due to the simplicity of its synthesis and its potential in the separation of light hydrocarbons such as xylene isomers, the structure-type MFI (also known as ZSM-5)[4] has attracted a great deal of interest as a model zeolite system for the development of a generalized membrane fabrication method.[5] The pore structure of MFI zeolites is shown in Figure 1.1. It has straight channels with an approximate pore opening of 0.56 nm × 0.54 nm along its b-axis and sinusoidal channels with an estimated pore opening of 0.51 nm × 0.55 nm along its a-axis. It has been demonstrated that *b*-oriented MFI membranes show superior performance for organic vapor separation because 1) straight channels along the *b*-axis allow to effectively enhance intercrystalline diffusion of molecules, and 2) *b*-oriented membranes have better grain structure which can reduce non-selective intracrystalline diffusion of molecules.[6]

To date, several groups have reported *b*-oriented ZSM-5 membranes by both *in situ* and secondary growth methods.[7-12] However, Lai et al. was the first to report the

permeation results for *b*-oriented MFI membranes which were prepared by a secondary growth (i.e. seeded growth) method.[6, 13] Compared to the selectivity of *c*- or *a/b*-oriented MFI membranes, the selectivity of *p*-xylene over *o*-xylene through *b*-oriented MFI membrane improved unprecedentedly at most to 450 as shown in Figure 1.2. In spite of the remarkable performance of their *b*-oriented MFI membranes, the complexity of their manufacturing process (i.e. time-consuming preparation steps and the need for organic template synthesis) makes it difficult to produce high performance *b*-oriented MFI membranes in a reproducible and cost-effective way for commercial application.

A simple synthesis method-termed as the micro-tiles-and-mortar method-that is commercially viable is demonstrated here to make continuous *b*-oriented MFI membranes with controlled grain boundaries. This method is analogous to a macroscopic tiling process, i.e. assembling tiles and jointing them with mortar. This method involves three main steps: 1) tiling of MFI micro-crystals on porous substrate by manual assembly, 2) passivating the out-of-plane crystal faces by metal sputtering, 3) filling the gap between crystals by secondary growth. The key feature of this method is to preserve the orientation of b-oriented seed crystals by passivating the flat crystal faces with a thin layer of a sputtered mixture of gold and palladium. This thin metal layer suppresses the nucleation and growth of crystals along the out-of-plane direction while allowing the growth of crystals along the in-plane direction. The micro-tiles-and-mortar method requires neither complicated steps nor custom-made organic templates. This enables us to reduce the membrane fabrication time from days to hours by simplifying seeding and secondary growth.

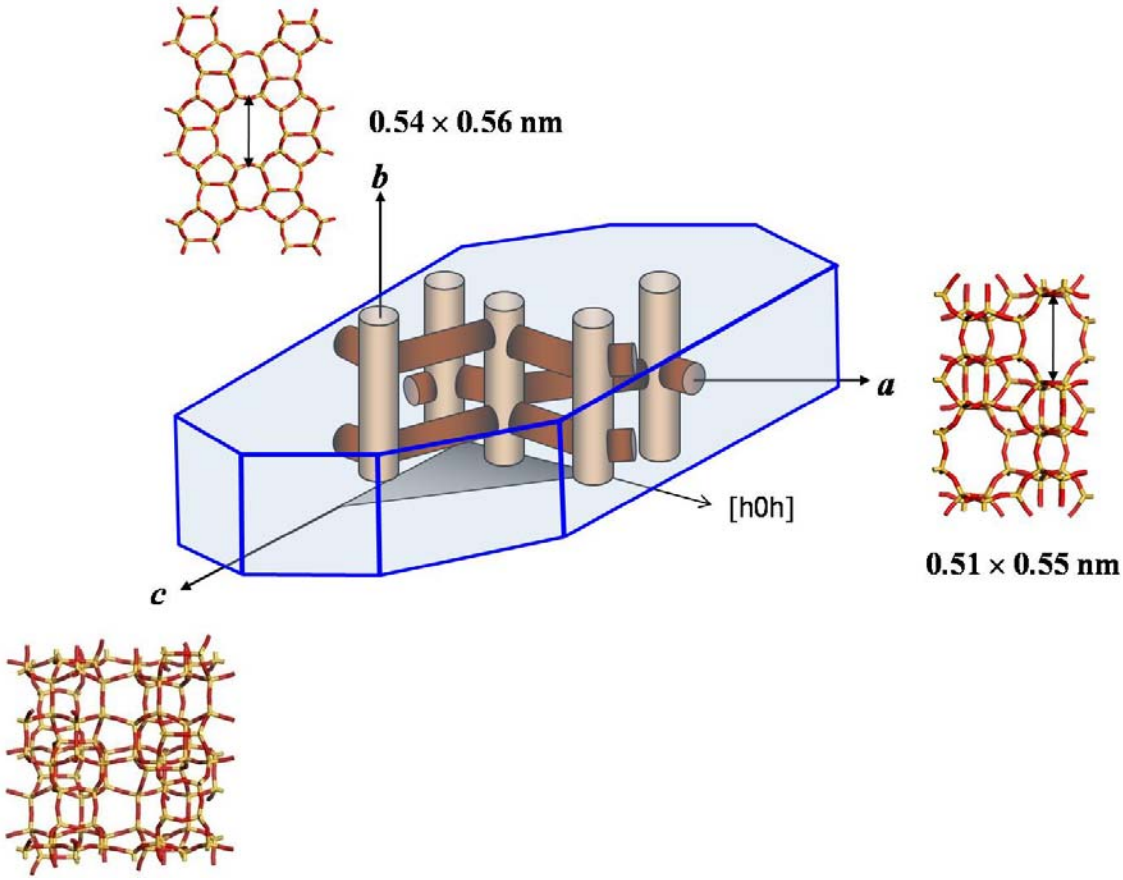

Figure 1.1 The pore structure of MFI zeolite

(a)

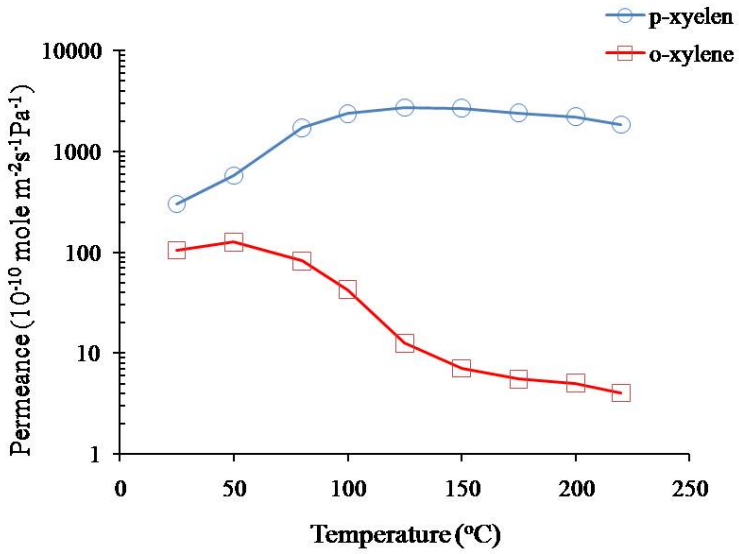

(b)

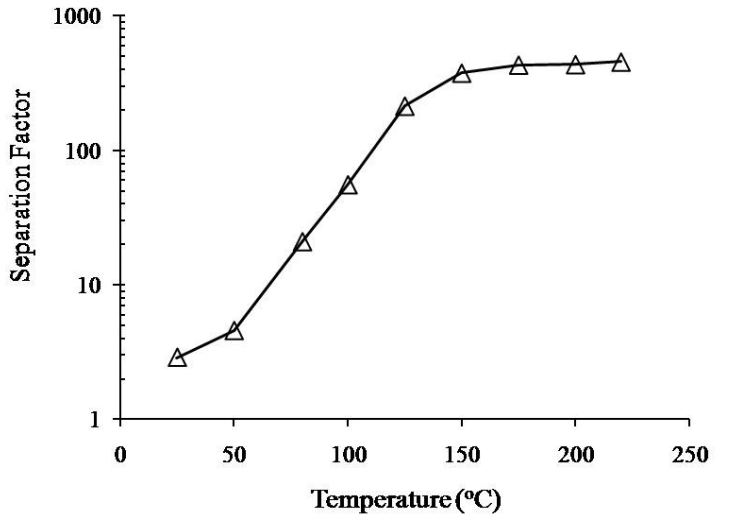

Figure 1.2 *b*-oriented ZSM-5 membrane performance in xylene isomer separation. (a) permeance of xylene isomers (b) separation factor. Adapted and slightly modified from Lai et al.[6]

1.1.2 Nanoporous materials: Ordered Mesoporous Silica (OMS) microspheres

Despite the promise and success of OMS spheres as nanoporous materials in conventional applications, which includes catalysis,[14] selective adsorption, separation,[15, 16] biosensors,[17, 18] drug delivery,[19, 20] micro devices, and electronics,[21] there are still technological challenges to control precisely over their microstructure, i.e., size, shape, surface morphology, and composition. The main goal of this research is to develop an innovative method that can address these challenges such as control of microstructure.

In various industrial fields, researchers would like OMS spheres to have a high selectivity with a high yield in catalysis, a relatively narrow size distribution in adsorption and separation, and highly monodisperse spheres in membranes. Controlling microstructure of the OMS particles, i.e., particle size, shape, surface morphology, and composition, are receiving great interest due to their ability to strongly influence the efficiency of the material, as well as offer access to a variety of material properties. There have been the enormous efforts over the past decade in optimizing different routes for the control over their microstructure. To date, there are mainly two methods for the synthesis of OMS: 1) "hydrothermal synthesis"[22] and 2) "nonaqueous synthesis with EISA".[23, 24] The hydrothermal synthesis allow for a chance to make uniform OMS spheres. However, we still face technological challenges such as a diversity of material choices and control of surface multi-functionality.[25] Nonaqueous synthesis with EISA has become more powerful in overcoming the limitations of the previous synthesis method. Specifically, there is no limitation as to the types of surfactants that can be used in this method; as a result, the size of nanopores inside OMS spheres can be controlled

through this method. However, nonaqueous synthesis with EISA still has technological difficulties in making OMS spheres with narrow size distribution and multi-functionality.

There is significant interest in making particles in microfluidics due to its ability to control size, shape, internal structures, and multi-functionalities by generating droplets of precursor solution and rapidly converting the droplets into particles with various sizes and shapes.[26-37] Although the generation of monodisperse multi-functional polymer particles using microfluidic devices has attracted a great deal of research interest throughout the last decade, the synthesis of inorganic mesoporous materials has yet to be demonstrated. Inorganic mesoporous silicates synthesized by the EISA process are typically conducted in nonaqueous solvents (normally ethanol, THF, and acetonitrile). However, if the nonaqueous solvent is used in the microfluidic devices, it is difficult to generate droplets of nonaqueous solvent due to the interaction between solvent and microfluidic devices.

Additionally, a new method suggests for the synthesis of mesoporous silica microspheres with controllable microstructures such as size, shape, surface morphology, and composition by combining microfluidic emulsification and a rapid solvent diffusion induced self-assembly (DISA) in the microfluidic channels. This new method is referred to as microfluidic DISA, which can make it possible to control the particle sizes and manipulate the surface morphologies. The microfluidic DISA generates opportunities to create innovative nanoporous materials that can be applied to industrial areas such as energy, automobile, health and medicine, and sensor technology.

The overarching theme of this dissertation is to develop novel synthesis methods to address current challenges such as the control of material microstructure. Focus is placed on two new synthesis methods: 1) a simple technique for the fabrication of thin oriented MFI zeolite membranes with controlled thickness, orientation, and grain boundaries. 2) microfluidic synthesis for monodisperse OMS particles with controllable size, shape, surface morphology, and composition. If successful, the proposed methods could have significantly positive effects on nanoporous materials research, the energy industry, the environment, and society.

1.2 Proposal

1.2.1 A simple preparation of *b*-oriented MFI zeolite membranes with controlled microstructure

A simple and commercially viable method-termed the micro-tiles-and-mortar method- is demonstrated to make continuous *b*-oriented MFI membranes with controlled membrane microstructure. The essence of this method is preserved the orientation of the *b*-oriented seed crystals by passivation of the flat crystal faces with a thin layer of a sputtered mixture of gold and palladium. This thin metal layer suppresses the nucleation and growth of crystals in the out-of-plane direction while allowing the growth of crystals along the in-plane direction. This simple method enables control of the membrane thickness by using plate-like seed crystals with different thicknesses along the *b*-axis (0.5 μm to 2.0 μm), as well as to manipulate grain boundaries by selectively eliminating

the tetrapropylammonium hydroxide (TPA) present in them. Here, we try to answer the questions in order to demonstrate our commercially viable method.

1.2.1.1 How is the microstructure of zeolite MFI membranes controlled?

Membrane microstructure such as thickness, preferred orientation, and grain boundary affect the performance of the membranes. To get high quality of membranes, it is important to control the microstructure. Our method can prevent the nucleation and growth of seed crystals in the out-of-plane direction by passivating the surface of seed crystals. The thickness of the zeolite membranes determines simply by the thickness of seed crystals. We control the thickness of the membranes by simply controlling the thickness of seed crystals. Oriented MFI zeolite membranes with various thicknesses are fabricated. We control the density of grain boundary by varying the size of the seed crystals. Bigger crystals result in bigger single crystal domain, i.e., lower density of grain boundary.

1.2.1.2 What does the microstructure affect on membrane performance?

It has been reported that thin *b*-oriented silicalite-1 membranes showed high permeability and selectivity for xylene isomers. It was also shown that the performance of silicalite-1 membranes on gas separation were not consistent due to their different microstructure. The effect of microstructure of zeolite membranes on gas separation performance is investigated by measuring permeability and selectivity for single or binary gases using custom-build permeation measurement system. The effects of the

grain boundaries on membrane performance are studied intensively. Especially, the density of grain boundaries and the structure of grain boundaries are controlled by our method and are measured experimentally their effects on the performance of separation.

1.2.2 A new method for the synthesis of the OMS particles with controllable microstructure

In addition, a new mesoporous silica particle synthesis method for the control of the microstructure is discussed, which combines a microfluidic emulsification technique and nonaqueous synthesis with a diffusion-induced self-assembly (DISA) technique. In this method, uniform droplets from an inorganic precursor solution are first generated in a soft microfluidic device and are subsequently changed into ordered mesoporous silica (OMS) spheres by solvent diffusion-induced self-assembly in the microfluidic channels. Here are the questions that are tried to answer in order to demonstrate our new method.

1.2.2.1 What are the critical parameters in the microfluidics to control microstructure of OMS particles?

This proposed method allows for the systematic control of the particle microstructure such as size, shape, and surface morphology by adjusting the fluid conditions. Monodisperse precursor droplets are generated in a T-shape hydrodynamic-flow-focusing geometry[38] by introducing two perpendicular intersecting flows: one continuous oil phase and the other as an ethanol-rich precursor phase through microchannels. The flow-focusing geometry enables continuous breakage of the

precursor flow into droplets by controlling relative flow rate of the two fluids. The optimized flow rates are investigated of the two immiscible solutions to have uniform precursor droplets. In order to stabilize the droplets of the precursor solution in oil phase, oil-soluble emulsifying reagents are required. While most emulsion technology studies have been done on either water-in-oil or oil-in-water droplets, relatively few studies have been carried out on ethanol-in-oil emulsion due to the amphiphilic nature of ethanol, which poses a challenge. Various emulsifiers are investigated, which can make stable ethanol-rich precursor droplets in oil according to hydrophilic/lipophilic balance (HLB). Liquid droplets are changed into solid OMS microparticles inside or outside microfluidic channel by heat treatment under vacuum condition. The optimized solidification conditions of OMS droplets will be determined without destroying surfactant/silicate hybrid mesostructure during the EISA process.

1.3 Outline

Critical background about the subjects dealt in this dissertation is provided in Chapter I. The main purpose of the research is also discussed in the first chapter.

Chapter II provides the overview of state-of-the art zeolite membranes in separation. Current synthesis methods and the importance of microstructure of zeolite membranes are reviewed and transport mechanisms of gas molecules in the zeolite membranes are also discussed. The overview of OMS particles is reviewed briefly in the introduction of Chapter VII. In Chapter III, experiment procedures for the preparation of zeolite membranes and for the OMS microspheres are provided.

The research results are presented and discussed in following chapters. The results are composed of two main sections and each section explores the synthesis of a different nanoporous material: 1) Chapters IV, V and VI deal with oriented MFI zeolite membranes with controlled thickness, orientation and grain boundary. Chapter IV focuses on the synthesis method for the preparation of continuous MFI zeolite films on the planar substrates. The optimization for the synthesis of MFI zeolite membranes on the porous supports is discussed in Chapter V. Chapter VI discusses the membrane performance and the effect of microstructure of zeolite membranes on gas separation by measuring permeation of xylene isomers; 2) Chapter VII shows microfluidic synthesis of OMS particles with controllable size, shape, and surface morphology.

Finally, Chapter VIII summarizes the results obtained in this dissertation, and suggestions are given for the future work.

CHAPTER II

RESEARCH REVIEW: STATE OF THE ART ZEOLITE MEMBRANES

2.1 Introduction

Zeolites are amino silicate crystalline materials with a very regular pore size and structure. Since zeolites have been produced in large volumes in a powder form, thin films of zeolites have attracted a great deal of research and particular commercial interest such as separation membranes,[3, 6, 39, 40] corrosive-protective coatings,[41] sensors,[42] and low dielectric constant films.[43] Due to their high selectivity, high thermal and chemical stability at high temperatures, zeolite membranes are of particular industrial interest as energy-efficient alternatives to the current processes of distillation, crystallization, and others.

The pore size of zeolite channels is determined by the number of oxygen atoms which form the pore aperture.[44] By changing the number of oxygen in the zeolite framework, the pore size and shape can be controlled. The range of pore size in zeolite is normally 0.3 ~ 1.0 nm which can discriminate gas molecules with a resolution of 1~2 Å. Figure 2.1 shows the framework projection and pore size according to the number of oxygen atoms.

Zeolite membranes have many advantages, as listed in Table 2.1, when compared to polymeric or organic membranes in separation applications.[45] Figure 2.2 summarizes the characteristics of several zeolite structures that have been applied in zeolite membranes in terms of pore diameter together with the kinetic diameter of some molecules.[40]

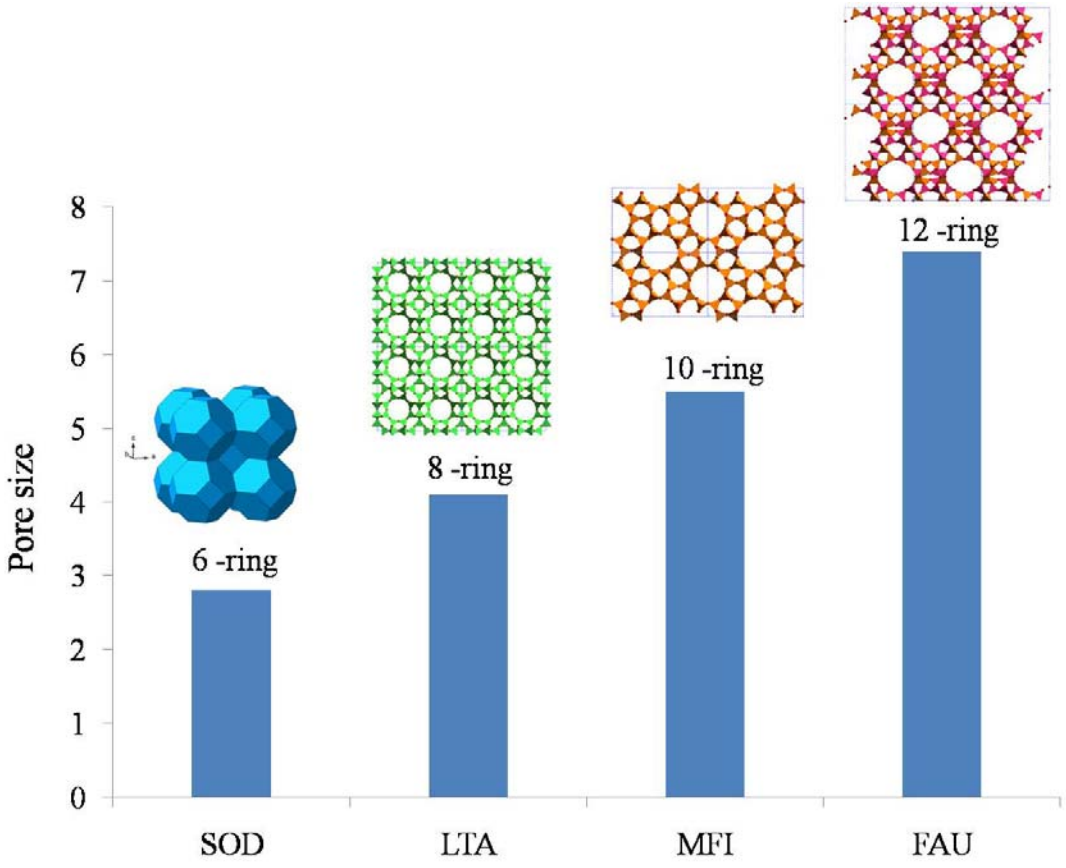

Figure 2.1 Comparison of pore size of different framework

Table 2.1 Advantages and disadvantages of zeolite membranes[45]

Advantages	Disadvantages
Stability of high temperatures	High cost
Resistance to harsh environment	Brittleness
Resistance to high-pressure drops	Poor intensification
Inertness to microbiological degradation	Difficulty in industrial scale-up
Easy cleaning after foiling	Sealing problems

Small pore zeolites such as LTA (Linde Type A) and Chabazite have about 4Å pores, which are relevant to small gas molecules. Medium pore zeolites such as MFI (Mobile Five) and FER (Ferrierite) have pores about 0.58 Å, which are in the similar scales of hydrocarbons and large pore zeolites such as MOR (Mordenite), FAU (Faujasite), and BEA (beta) have pores of about 0.7Å which are for larger hydrocarbons. However, among many zeolites, only a few zeolites have been reported as separation membranes such as silicalite, zeolite A, zeolite Y, ZSM-5, faujasite, mordenite, ETS-10, and SAPO-34.[3, 40, 46-48]. In particular, hydrophilic Na-A zeolite membranes have been commercialized in a large-scale pervaporation plant for alcohol dehydration.[49] In order to commercialize zeolite membranes, there are still a number of challenges that need to be addressed: 1) quality of membranes with high permeability and selectivity; 2) availability with large areas; 3) reproducibility of membrane performance; 4) module reliability under extreme temperature cycling; 5) long-term stability; and 6) cost.

In spite of a relatively short history, a number of publications about zeolite membranes increased by more than 200 in 2004.[40] Most publications focused on solving the current challenges resulting in many progresses to show the possibility for commercialization. The objective of this chapter is to provide a short overview of the current state of the art in zeolite membranes. It deals with zeolite membrane preparation and the importance of microstructure of zeolite membranes, characterization, and applications.

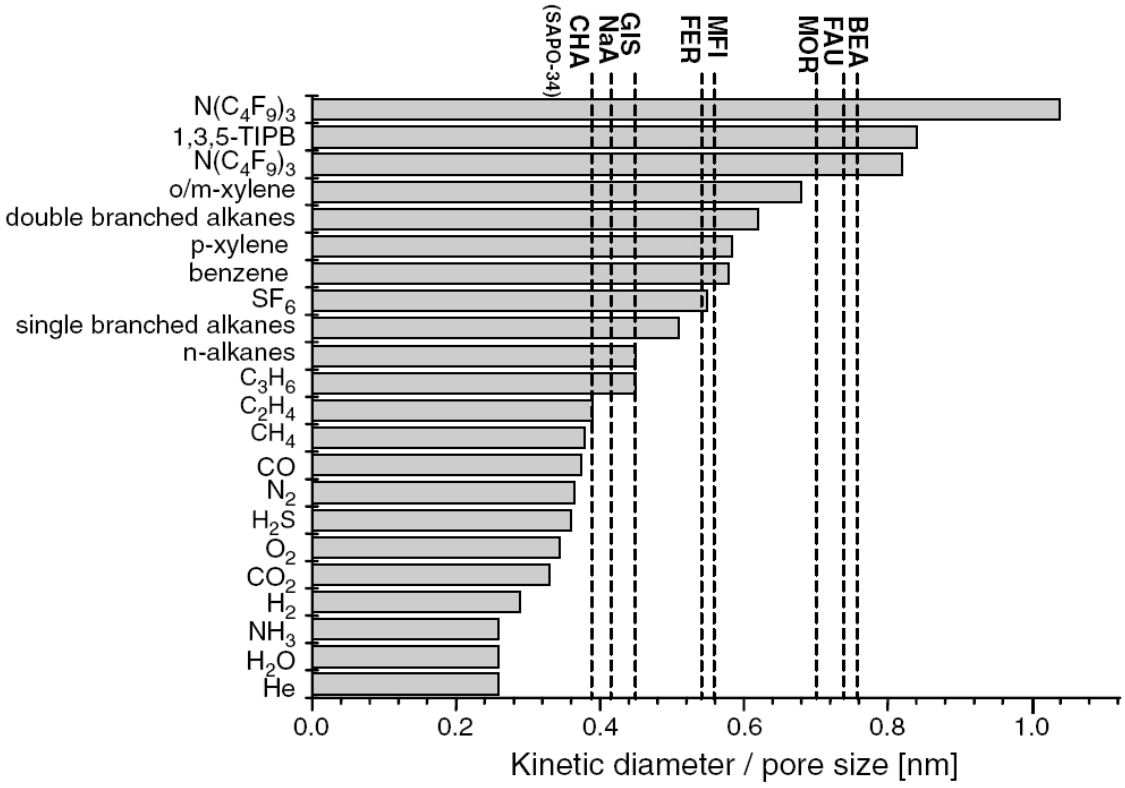

Figure 2.2 Comparison between the effective pore sizes of different zeolites and the kinetic diameters of gas molecules featured in reports on zeolite membranes. Adapted from McLeary et al.[40]

2.2 Preparation of zeolite membranes

For the purpose of gas separation, zeolite membranes require the development of continuous and defect-free layers of zeolites on the porous supports. Many researchers have demonstrated continuous zeolite membranes on the porous supports by liquid phase hydrothermal synthesis. To date, there are mainly two methods of liquid phase hydrothermal synthesis to prepare zeolite membranes; one is direct in situ hydrothermal synthesis, the other is secondary seeded hydrothermal synthesis. The principle, advantages, and challenges of these two methods are discussed here.

2.2.1 Direct in situ hydrothermal synthesis

Zeolite membranes are commonly synthesized by the in situ hydrothermal method. The key feature of this approach is to nucleate and grow a thin and continuous zeolite membrane on the porous support. In this method, the porous support is immersed into the zeolite precursor solution, which generally contains water, silicon or alumina source, and an organic structure-directing agent. The continuous zeolite membrane is grown under autogenous pressure controlled in an autoclave. The autoclave is heated in the oven for a predetermined time resulting in preferential growth of zeolite on the surface of the porous support.

Since the Suzuki patent reported the first zeolite membranes by the in situ method [50], the various types of zeolites such as MFI (silicalite-1, ZSM-5)[51-55], zeolite A[56, 57], zeolite Y[58], mordenite[59], zeolite P[60], and SAPO-34[61] have been synthesized as continuous membranes using the in situ method. The advantage of this method is to simplify the

procedure of a zeolite membrane. Although the synthesis procedure seems to be very simple, the mechanism for the formation of a zeolite membrane is not fully understood. There are two models that explain how zeolite crystals grow to continuous membranes by the in situ method. First, Wang and Yan have studied a film formation model of MFI zeolite layers on stainless steel disks as shown in Figure 2.3.[9]

The model consists of four stages: (1) nucleation and crystallization of colloidal sub-micron crystals, (2) deposition of colloidal sub-micron crystals by favorable interaction, (3) crystal growth in solution and within film, and (4) second-layer formation by settling of fully grown crystals (>1μm) from bulk.[9] The essence of this model is to form a very thin gel layer on the alumina support in the first stage, and then crystals are growing to continuous films.

Vilaseca et al. have proposed the mechanism for the synthesis of zeolite membranes on the alumina porous support by using AFM and SEM analysis.[62] They measured the change of nuclei size and crystal size as a function of synthesis time. In a short time, small size of nuclei is generated both in the solution and on the alumina support. After the concentration of reactants in the solution drops below a certain level, nucleation stops and only zeolite crystals can grow on the support. The key feature of this model is that the nucleation process took place not only in the solution, but also on the support and crystal surfaces as shown in Figure 2.4.

The direct in situ hydrothermal synthesis still has a few limitations for the use of membranes for gas separation: 1) Formation of defects; 2) Difficulty in controlling microstructure such as thickness, orientation, and grain boundary; and 3) reproducibility.

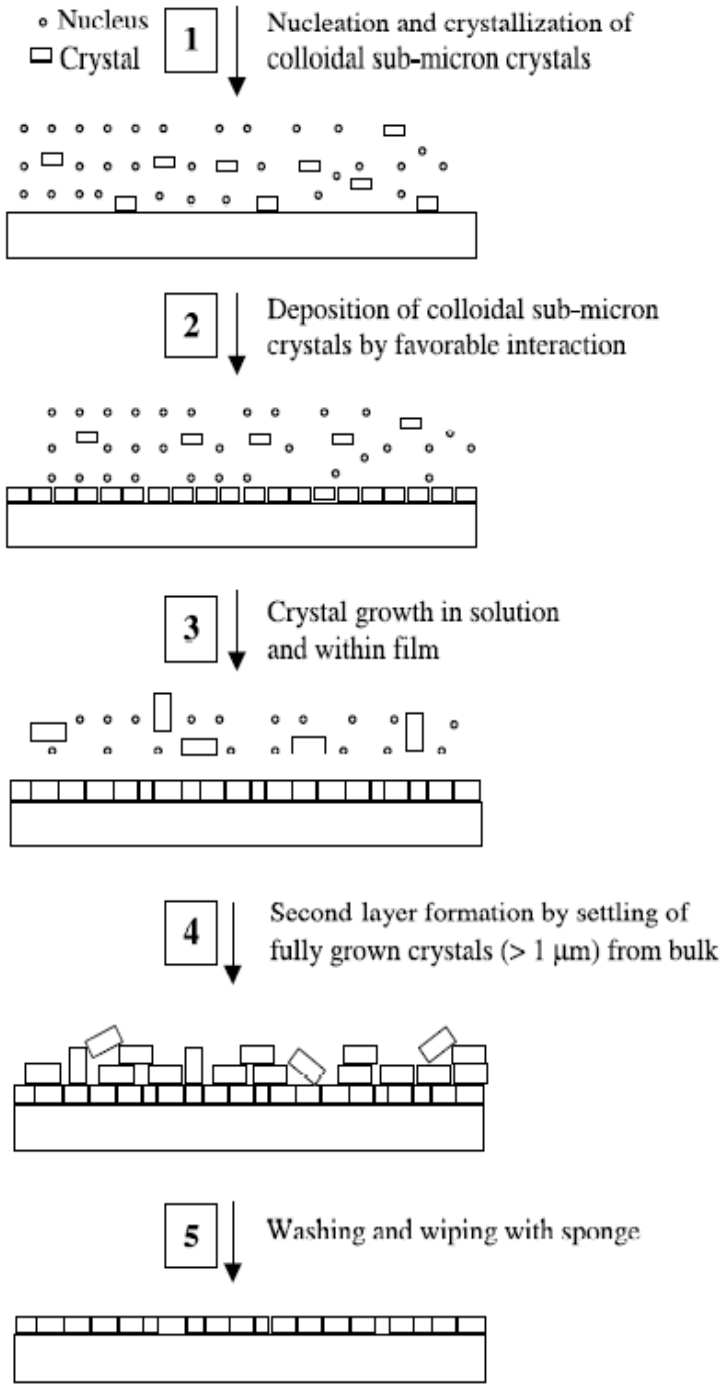

Figure 2.3 A formation model for MFI zeolite films proposed by Wang and Lin[9]

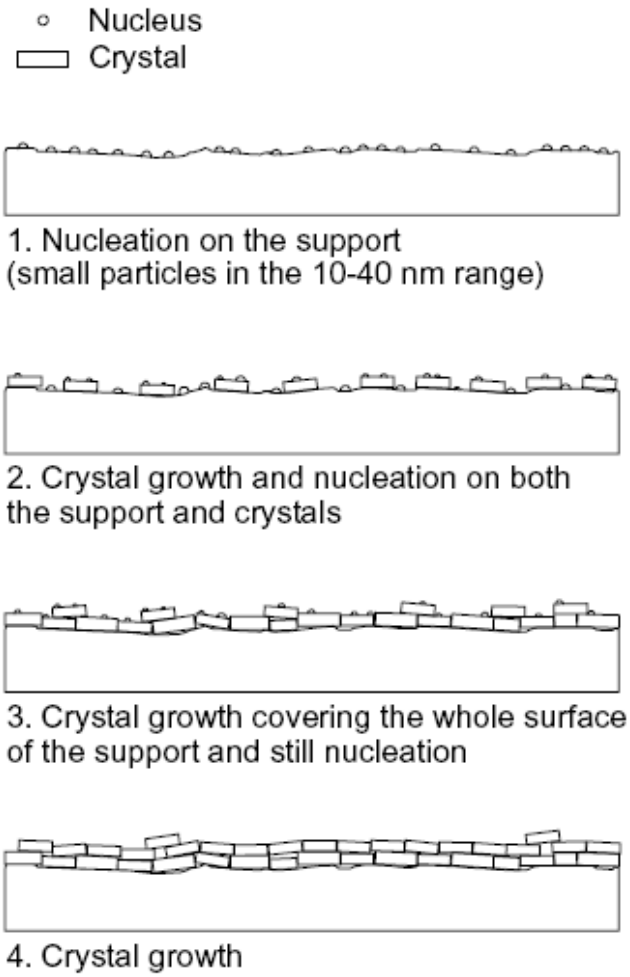

Figure 2.4 A formation model for MFI zeolite films proposed by Vilaseca et al.[62]

There are many attempts to improve these limitations by many researchers. For example, in order to prepare defect-free zeolite membranes, Miachon et al. tried to form zeolite layers within the pores of the support, rather than on top of the support.[63, 64] According to their finding, nucleation and growth of zeolite within the pores of the support highly depended on reaction conditions such as temperature and time. If the reaction occurred at relatively low temperatures (~130^{o}C) over a long time (~ 6 days), the growth of zeolite is likely within the pores of the support. However, at high temperatures (~190^{o}C), zeolite layers can form on top of the porous support.

Apart from the formation of defects in zeolite membranes, the distribution of zeolite on the porous support may cause lack of reproducibility for gas separation. The distribution of zeolite membranes has been reduced by simply repeating the experimental number of synthesis cycles. Vroon et al. prepared MFI zeolite membranes by two hydrothermal reactions with two different synthesis temperatures.[65] They claimed that lack of connectivity between the individual zeolite crystals may affect the performance of zeolite membranes. By repeating hydrothermal reactions, improvement of inter-connectivity of the crystalline zeolite layers has been achieved.

Recently, the development of removing defects after synthesis has been reported. These include coking treatments,[66] chemical vapor deposition,[67] and chemical liquid deposition.[68] Those techniques improved selectivity of hydrocarbon separation by effectively blocking defects. However, the flux of gas molecules was decreased.

2.2.2 Secondary (seeded) growth method

Zeolite membranes prepared by the in situ method have shown promising performance in gas separation applications since they have developed in the early 1990s. However, they have limitations to control microstructure of zeolite membranes, which can affect their separation performance. Microstructure of zeolite membranes refers to thickness, orientation, and grain boundary, which will be discussed in detail in the next section. The most successful approach to control microstructure of zeolite is to decouple the nucleation step from the crystal growth, and we call this the secondary seeded growth model.

Unlike the in situ synthesis method, the secondary growth method consists of two steps as illustrated in Figure 2.5. The first step of this method is to prepare seed crystals by conventional hydrothermal synthesis resulting in either colloidal crystals or the powder form of zeolite crystals. The size of seed crystals could be hundreds of nanometers. Seed crystals are then depositing on the porous support, which could be preferentially oriented layer along the out of the plane direction (i.e. along the *b*-axis) or randomly ordered layer. Finally the seed layers are subjected to hydrothermal growth to make continuous defect-free membranes. There are several advantages over the in situ method: 1) easy to control microstructure, 2) less dependent on the substrate types by decoupling nucleation and growth as listed in Table 2.2. Tsapatsis and co-workers first reported MFI membranes by the secondary growth method.[69] The secondary growth method improved control of microstructure, flexibility for crystal growth, and reproducibility.

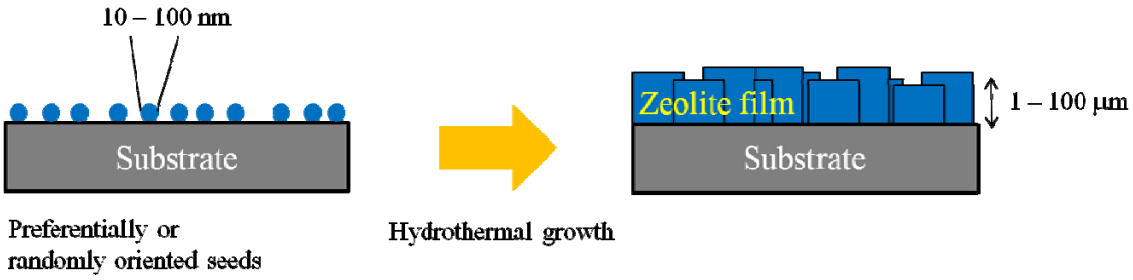

Figure 2.5 Schematic illustration of the procedure of secondary (seeded) growth

Table 2.2 Comparison of two synthesis methods for zeolite membranes

	In situ method	Secondary (seeded) growth
Advantages	▪ Simple process	▪ Easy to control microstructure ▪ Less sensitive to procedures and conditions
Disadvantages	▪ Sensitive to procedures and conditions ▪ Long process time	▪ Complexity of the process

2.2.2.1 Methods for deposition of zeolite seed layers

To make continuous zeolite membranes by secondary growth, it is essential to form defect-free and close-packed seed layers on the porous support. The various seeding methods such as dip coating,[69-72] slip casting,[73] vacuum seeding,[74] self-assembly by attraction interaction,[75-77] ultrasound assisted seeding,[78] and manual assembly by rubbing[79] have been reported. In this section, we discuss the methods used for depositing seed layers of zeolite crystals on the porous supports.

2.2.2.1.1 Dip coating

Zeolite seeds are deposited on the porous support by simple contact with a colloidal suspension of the zeolite crystals as shown in Figure 2.6. The colloidal suspension of zeolite crystals are stabilized by adjusting the pH after the synthesis of small zeolite crystals (< 100 nm). The porous supports are brought to the surface of colloidal suspension. The horizontal surface of the polished support is in contact with the colloidal suspension, which can adhere to the porous support due to surface tension and capillary force. During the drying process, solvents are evaporated and zeolite seed crystals can attach to form seed layers on the porous supports.

Figure 2.7 shows the MFI silicalite-1 seed layers formed by the dip coating method.[70] A stable suspension of silicalite-1 seed crystals with a particle size of around 100 nm were used as a seed layer prior to doing secondary growth. This dip coating method is quite simple to prepare seed layers. However, defects such as pin-holes or low density of packing can be found on the surface.

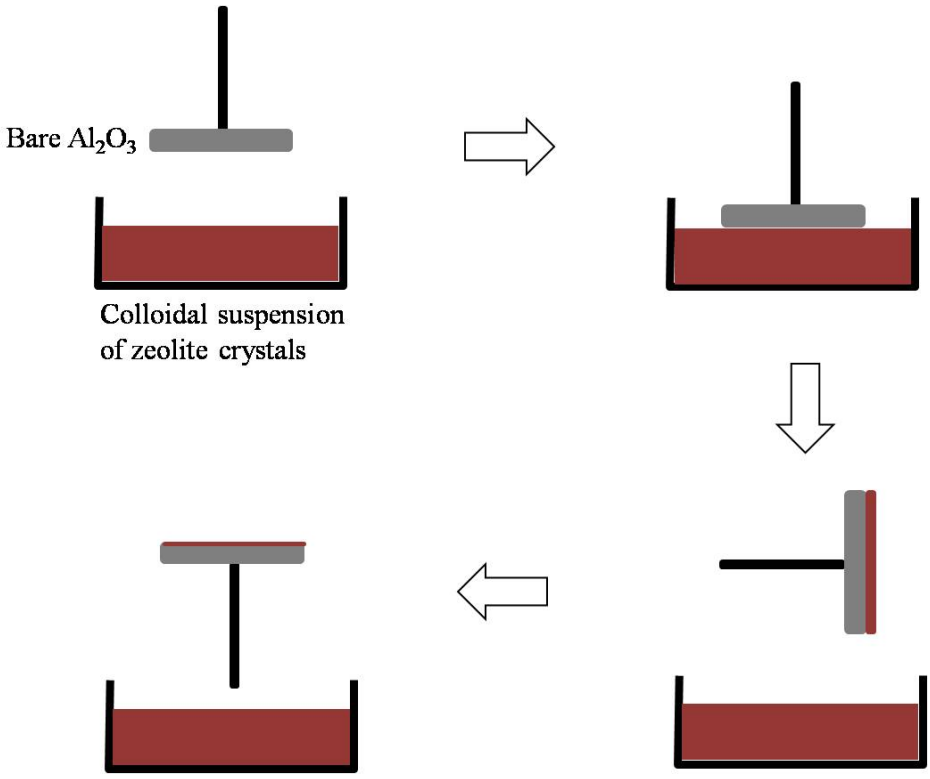

Figure 2.6 Schematic illustration of dip coating for the formation of zeolite seed layers on the porous support

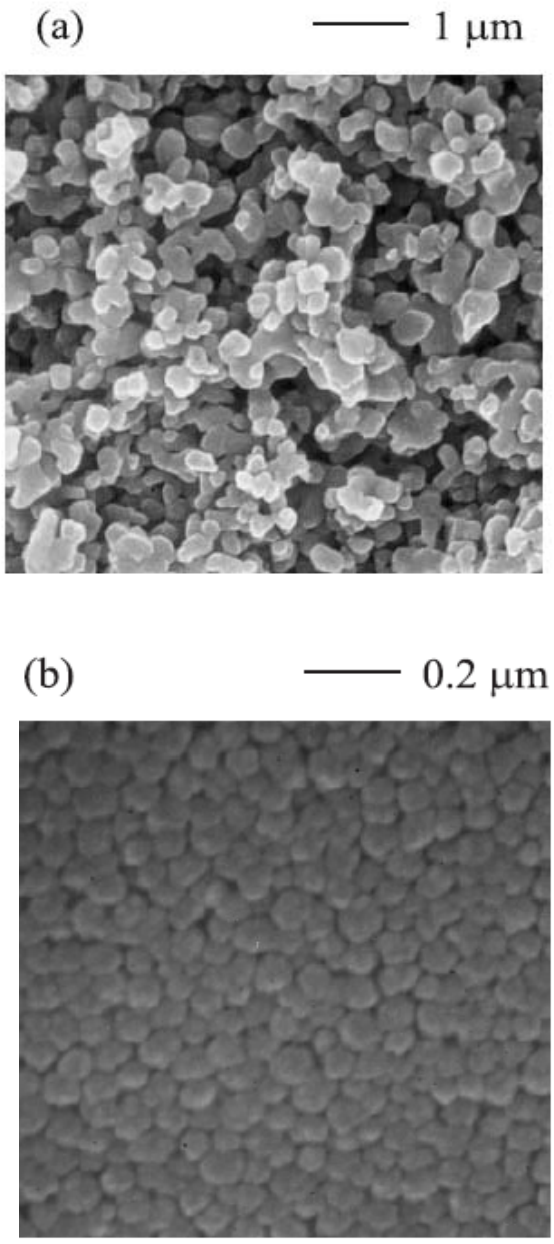

Figure 2.7 Scanning electron micrographs of (a) surface of Al_2O_3; and (b) silicalite-1 seed layer. Adapted from Xomeritakis et al.[70]

In the dip coating process, the main driving force to attach the seeds on the porous support is the capillary force. Once water is filled on the support pores, capillary forces acting on seed crystals guided onto the surface of the support disappear and seed crystals in the suspension are stopped to move to the support. If seed layers are formed by just one time dip coating, chances are likely to have the seed layers with defects. In order to obtain the high density and coverage of zeolite seed layers, it is necessary to repeat the drying and dip coating, which took a long time to coat.

2.2.2.1.2 Vacuum seeding

To overcome drawbacks of the dip coating method, Huang et al. reported the vacuum seeding method.[74] Figure 2.8 shows the apparatus for coating zeolite A seeds by the vacuum method. In the vacuum seeding method, the driving force of seeding is the capillary force, as well as vacuum force. The water being penetrated into the support pores by capillary force keeps filling into the pores by vacuum force. The zeolite seeds in the suspension solution are transported to the porous support continuously.

2.2.2.1.3 Self assembly by attractive interactions

There are a couple of methods to form seed layers by creating attractive interactions between seed crystals and supports such as an electrostatic, van der Waals, or covalent bonding. In order to make defect-free and closed pack seed layers, it is more desirable to deposit seed crystals using self assembly by attractive interaction.

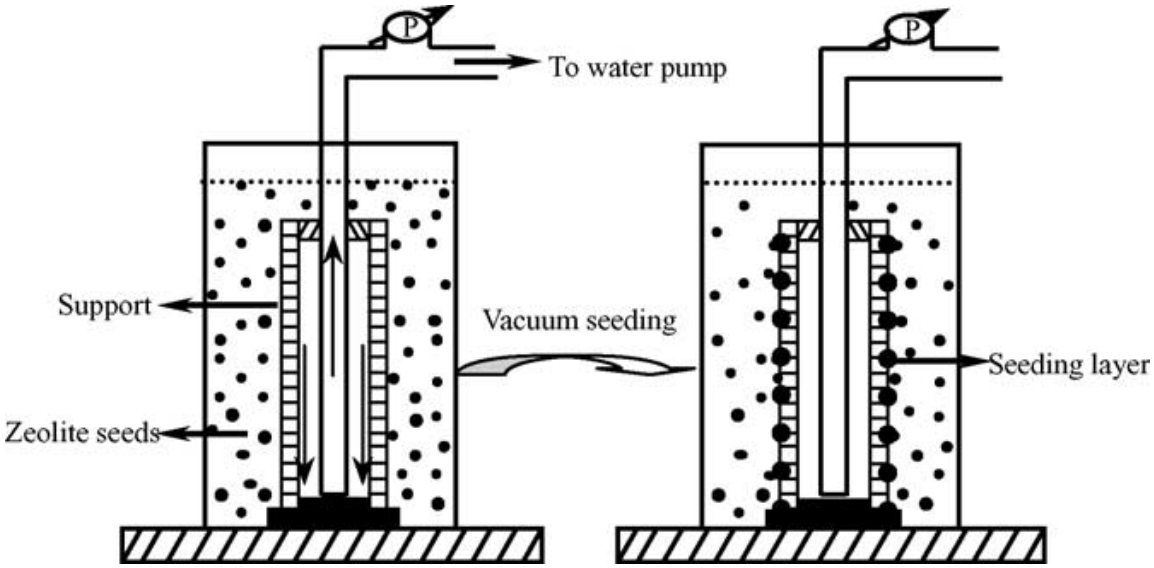

Figure 2.8 Apparatus for coating A-type zeolite seeds by the vacuum seeding method. Adapted from Huang et al.[74]

Among the attractive interactions between seed crystals and supports, electrostatic interaction is achieved by the change of surface charge of zeolite seed crystals and/or supports. Boudreau et al. deposited zeolite A seed crystals onto the glass or silicon wafer using electrostatic interaction.[80] A suspension of zeolite A seed crystals was prepared and determined its isoelectric point (pH 5) by the measurement of ζ potential as a function of pH. The surface of zeolite A seed crystals was changed by reacting with 3-aminopropyl trimethoxy silane (APTMS), which contains an amino group. The amino group has a pK_a of 10.7. At the neutral pH 7, the amino group is protonated to be positive charge NH_3^+ so that the zeolite A seed crystals modified by APTMS have positive charge in the neutral solution. Deposition of zeolite A seed crystals with a positive charge were carried out on the glass substrate with normally negatively charged surface by electrostatic interaction between seed crystals and substrates.

Covalent bonding can be used to attach zeolite crystals on the surface of supports. The zeolite and the support are chemically modified with molecules, which can react to form covalent bonding. Kulak et al. reported zeolite monolayer on the glass substrate by covalent bonding.[81] The surface of zeolite was functionalized with 3-aminopropyltriethoxysilane (APTES), and the glass surface was modified with 3-(2,3-epoxypropoxy) Propyltrimethodxysilane as shown in Figure 2.9. Amine groups on the surface of zeolite can bind covalently with epoxide groups on the glass substrate leading to effective assembly between zeolites and glass supports. It was shown that the strength of bonding between zeolite seeds and glass substrates was so strong that 99% of the seed monolayer can survive after sonication for 1h.

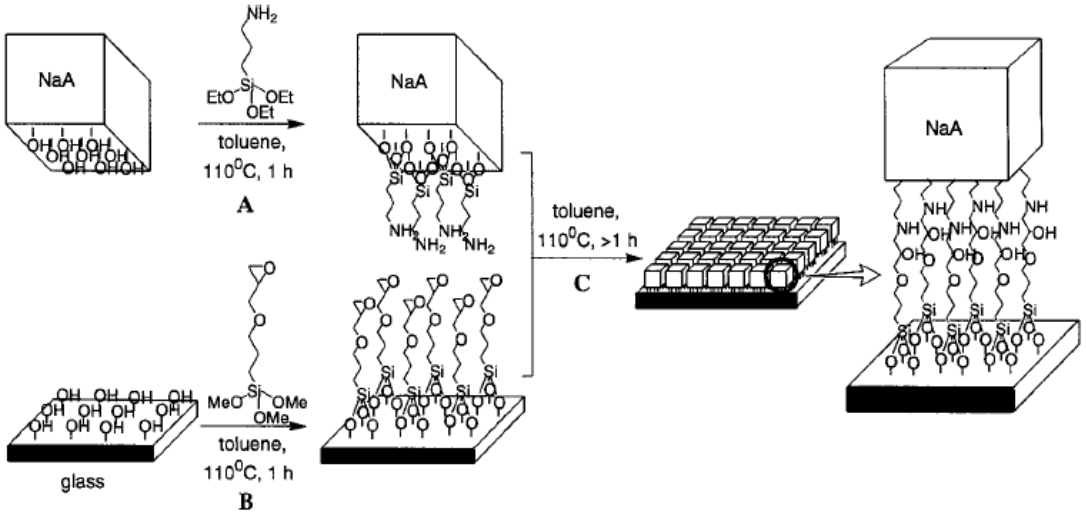

Figure 2.9 Schematic procedures to assemble zeolite A monolayer on a glass substrate by covalent bonding. Adapted from Kulak et al.[81]

However, it is also observed that there are defects such as uncovered areas due to the limited number of amine or epoxy linkages and the roughness of supports. To improve the coverage of zeolite seed layers, polyamine linkers were used to coat on the surface of either zeolites or supports. In this case, polymeric linkers have a lot of amine functional group, which can provide enough number of amine groups to react with epoxy groups, and are flexible on the molecular scale. Kulak et al. also reported zeolite A monolayer with high density of packing using polyamine linkers.[82] In this paper, the use of polyethylenimine linker improved the coverage of zeolite A monolayer. After a detachment test by sonication for 1 hour, 75% of zeolite A monolayer still survived on the glass substrate, which indicated that zeolite A crystals bound covalently to the surface of glass substrate.

2.2.2.1.4 Ultrasound assisted seeding

In the self assembly by attractive interaction, the zeolite monolayer is obtained by the reaction of functional groups on the surface of zeolite crystals and supports. To achieve high coverage of zeolite monolayer, reflux and stirring had been used the way to promote reaction in the self assembly. However, under those conditions, the reaction time was needed at least 24 hours.

Lee et al. reported the ultrasound-assisted seeding method to increase the rate of achieving around 100% coverage of zeolite monolayer.[78] Suspension of zeolite A crystals was prepared in toluene and the surface of glass substrate was modified with 3-chloropropyltrimethoxysilane (CP-TMS).

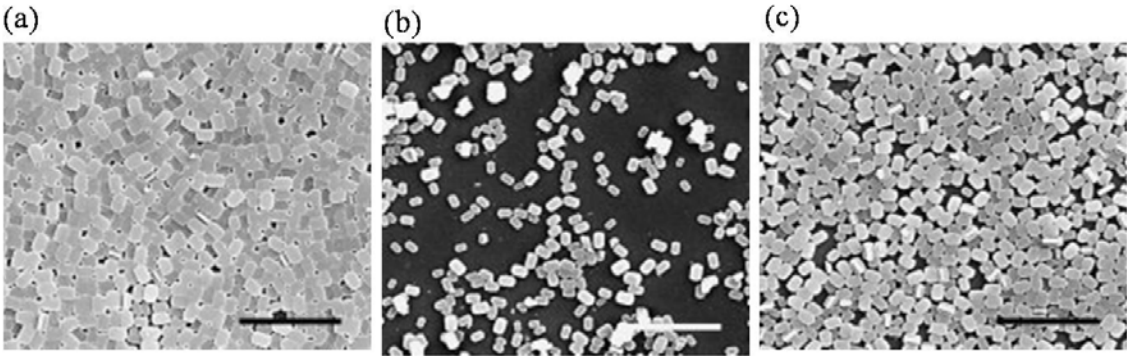

Figure 2.10 SEM images of zeolite A monolayer formed by (a) ultrasound-assisted deposition for 10 min (b) reflux method for 10 min (c) reflux method for 24 h. Adapted from Lee et al. [78]

The glass substrate modified with CP-TMS was inserted between two cover glasses and then was placed in the suspension solution. Sonication started to deposit zeolite A crystals and within 10 min high density of packing of zeolite A monolayer was obtained. In Figure 2.10, SEM images show the zeolite A monolayer formed by ultrasoundaided deposition and reflux method, respectively. Obviously, the ultrasound-aided seeding method increased in the rate of deposition of zeolite A. Within 10 min, highly closed pack zeolite A monolayer was obtained, while it took at least 24 hours by the reflux method.

2.2.2.1.5 Manual assembly by rubbing method

The first commercialized zeolite membranes are Zeolite A membranes synthesized by secondary growth method with seed layer prepared by rubbing method on the tubular porous supports. Self assembly has a size limitation of zeolite crystals for the formation of zeolite monolayer. The upper size limit for self assembly is approximately around 3 μm because larger crystals are very difficult to disperse in the solution. Direct attachment with the hands normally organizes big crystals (> 3 μm) and its lower size limit is around 0.5 μm. In the overlapping range of crystal size from 0.5 μm to 3 μm, direct attachment is desirable to deposit zeolite monolayer in terms of process time, large area deposition, close packing density, and uniform orientation of the crystals. Manual assembly by rubbing is one of the direct attachments. Lee et al. reported silicalite-1 and ETS-10 monolayer by manual assembly on the glass substrates.[79]

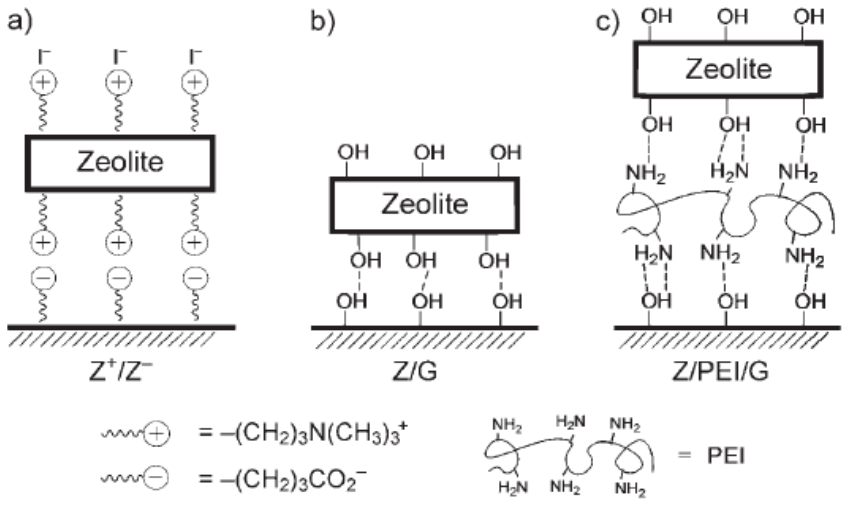

Figure 2.11 Types of bonding effective for the monolayer assembly of zeolite (Z) microcrystals on substrates: a) Ionic bonding between the zeolite-tethered TMP^{+} and glass (G)-tethered Bu^{-} b) hydrogen bonding between the surface hydroxy groups of zeolite and glass; and c) PEI-mediated hydrogen bonding between the surface hydroxy groups of zeolite and glass. Adapted from Lee et al.[79]

In the manual assembly, ionic bonding and hydrogen bonding between zeolite crystals and substrates were most effective for the monolayer assembly of microcrystals among various types of bonding. For the ionic bonding, the surface of zeolite crystals was modified with trimethylpropylammonium groups being positive charge and glass substrate was coated with butyrate groups being negative charge. In the case of hydrogen bonding, polyethyleneimine (PEI) was served as a linker providing hydrogen bonding with hydroxyl groups of the zeolite crystals and glass substrates as shown in Figure 2.11.

2.2.2.2 Secondary growth

2.2.2.2.1 Conventional heating

The growth of zeolite seed layer is done hydrothermally with a dilute synthesis mixture. The porous supports with zeolite seed layer are placed in the Teflon-lined autoclave with filtered synthesis solution and increased temperature to lead crystal intergrowth filling the gap between seed crystals, resulting in continuous membranes. In order to make continuous zeolite membranes; it is necessary to find optimized hydrothermal synthesis such as temperature and time.

2.2.2.2.2 Template-free secondary growth

Template-free secondary growth of zeolite membranes is attractive for not only avoiding calcination that is probably source of defect formation, but also saving the cost of chemicals. The various types of zeolites such as SOD,[83] FAU,[84, 85] and MFI[86-89] has been synthesized membranes by template-free secondary growth. Although thin, well intergrown MFI zeolite membranes were obtained by template-free synthesis, they

showed generally a lower permeance and different selectivity than that of the membranes prepared with a template.

2.2.2.2.3 Microwave-assisted synthesis

Recently, microwave (MW)-assisted syntheses are widely used due to a fast, simple, and energy-efficient method. Advantage of MW-assisted synthesis of zeolite membranes is that one can reduce the synthesis time and cost. Rapid heating rate driven from thermal lag and short induction period in MW-assisted synthesis enable to produce a rapid nucleation and growth as well as fast supersaturation of the reaction mixture.[90]

With closely packed zeolite seed layer, continuous zeolite membranes have been fabricated within a few minutes or hours by MW-assisted secondary growth. In particular, the Na-A,[91] SAPO-5,[92] LTA, ETS-4,[93] and MFI[73, 94-96] zeolite membranes have been prepared by MW-assisted method. Na-A membranes were fabricated within 15 minutes by coupling MW and secondary growth. ETS-4 films were formed within 1 hour, whereas classical synthesis needs 12 ~ 24 hours. MFI membranes also were obtained within 1 hour.

2.3 Microstructure of zeolite membranes

Microstructure of zeolite membranes refers to grain size, shape, thickness, orientation, and grain boundary. Since zeolite membranes are polycrystalline in nature, their microstructure plays important roles in the determining the performance of membranes such as permeance and separation. Controlling the microstructure of zeolite

membranes has a great implication. There have been many reported efforts to control the grain size,[97] orientation,[6, 39, 98] membrane thickness, and structure of grain boundary.[99-101] MFI silicalite-1 zeolite crystals have asymmetric pore structures with straight channels along *b*-axis and sinusoidal channels along *a*-axis. Also, due to the simplicity of the synthesis and its potential in the separation of light hydrocarbons such as butane isomers and xylene isomers, MFI zeolite has attracted a great deal of interest as a model system for the study of the control of membrane microstructure. In this section, the research progress on the control of the microstructure of MFI membranes such as orientation and grain boundary structure are discussed.

2.3.1 Orientation

The asymmetric pore structure of MFI zeolite provides the ways to fabricate zeolite membranes with various pore orientation such as the c-, a-, b-, h0h- and randomly oriented MFI membranes. The schematic illustration in Figure 2.12 shows the processing steps to manipulate and control the orientation of MFI zeolite membranes.

Xomeritakis et al. showed c- and h0h-orientation of MFI silicalite-1 membranes by secondary growth with randomly oriented seed layer in the presence of TPA (Figure 2.12, (a)).[102] Due to the fastest growth rate along the *c*-axis, it is likely to eventually get *c*-oriented MFI membranes. By changing temperature and time of the secondary growth to reduce the rate of crystal growth, h0h-oriented MFI membranes can be obtained. In Figure 2.13, *c*-oriented membranes with 12 ~ 18 μm in thickness were fabricated at

175°C for 24 h and *h0h*-oriented membranes with 2 μm in thickness were synthesized at 90°C for 120 h in the hydrothermal synthesis.

Both experimental data and simulation[103, 104] have suggested that *b*-oriented MFI membranes show superior performance for organic vapor separation by providing the fastest diffusion pathway through the straight channel along the *b*-axis perpendicular to supports. However, it is a challenge to make *b*-oriented MFI membranes by hydrothermal treatment of MFI zeolite seed layer in the presence of TPA because of the emergence of *a*-oriented twins on the seed layer and eventual *c*-oriented membranes. To achieve the synthesis of the *b*-oriented MFI zeolite membranes, Lai et al. reported the optimized secondary growth conditions that control the in-plane and out-of-plane growth rate by selecting appropriate trimer-TPA (Figure 2.12 (b)).[6] A *b*-oriented MFI zeolite seed monolayer was prepared by self assembly on the α-Al_2O_3 supports. The key for successful *b*-oriented MFI membranes was to maintain the orientation of the seed layer during the secondary growth. When using monomer-TPA in zeolite synthesis during the secondary growth with *b*-oriented MFI seed layer, the orientation of MFI membranes is lost because of the slowest growth rate along the *b*-axis. By selecting appropriate trimer-TPA, the growth rate along the b-axis was enhanced enough to maintain the orientation of seed layer during secondary growth, which results in *b*-oriented MFI membranes as shown in Figure 2.14.

By comparing separation performance of MFI zeolite membranes, the preferred orientation of the MFI zeolite membranes remarkably influences the permeation behavior of gas molecules as shown in Figure 2.15.

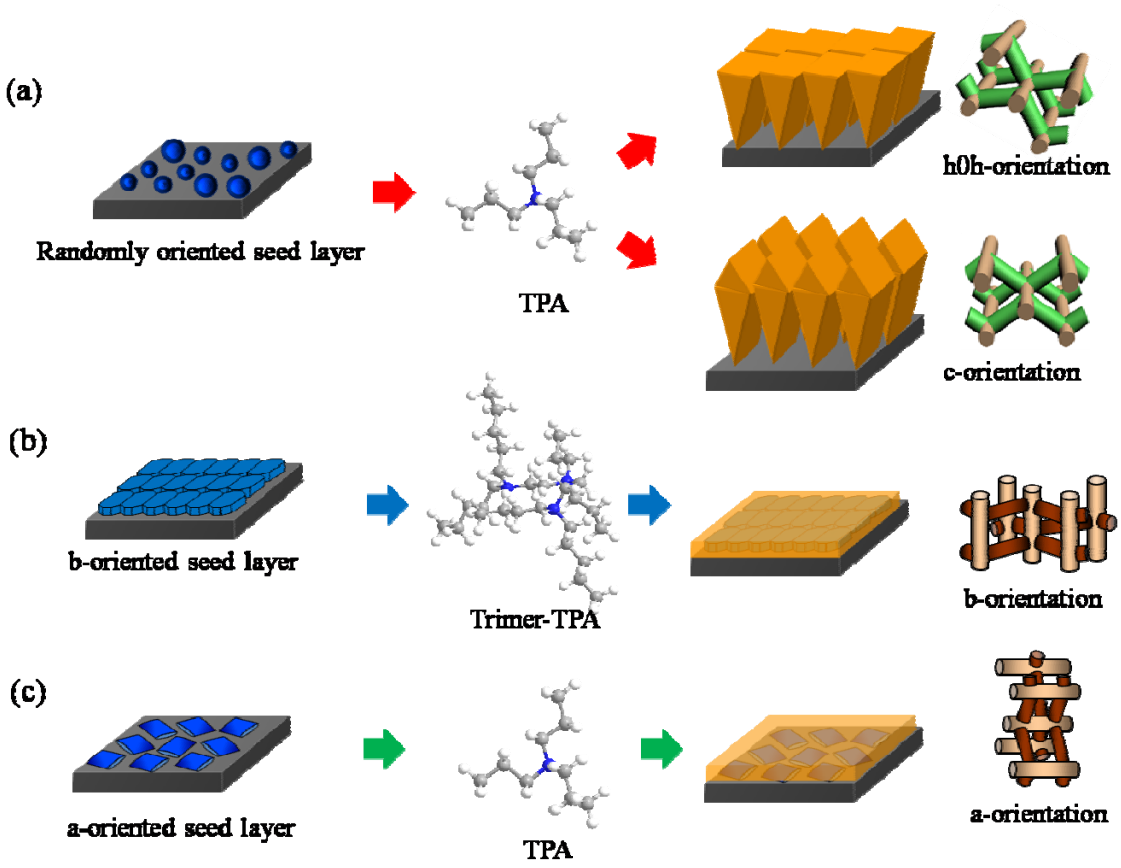

Figure 2.12 Schematic illustration for the control of the pore orientation

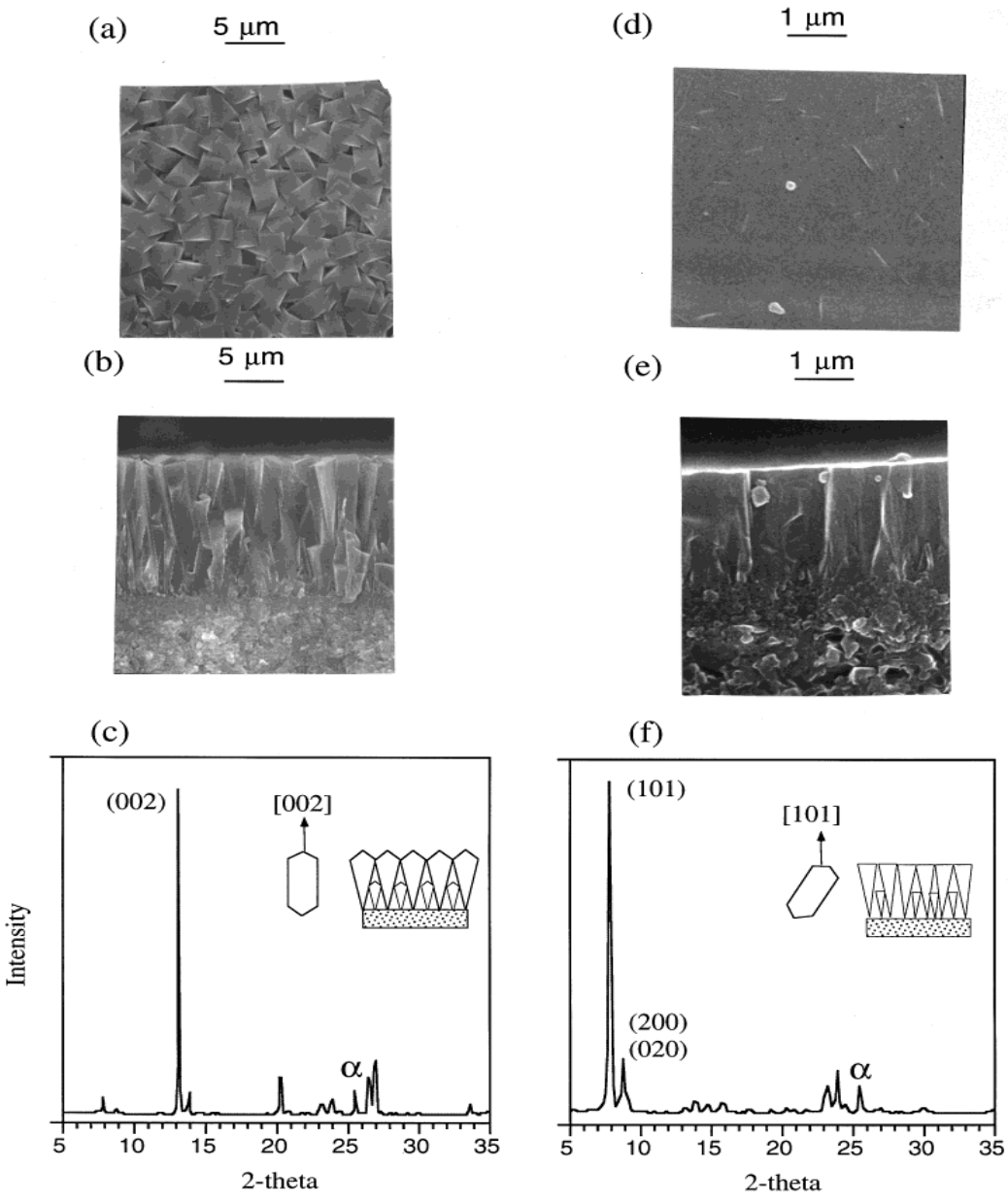

Figure 2.13 SEM top views, cross sections, and XRD patterns of (a,b,c) *c*-oriented MFI membranes and (d,e,f) *h0h*-oriented MFI membranes. Adapted from Xomeritakis et al.[102]

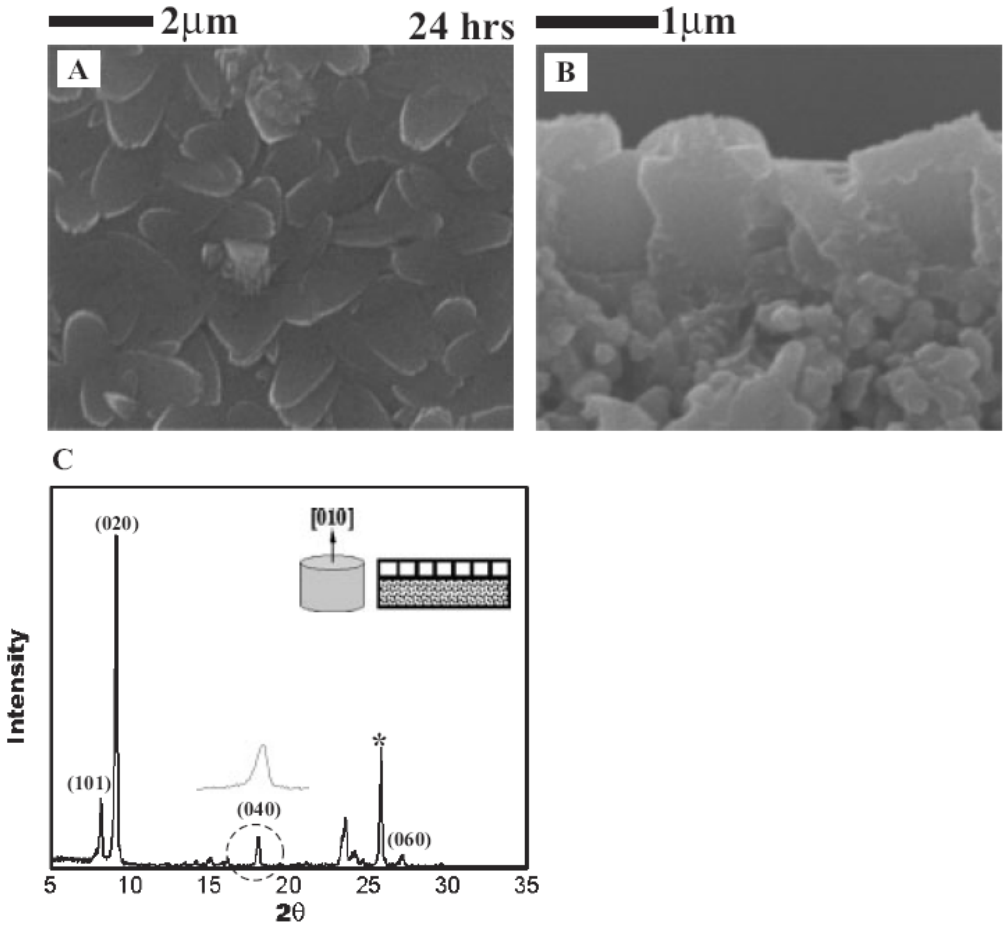

Figure 2.14 Morphology of a *b*-oriented MFI zeolite membrane synthesized at 175°C, 24 h in the presence of trimer-TPA: a) SEM top view; b) SEM cross sectional view; and c) XRD pattern. Adapted from Lai et al.[6]

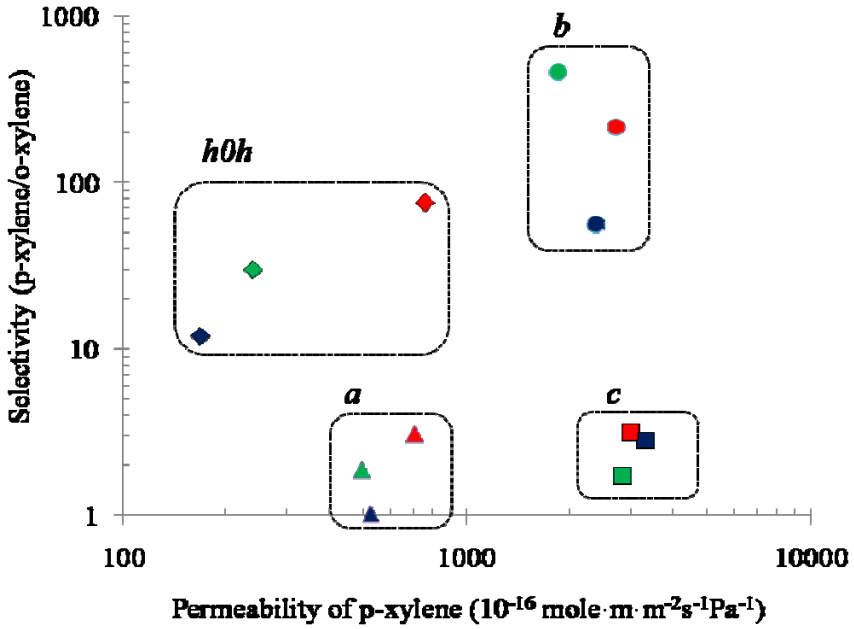

Figure 2.15 Performance of *a*- (▲),[105] *b*- (●),[6] *c*- (■),[102] and *h0h*-oriented (◆)[102] MFI silicalite-1 membranes for the separation of xylene isomers at temperatures ranging from 25°C to 200°C (blue: 25°C ~ 100°C, red: 100°C ~ 150°C, green: 150°C ~200°C)

For the separation of xylene isomers, it was shown that the selectivity of *p*-xylene (kinetic diameter ~ 0.58 nm) over *o*-xylene (kinetic diameter ~ 0.68 nm) in the *b*-oriented MFI membranes were unprecedented.[6, 39] This huge increase of separation performance has been attributed to two main factors.[6] First, channels are straight along the *b*-axis to effectively enhance intracrystalline diffusion of molecules. Second, *b*-oriented membranes make better grain structures compared to those of membranes with other orientation, which can reduce intercrystalline diffusion.

2.3.2 Grain boundary structure

Zeolite membranes are polycrystalline materials that consist of grains and grain boundaries. A challenge to commercialize zeolite membranes is to prevent defects and cracks formed in grain boundaries during calcination. Defects in grain boundaries are formed in response to stresses that are induced by thermal treatment during TPA removal. Non-selective transport pathways through defects in grain boundaries make molecular sieve membranes to lose the separation performance.

There are successful approaches to minimize defects formed in grain boundaries. Control of the microstructure of zeolite membranes plays an important role to obtain good membrane performance. As discussed in the previous section, the membrane orientation makes the structure of grain boundaries different which can affect the formation of defects. Figure 2.16 illustrated a possible scenario to form defects according to the membrane orientations by Lai et al.[6]

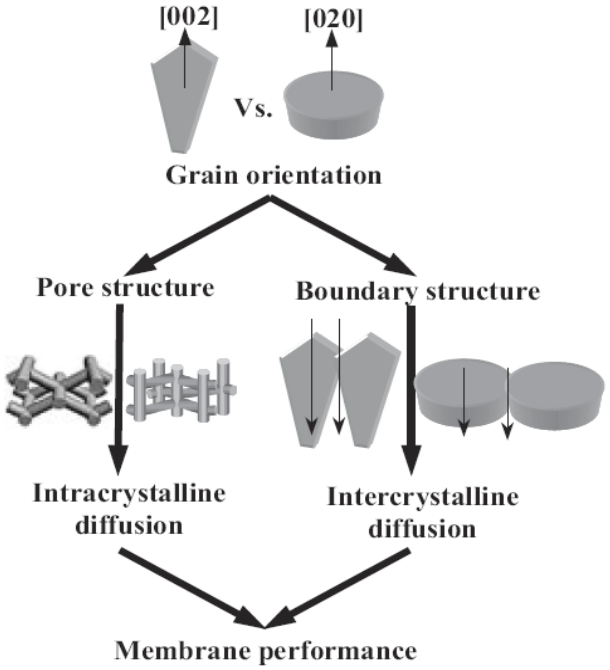

Figure 2.16 Schematic illustration of the potential influence of membrane orientation on performance. Adapted from Lai et al.[6]

The *c*-oriented MFI membranes would have less contact with adjacent seed crystals after secondary growth so that it was likely to generate defects or cracks by thermal stresses during calcinations. However, the *b*-oriented membranes would have a better contact between seed crystals that makes grain boundaries rigid.

Choi et al. recently demonstrated grain boundary defect elimination in a zeolite membrane by rapid thermal processing (RTP).[99] RTP heating up 700^{o}C within a minute was carried to *c*-oriented MFI membranes with a higher density of grain boundaries. RTP treatment led to make condensation of Si-OH groups at the grain boundaries resulting in strong bonding to reduce the opening of the grain boundaries. It was reported that separation factor for xylene isomers increased up to 128 from 4 for conventionally calcined membranes.

2.4 Gas transport and separation by zeolite membranes

Transport and separation of gas molecules through zeolite membranes are based on interfacial processes and intracrystalline diffusion. Barrer described that transport through porous crystal membranes can be carried out by five consecutive steps: 1) Adsorption on the external surface, 2) transport from the external surface into the pores, 3) intracrystalline transport, 4) transport out of the pores to the external surface 5) desorption from the external surface as shown in Figure 2.17.[106]

The five steps are all activation process, which assume that molecules jump between low-energy sites. Step 1, 2, 4 and 5 are referred to as interfacial processes and step 3 as intracrystalline diffusion. The operating conditions (temperature, partial pressure) and

characteristic of membranes and gas molecules (pore diameter, channel shape, molecular weight, and average molecular diameter) determine the rate determining step among five steps.

As discussed in previous section, microstructure of membranes also influences the transport and separation of gas molecules. Many researchers have studied the effect of thickness, orientation, and grain boundary on the permeation of membranes. In this section, the transport mechanisms of gas molecules in zeolite membranes are discussed and experiment results are shown. Also, permeation behaviors of hydrocarbon molecules in zeolite membranes are discussed in terms of the microstructure of membranes.

2.4.1 Transport mechanisms in zeolite membranes

2.4.1.1 Interfacial processes

In Figure 2.17, interfacial processes include step 1, 2, 4, and 5. The first step, adsorption on the external surface is affected by adsorbent-adsorbate interaction and temperature. For weak adsorbent-adsorbate interaction or at high temperature, the first step might be negligible and gas molecules enter directly into the pores. The second step, transport from the external surface into the pores are confronted with high energy barrier for entering inside pores as a result of a higher activation energy for this step. In general, the second and the third steps are rate determining. Adsorption on the external surface is usually less than adsorption inside crystal such that the fourth and fifth steps are not a rate limiting step.

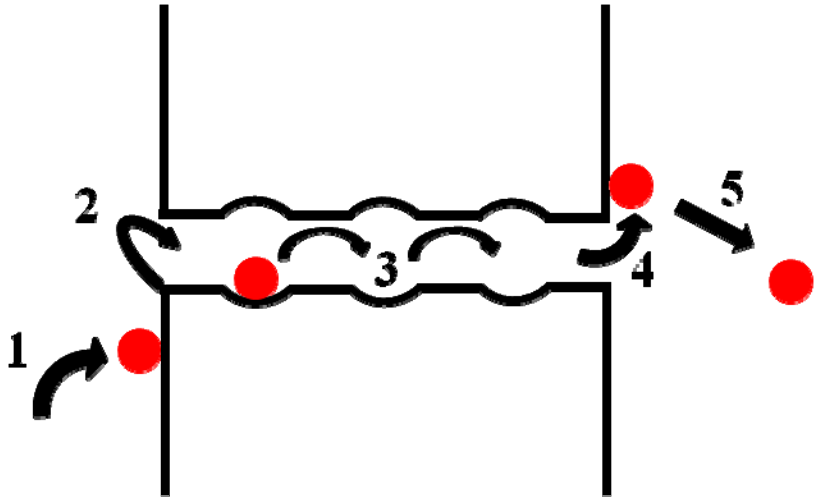

Figure 2.17 Five step model for mass transfer through crystal membranes.[106] Step 1: adsorption from the gas phase on the external surface; step 2: transport from the external surface into the pore; step 3: intracrystalline diffusion; step 4: transport out of the pore to the external surface; step 5: desorption from the external surface into the gas phase

Barrel derived the equation for the importance of interfacial effects.[106]

$$\frac{N_i^{abs}}{N_i^{id}} = \frac{1}{1+\left(\frac{1-K_{P_{i,0}}^{ext}}{1-K_{P_{i,0}}}+\frac{1-K_{P_{i,\delta}}^{ext}}{1-K_{P_{i,\delta}}}\right)\frac{d}{\delta}exp\left\{\frac{\Delta E_a}{RT}\right\}} \quad (1)$$

N_i^{id} is the flux when intracrystalline transport is rate controlling, and N_i^{abs} is the experimentally observed flux. ΔE_a is the activation energy of diffusion. K^{ext}, and K represent the Langmuir parameters for adsorption on the external and internal surface, respectively. Assume that K^{ext}, and K are identical. Then equation (1) simplified to become:

$$\frac{N_i^{abs}}{N_i^{id}} = \frac{1}{1+2\frac{d}{\delta}exp\left\{\frac{\Delta E_a}{RT}\right\}} \quad (2)$$

when N_i^{abs}/N_i^{id} equals to 1, interfacial processes are negligible. According to the equation (2), it is clear that at high temperature interfacial processes become less important for the low activation energy and thick membranes.

2.4.1.2 Intracrystalline diffusion

2.4.1.2.1 Five types of transport mechanisms

There are five types of transport mechanisms in pore diffusion through membranes as described in Table 2.3. Viscous flow is the result of convective flow in the direction of an absolute pressure gradient.[44] This type of diffusion is related to the pore size, normally happen above 20 nm of pore size. The permeance is proportional to pore size and partial pressure, and inversely proportional to temperature.

Table 2.3 Five types of transport mechanisms in pores

Name	Pore diameter	Permeance (Π_i)	Diffusivity (D)	Temperature dependence
Viscous flow	> 20 nm	$\Pi_i = \frac{1}{RT}\cdot\frac{g}{\delta}\cdot\frac{r_p^2}{8\eta_t}\cdot\bar{p}_t$		$\eta_i \approx T$ $\Pi_i \approx T^{-2}, p_i$
Molecular diffusion	> 20 nm	$\Pi_i = \frac{1}{RT}\cdot\frac{g}{\delta}\cdot D_{ij}$	$D_{ij} = \frac{0.001858T^{\frac{3}{2}}}{P\sigma_{ij}^2\Omega_D}\left(\frac{1}{M_i}+\frac{1}{M_j}\right)^{1/2}$	$D_{ij} \approx T^{1.75}, p^{-1}$ $\Pi_i \approx T^{-0.75}, p_i^{-1}$
Knudsen diffusion	2 ~ 10 nm	$\Pi_i = \frac{1}{RT}\cdot\frac{g}{\delta}\cdot D_i^{KN}$	$D_i^{Kn} = d\cdot\sqrt{\frac{8RT}{\pi M_i}}$	$D_i^{Kn} \approx T^{0.5}$ $\Pi_i \approx T^{-0.5}$
Surface diffusion	Mesopores	$\Pi_i = \frac{\rho\cdot q_{sat,i}\cdot g\cdot D_i^s\cdot\nabla\ln(1-\theta_i)}{\Delta p_i}$	$D_i^s = D_i^0\exp\left[\frac{-E_a^s}{RT}\right]$	$\theta_i = f(T,p_i)$ $\Pi_i \approx f(T,p_i)$
Configurational diffusion	< 2 nm	$\Pi_i = \frac{1}{RT}\cdot\frac{1}{\delta}\cdot D_i^g$	$D_i^g = g\cdot d\sqrt{\frac{8RT}{\pi M}}\exp\left[\frac{-E_a^g}{RT}\right]$	$\Pi_i \approx f(T)$
		$\Pi_i = \frac{\rho\cdot q_{sat,i}\cdot g\cdot D_i^s\cdot\nabla\ln(1-\theta_i)}{\Delta p_i}$	$D_i^s = D_i^0\exp\left[\frac{-E_a^s}{RT}\right]$	$\theta_i = f(T,p_i)$ $\Pi_i \approx f(T,p_i)$

Π	Permeance
R	Gas constant
T	Temperature
g	Geometrical factor
δ	Membrane thickness
r_p	Pore radius
η	Dynamic viscosity
p	Partial pressure
D	Diffusivity
M	Molecular weigh
θ_i	Occupancy
E_a	Activation energy
q	Adsorbed phase concentration
q_{sat}	Saturation concentration in zeolite

Molecular diffusion is simply called as bulk diffusion that is dominant by molecular-molecular collisions in the gas phase.[44] Like viscous flow, molecular diffusion takes place in large pores of above 20 nm. One thing to note is that diffusion of single component systems does not contribute to transport.

Knudsen diffusion occurs in a long pore with a narrow diameter with a range from 2 nm to 10 nm by molecule-wall collisions. The Knudsen diffusion coefficient is proportional to the pore radius and the mean molecular velocity. In silicalite-1 membranes, intercrystalline diffusion through non-zeolitic pores such as defects or cracks is observed and analyzed by Knudsen diffusion.

Surface diffusion is an activated transport that the molecules adsorb on the pore surface. The permeance from surface diffusion shows a maximum as a function of temperature.

Configurational diffusion occurs in micropores, especially in zeolite. Configuration diffusion in zeolite is divided two mechanisms; surface diffusion and activated gaseous diffusion in micropores. Gas molecules can either retain their gaseous character in the pores (activated gaseous diffusion) or they are adsorbed on the surface (surface diffusion).[107]

The temperature and pressure dependence of the permeance in porous membranes can be used to characterize the pore size of the membranes in Figure 2.18.[44] Molecular diffusion and activated gaseous diffusion increase with temperature while Knudsen diffusion and viscous flow decrease with temperature. Surface diffusion shows the maximum as a function of temperature. In Figure 2.18 (b) and (c), the permeance from

Knudsen diffusion and activated gaseous diffusion is independent of pressure drop. However, surface diffusion and molecular diffusion is decreasing with increasing pressure. The dependence of the permeance on the temperature and the pressure is an important measure of the quality of membranes.

2.4.1.2.2 Diffusion in zeolite membranes

Three main types of diffusion pathways exist in zeolite membranes: (1) zeolitic pores (5.5Å for silicalite-1), (2) nonzeolitic micropores (size < 10Å), 3) mesopores or macropores (size > 20Å).[102] According to diffusion pathways, three simultaneous transport mechanisms are needed to analyze diffusion of gas molecules through zeolite membranes. Surface diffusion and activated gaseous diffusion occur in zeolitic pores and Knudsen diffusion and viscous flow occur in nonzeolitic micropores or meso-/or macropores.

Nishiyama et al. demonstrated the evaluation method for the silicalite-1 membranes by measuring the permeation of helium and hydrocarbon.[108] It was shown that the permeation in silicalite-1 membranes was divided into the three different contributions such as surface diffusion, activated gaseous diffusion, and viscous flow. For the helium gases, the permeation was governed by activated gaseous diffusion. However, the permeation of alkanes was governed by surface diffusion at low temperature and by activated gaseous diffusion at high temperature.

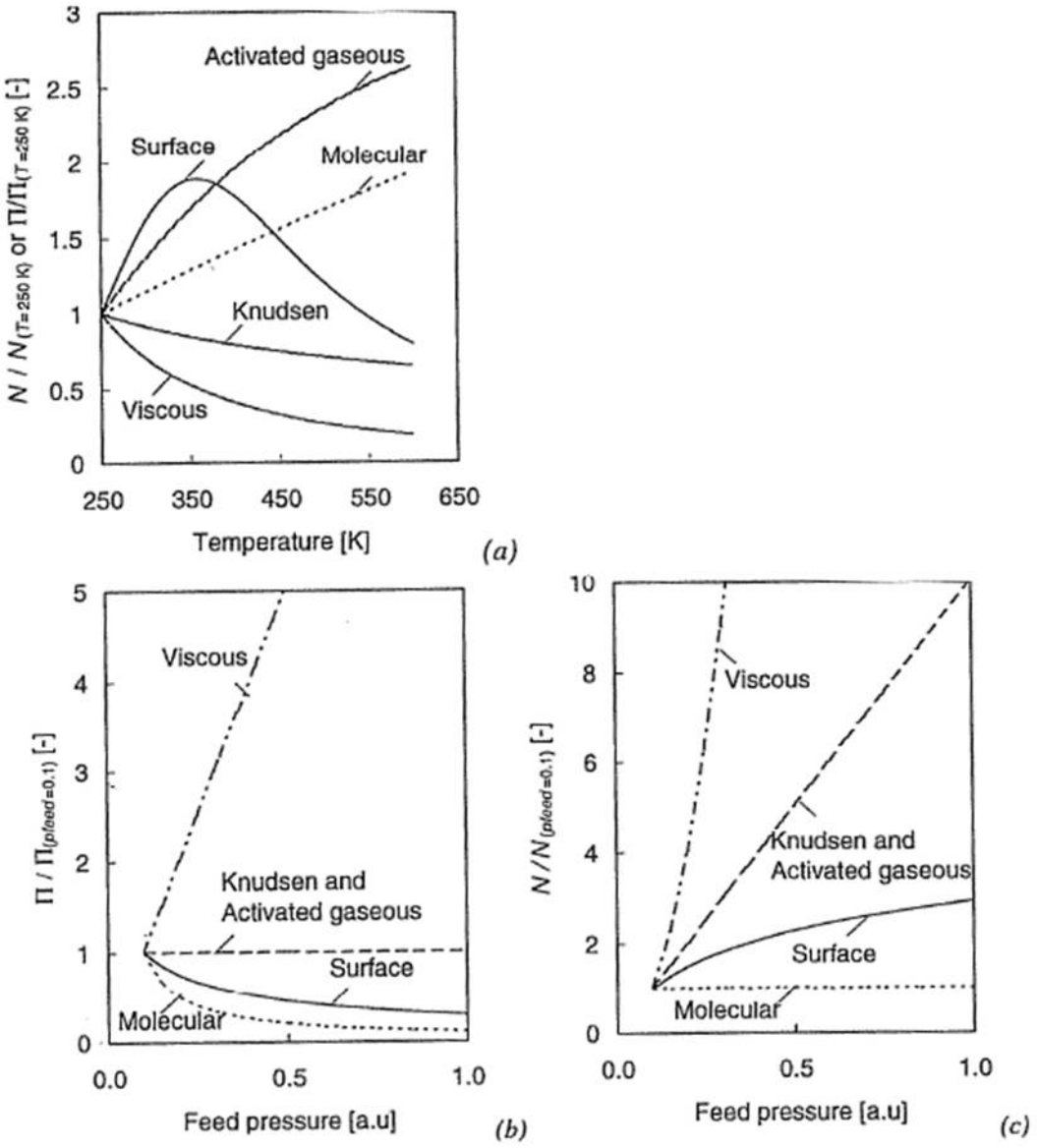

Figure 2.18 (a) Trends in the permeance and the flux as a function of temperature, (b) trends in the permeance as a function of feed pressure, (c) trend in the flux as a function of feed pressure for the viscous flow, the molecular diffusion, the Knudsen diffusion, the surface diffusion and the activated gaseous diffusion. Adapted from Graaf's thesis[44]

2.5 Characterization of zeolite membranes

Rapid identification of the defects or cracks in the zeolite membranes is the key factor for the large-scale industrial applications. Defects are classified according to origin and size. Sources of defects include incomplete growth of crystals, a non-uniform seeding, and thermal stresses during calcination step. The orientation of zeolite crystals, the thickness of the membranes, and the structure of grain boundary may affect the formation of defects.

X-ray diffraction analysis of zeolite membranes on the porous supports is used to characterize orientation of membranes. Scanning electron microscopy (SEM) is the classical technique to evaluate the morphology, thickness, and grain size. Atomic force microscopy (AFM) can be used to study the growth of zeolite films. Transmission Electron Microscopy (TEM) has been less used, but has provided the zeolite structure in the nanoscale, and composition. Fluorescence confocal optical microscopy (FCOM) as a qualitative, non-destructive imaging tool is used to view the polycrystalline features of zeolite membranes.

The measurement of the permeance and selectivity of gas or vapor molecules through zeolite membranes can evaluate the quality of the zeolite membranes. The types of the measurement and methods will be discussed in the next chapter.

2.6 Summary

Zeolite membranes are of great interest due to their unique properties such as 1) size and shape selective separation behavior, and 2) thermal and chemical stability. In the last

decade, significant progress has been made in the synthesis of zeolite membranes. However, there are still many challenges to solve for the large-scale industrial applications. Not only minimization of defects is needed but also enhancement of reproducibility and low cost production. A simple preparation method for zeolite membranes with controlled microstructure is necessary to apply industrial applications since microstructure influences the membrane performance.

CHAPTER III

EXPERIMENT METHODS

3.1 Introduction

This chapter describes general information of the materials and procedures for the two novel synthesis methods: one is for the preparation of *b*-oriented MFI zeolite membranes in Section 3.2 and 3.3; the other is for the monodisperse OMS microspheres in Section 3.4. For the membrane testing, permeance and selectivity will be measured using Time Lag method for single gas molecules and Wicke-Kallenbach (W-K) method for binary mixture will be described in Section 3.5. Characterization methods for the nanoporous materials and their films will be discussed in Section 3.6.

3.2 Synthesis of *b*-oriented MFI zeolite films

3.2.1 Materials

All chemicals were used as received without further purification. Tetraethyl orthosilicate (TEOS, 98 %, Sigma-Aldrich), tetrapropylammonium hydroxide (TPAOH, 1.0 M in H_2O, Sigma-Aldrich), poly(ethyleneimine) (PEI, M_w = 25,000, Sigma-Aldrich) and ethanol (99.5 %, Acros) were used as supplied. Deionized water (DI water) was used throughout the study.

3.2.2 Synthesis of silicalite-1 seeds

Silicalite-1 seeds with the average size of 0.8×0.7×0.4 μm^3 and 2.5×1.8×0.7 μm^3 were synthesized from a gel with the molar ratio of 5TEOS: 1TPAOH: 500H_2O.[6] 5 g of TEOS is introduced into a TPAOH aqueous solution (approximately 4.9 g of 1 M TPAOH in 39.3 g H_2O) under vigorous stirring. The mixture was further stirred for 1 day at room temperature to form a clear solution. Then seeds with the average size of 0.8×0.7×0.4 μm^3 and 2.5×1.8×0.7 μm^3 were synthesized at 130^oC for 12h and at 150^oC for 5h, respectively. Silicalite-1 seeds with the average size of 1.3×1.0×0.5 μm^3 was synthesized from a gel with the molar ratio of 6TEOS: 1TPAOH: 330H_2O.[79] 6 g of TEOS was mixed into a TPAOH aqueous solution (approximately 4.9 g of 1 M TPAOH in 24.6 g H_2O) under vigorous stirring. The mixture was further stirred for 12h at room temperature. Then the mixture was filtered into an autoclave and the synthesis was carried out under rotation at 170^oC for 6h. Silicalite-1 seeds with the average size of 5.0×2.4×0.8 μm^3 was synthesized from a gel with the molar ratio of 5TEOS: 1TPAOH: 100H_2O.[6] 2g of TEOS was mixed into a TPAOH aqueous solution (approximately 2 g of 1M TPAOH in 36 g H_2O) under vigorous stirring for 4h at room temperature. Then the mixture was filtered into an autoclave and the synthesis was carried out with rotating at 175^oC for 3h.

3.2.3 Preparation of PEI film

Silicon wafers or glass substrates were cleaned in a piranha solution (H_2SO_4: H_2O_2 = 3:1) at 120^oC for 1h. PEI films on the substrates were prepared by spin-coating the

substrates with a PEI solution (20 wt% in ethanol). The spinning was carried out at the spinning rate of 3000 RPM for 1 min. The PEI films on the substrates were heated at 110^{o}C for 1h and then were washed in ethanol for 1h to remove PEI residues which didn't bond to the substrates.

3.2.4 Manual assembly of the silicalite-1 seeds on PEI film

The silicalite-1 monolayers were formed according to a previously reported procedure.[79] In short, silicalite-1 seed crystals were poured onto the PEI film coated on a silicon wafer or a glass substrate. The seed crystals were gently pressed and rubbed by a finger. The finger was covered tightly with a clean soft latex glove to avoid contamination of the substrate surfaces and silicalite-1 seed crystals.

3.2.5 Passivation of the flat facets of the silicalite-1 seeds

After calcined for 465^{o}C for 4h, the flat facets of the silicalite-1 seeds were passivated by depositing a thin Au/Pd layer by a metal sputter (Hummer I, Anatech). The thickness of the Au/Pd layer was varied from 5 nm to 50 nm by controlling the deposition times.

3.2.6 Secondary growth and Au/Pd etching

The molar composition of the precursor solution during the secondary growth step was 5TEOS: 1TPAOH: 100H_2O. 2g of TEOS was mixed into a TPAOH aqueous solution (2 g of 1M TPAOH in 36 g H_2O) under vigorous stirring for 4h at room temperature. The

clear solution was filtered into an autoclave. A seeded substrate was placed vertically inside the autoclave with the aid of a custom-made Teflon® holder. The autoclave was placed into a convective oven at the desired temperature. After predetermined time, the autoclave was taken out and quenched in a water bath. After cooling, the sample was collected and washed with a copious amount of DI water. Finally the Au/Pd passivation layers were etched using an Au etchant (Gold Etchant TFA, Transene) for 60 seconds followed by a Pd etchant (Palladium Etchant TFA, Transene) for 60 seconds. The films were thoroughly washed with a copious amount of DI water and dried at 80°C.

3.3 Synthesis of *b*-oriented MFI zeolite membranes

3.3.1 Materials

All chemicals were used as received without further purification. Tetraethyl orthosilicate (TEOS, 98%, Sigma-Aldrich), tetrapropylammonium hydroxide (TPAOH, 1.0M in H_2O, Sigma-Aldrich), aluminum-tri-sec-butoxide (ALTSB, $Al(OC_4H_9)_3$, 97%, Sigma-Aldrich), trimethoxysilypropyl-modified-(polyethylenimine) (TMS-PEI, Gelest), nitric acid (HNO_3, 70%, Fisher Sci.), Polyvinyl alcohol (PVA, average Mw 31,000 ~ 50,000, 85,000 ~ 124,000, and 146,000 ~ 186,000, Sigma-Aldrich) and ethanol (99.5%, Acros) were used as supplied. Deionized water was used throughout the study.

3.3.2 Preparation of α-Al_2O_3 porous substrates

A *α*-alumina porous disc with 2 mm in thickness and 22 mm in diameter was prepared by pressing alumina powder (Baikowski International Corp. CR6 grade). The

α-alumina porous discs were sintered at 800^{o}C for 30 h with 1^{o}C/min of ramping rate and heated up to 1200^{o}C for 4 h with 1^{o}C/min of ramping rate. One side of disc was polished sequentially using sandpapers #320, #600, and #800, each for 5 min. Figure 3.1 shows the properties of the porous α-Al_2O_3 supports made in our lab. The porosity and the average diameter of the α-Al_2O_3 supports are 43% and 0.15 μm, respectively.

3.3.3 Preparation of γ-alumina film

The γ-alumina films are prepared on the α-Al_2O_3 porous supports by slip coating. The Al precursor solution was prepared by hydrolization of aluminum butoxide (ALTSB) with water. Then the mixture was carried out peptization with acid using molar composition of 1ALTSB: 100H2O: 0.1HNO_3. 65 ml of ALTSB was adding gradually into 450 ml of water at 90^{o}C. The solution was then refluxed at 90^{o}C for 1 hour under vigorous stirring. In order to peptize the solution, 25 ml of HNO_3 was added and refluxed at 90^{o}C for 24 hour. The peptized sol was cooled steadily down to room temperature to enable hydroxylation, alkoxilation, or condensation. 30 ml of PVA polymer solution was added into 70 ml of the peptized sol to make the final Al-boehmite gel solution.

A boehmite sol solution was coated on the porous supports through a procedure schematically in Figure 3.2. The boehmite sol was poured into a Petri-dish that was placed on a height-adjustable jack.

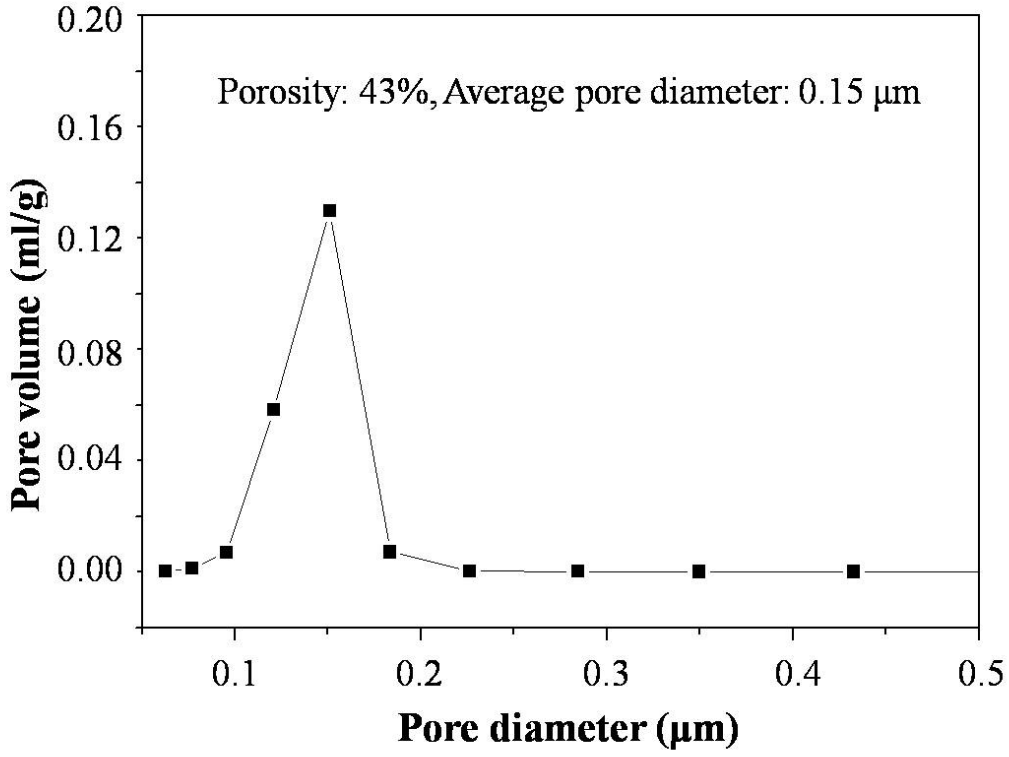

Figure 3.1 The porosity and average pore diameter of the α-Al_2O_3 supports

The boehmite sol was slowly raised toward the polished surface of an inverted α-Al_2O_3 disc until the support soaked the sol solution. The support was left in contact with the sol solution for 10 seconds and was removed tangentially to vertical position. And then the support was placed parallel to the ground until the solvent was completely evaporated. The γ-alumina films were then heated up 465^{o}C for 4 hours to make mesopores in the γ-alumina film.

3.3.4 Preparation of PVA film

A porous α-alumina disc was cleaned under O_2 plasma for 5 min. The PVA film on the substrates was prepared by spin-coating on the surface of the α-alumina discs. The PVA solutions were prepared with three different average molecular weights (Mw 31,000 ~ 50,000, 85,000 ~ 124,000, and 146,000 ~ 186,000) to find the good quality of PVA films. The concentration of PVA solution was fixed at 5% of weigh percent in the water. The spin coating was carried out at the spinning rate of 3000RPM for 1min. The PVA films on the porous supports were heated at 120^{o}C for 30 min. In order to make continuous PVA films on the porous support, spin coating was repeated a couple of times until the surface of the α-alumina porous disc was covered completely by PVA.

3.3.5 Preparation of TMS-PEI film

A TMS-PEI film on the PVA layer was prepared by spin-coating with the TMS-PEI solution (5 wt % in ethanol). The spin coating was carried out at the spin rate of 3000 RPM for 1min. Then, TMS-PEI film was heated at 110^{o}C for 45 min.

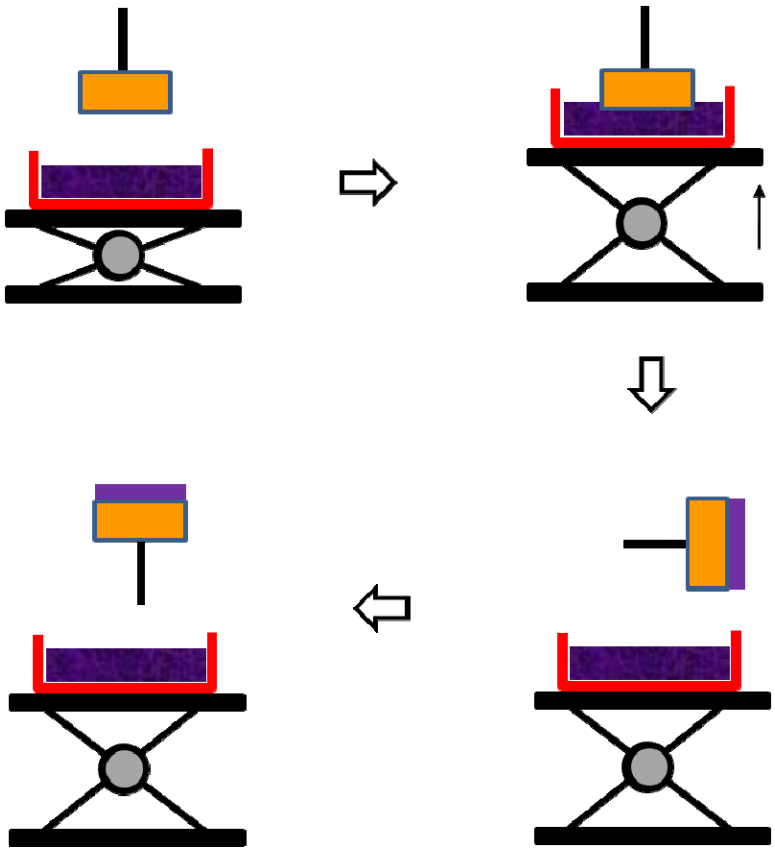

Figure 3.2 Schematic procedure for γ-alumina films by slip coating method

3.3.6 Seeding, Au passivation, and secondary growth

Silicalite-1 seed crystals were deposited on the porous α-alumina supports by manual assembly. After calcined at 465^{o}C for 8h, the flat facets of the silicalite-1 seeds were passivated by depositing a thin Au/Pd layer by a metal sputter (Hummer I, Anatech). The thickness of the Au/Pd layer was controlled by the deposition times. To make continuous silicalite-1 membranes, secondary growth was carried out at proper temperature. A molar composition of the precursor solution during the secondary growth step was 5TEOS: 1TPAOH:100H_2O. Finally Au/Pd passivation layers etched out using an etching solution (3HCl: 1HNO_3: 2H_2O) and washed with a DI water. The silicalite-1 membranes were dried at 80^{o}C prior to measurement of the permeation.

3.4 Synthesis of OMS microspheres in a microfluidic device

3.4.1 Materials

All chemicals were used as received without further purification. Tetraethylorthosilicate (TEOS) and Sigmacote® were purchased from Sigma-Aldrich. Hexadecane (98%) and acetone (99.5%) were supplied by Fisher chemicals. Ethanol (99.5%) and isopropanol (99.5%) were acquired from Acros. Span®80 (sobitan monoloeate, visocosity 1200 ~ 2000mPa·s at 20^{o}C) was supplied by Fluka. Poly (dimethylsiloxane) elastomer (Sylgard 184) was purchased from Dow corning. P135 (a polymeric PEG-30 dipoly(hydroxysterate)) was kindly provided by Uniquema. All Pluronic block copolymers (L121, P104, P105 and F108) used in this study were obtained as gifts from BASF Corp. (Parispany, NJ).

3.4.2 Preparation of precursor solution

Typical mesoporous silicate precursor solution was prepared by hydrolyzing 5.2g TEOS in the mixture of 6g ethanol and 2.7g dilute hydrochloric acid (0.07M, pH 2) solution under vigorous stirring at room temperature for 20min. 0.8g of P104 (a pluronic block copolymer) was dissolved in 8g of ethanol before being mixed with the hydrolyzed TEOS solution. The final molar ratio was 1TEOS: 0.005 P104: 12.174 Ethanol: 0.0176 HCl: 5.97 H_2O.

3.4.3 Fabrication of PDMS microfluidic devices

PDMS microfluidic devices were fabricated using a soft lithography procedure.[37] These devices were made of rectangular channels of 100μm height and 100μm width. The flow focusing point of the devices was decreased to 50μm. The PDMS devices were placed on glass slides coated with PDMS films to ensure that precursor only contacts to the PDMS surfaces. In order to prevent the precursor solution from wetting on the PDMS surface, the surface of PDMS was coated with Sigmacote®, a water-repellant.

3.5 Permeance measurement

3.5.1 Time lag method for single gas permeance

The average kinetic diameters of gas molecules measured in this study are listed in Table 3.1.[109] The permeance of single gas molecules were measured in a custom-made permeation cell using a time-lag method[110]. The time-lag is the amount of time required for a gas to permeate through a membrane.

Table 3.1 The kinetic diameters of gas molecules[109]

Molecule	Kinetic diameter: d_k(nm)
He	0.260
H_2	0.289
O_2	0.346
N_2	0.364
CH_4	0.380
CO_2	0.330
SF_6	0.550

There are two methods for obtaining the time-lag; one is a differential technique and the other is an integral method. In this study, we used the integral method to obtain the permeance of the gas molecules. The integral method monitors increasing pressure caused by accumulation of permeating gas through membrane in the evacuated chamber as a function of time. The chamber is initially degassed by vacuum and separated from the gas in feed side by a membrane.

The setup for single gas permeation is schematically shown in Figure 3.3. The Permeation cell is separated two parts (feed side and permeate side) by a zeolite membrane. At the permeate side, one port is connected to volume chamber which is subsequently lined to vacuum pump, and the other port is cupped. The pressure of the volume chamber is monitored by computer. Before measurement of permeance, the feed side is flushed with the gas molecules at about 1 ~ 2 bar and the permeate side is evacuated to a vacuum. The experiment is started when the inlet gas stream at the feed side is shut off. From this time, the pressure in the volume chamber at the permeate side increase and is monitored by a computer. The permeance (Π) of gas molecules through zeolite membranes can be calculated using following equations.

The flux (J) of gas molecules through the membrane is given by the following expression.[110]

$$J = \frac{Slope}{RT} \cdot \frac{V}{A} \quad (1)$$

The slope within the steady-state region is obtained during a permeation experiment by plotting the pressure of the chamber as function of time. In the equation (1), V is the volume of the chamber, A is the area of membrane, R is the ideal gas constant, and T is

the temperature of the experiment. Then, the permeance of gas molecules is calculated by the equation (2).

$$\pi = \frac{J}{\Delta P} \cong \frac{J}{P_2} \quad (2)$$

In the equation (2), ΔP is the pressure difference between at the feed side (P_2) and at the permeate side (P_1). The pressure of permeate side (P_1) is much smaller than one of the feed side because the permeate side is evacuated to a vacuum. Thus, P_1 can be ignored in the equation so that ΔP can be replaced to P_2.

3.5.2 Wicke-Kallenbach (WK) method for binary gas permeance

Binary gas permeation experiments were carried out by the WK method shown in Figure 3.4. Xylene isomers (*p*- and *o*-xylene) were mainly used to evaluate the performance of our MFI silicalite-1 membranes. At the feed side, two gas bubblers were used for each *p*- and *o*-xylene isomer. The xylene isomers are made up the feed stream with the sweep gas (He). A mixture of feed stream was balanced to 101kPa by Helium gas with the flow rate of around 50ml/min. At the permeate side, a pure sweep helium gas was used with the flow rate of around 50ml/min. The concentration of the component through a zeolite membrane was analyzed by Agilent 7890C Gas Chromatograph equipped FID detector with a capillary column (DB-WAX, Agilent).

3.5.2.1 Calibration of xylene isomers from GC data

Calibration curves of xylene isomers are needed to determine the concentration of xylene isomers prior to the permeation experiments.

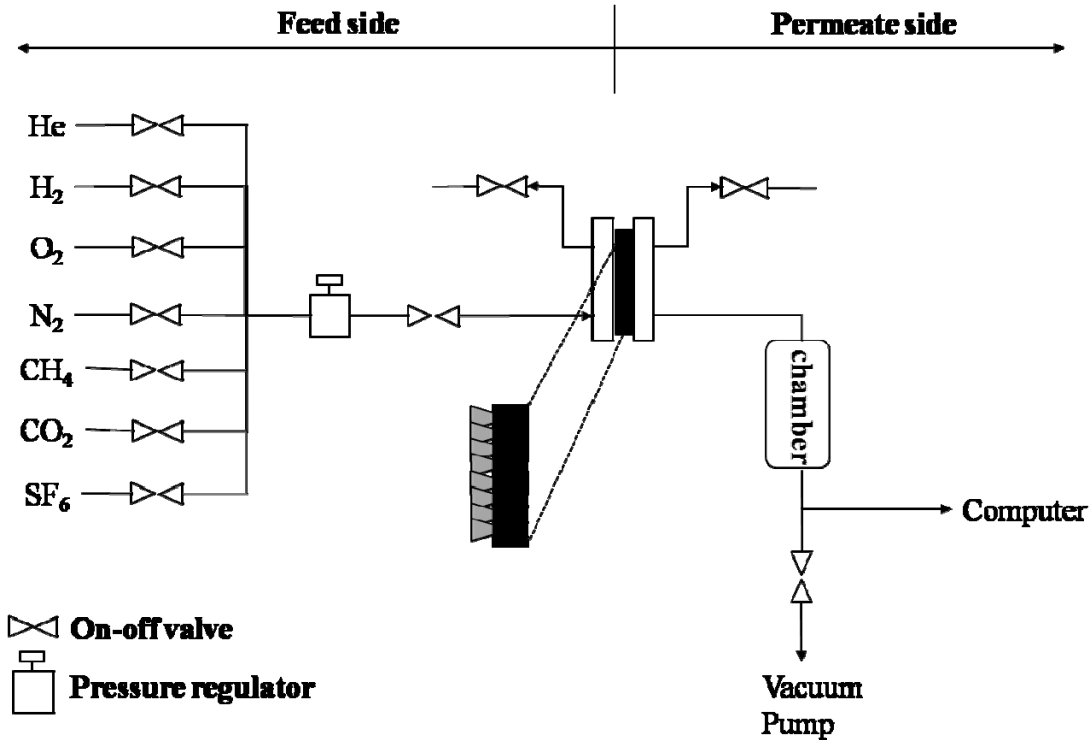

Figure 3.3 Single gas permeation setup

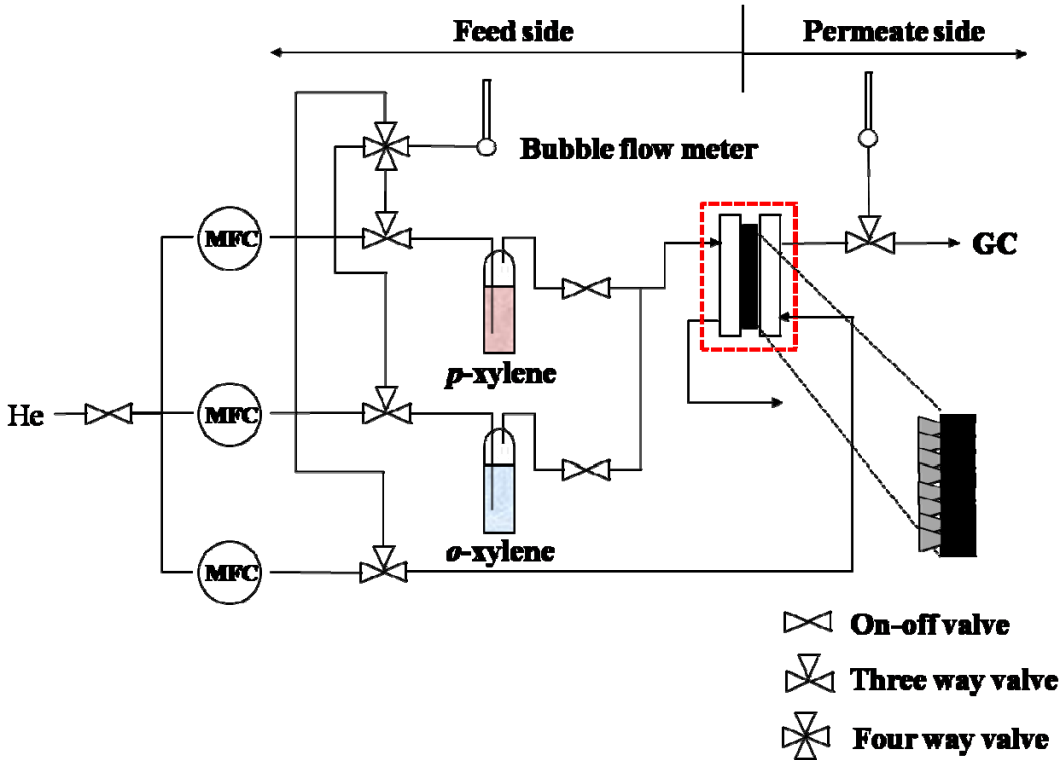

Figure 3.4 Binary gas permeation setup

Calibration curve was obtained to plot the areas of the FID peaks as function of the partial pressures of xylene isomers. Table 3.2 showed the design of the experiment for the calibration curve of the *p*-xylene and the *o*-xylene, respectively. The partial pressures of xylene isomers were adjusted by changing flow rates of xylene isomers and He gas. The total flow rate of the mixture in the calibration experiments should be the same as the total flow rate of the permeation experiments. The GC measurements for the calibration were repeated 3 times at each condition and the calibration graphs were plotted as shown in Figure 3.5. The graphs showed linear relationship with R^2 around 0.99.

3.5.2.2 Calculation of permeance

Permeance of xylene isomers through zeolite membranes are calculated in this section using following equations. Permeance is a function of the flux and the difference of the partial pressures of between feed and permeate side.

$$\pi_1 = \frac{J_1}{\Delta P_1} \quad , \quad \pi_2 = \frac{J_2}{\Delta P_2} \tag{3}$$

$$\Delta P_1 = P_{1,F} - P_{1,p} = P_{1,F}^{sat} - P_{1,P}^{sat}$$

$$\Delta P_2 = P_{2,F} - P_{2,p} = P_{2,F}^{sat} - P_{2,P}^{sat} \tag{4}$$

In equation (3), π is the permeance, J is the flux of components, and ΔP is the difference of the partial pressures. Number 1 in the parameters represents to *p*-xylene and number 2 represents to *o*-xylene.

Table 3.2 Design of the experiment to obtain the calibration curve

No	p-xylene				o-xylene			
	Flow rate (ml/min)			Partial pressure (Pa)	Flow rate (ml/min)			Partial pressure (Pa)
	p-xylene	He	Total		o-xylene	He	Total	
1	7.73	44.66	52.49	156.65	7.83	45.0	52.83	116.30
2	16.60	36.19	52.79	330.22	16.60	36.39	52.99	245.82
3	25.97	26.58	52.55	518.97	25.97	27.09	53.06	384.07
4	52.58	0	52.58	1050.13	52.61	0	52.61	784.70

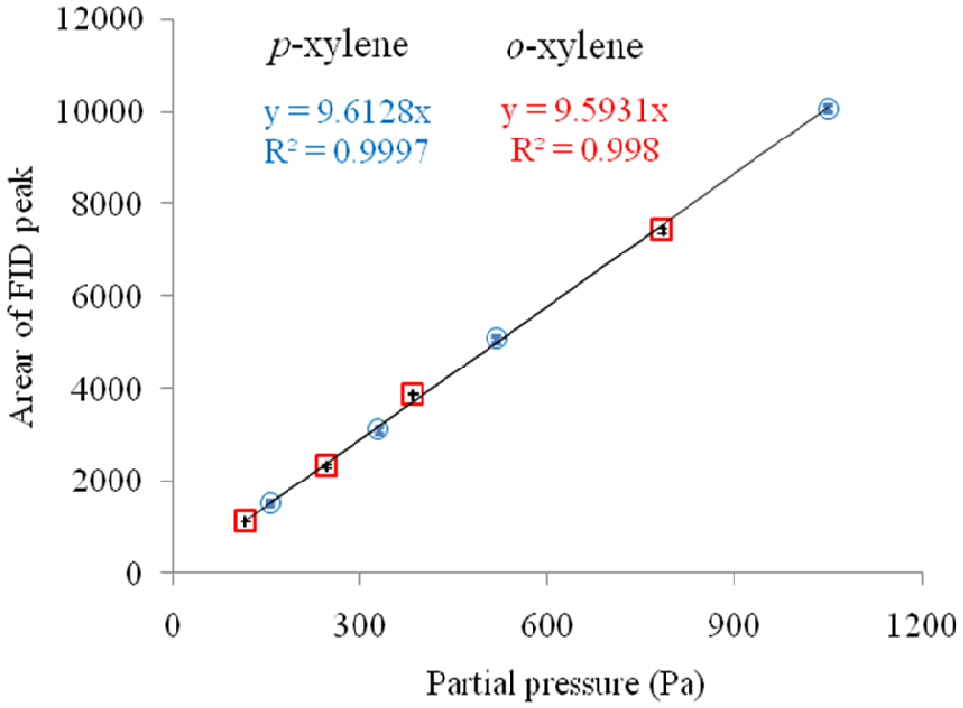

Figure 3.5 Calibration curve xylene isomers: circle symbol represents *p*-xylene and square symbol *o*-xylene

At the feed side, the partial pressure of *p*-xylene ($P_{1,F}$) is equal to the saturated vapor pressure of *p*-xylene at given temperature. The vaporization of xylene isomer in the experiments was carried out at 23°C. We took the saturated vapor pressures of each xylene isomers from the thermodynamic Vapor-Liquid-Equilibrium data.[111] At the permeate side, the partial pressure of p-xylene ($P_{1,P}$) can be ignored due to continuous sweep gas of He. Equation (4) can be simplified as in the equation (5).

$$\Delta P_1 = P_{1,F}^{sat}$$

$$\Delta P_2 = P_{2,F}^{sat} \tag{5}$$

The flux of p-xylene through a zeolite membrane was obtained using the equations (6).

$$J_1 = \frac{\dot{n_1}}{A}, \quad J_2 = \frac{\dot{n_2}}{A} \tag{6}$$

In the equation (6), ṅ is the molar flow rate and A is the effective membrane area. To calculate the flux, it is assumed that xylene isomers act as the ideal gas. The molar flow rates of xylene isomers through membranes can be calculated by equation (7).

$$\dot{n_1} = \frac{P\dot{v_1}}{RT} = \frac{P\dot{V_T}y_1}{RT} = \frac{PV_T\frac{\dot{p}_1}{P}}{RT} = \frac{V_T P_1}{RT}$$

$$\dot{n_2} = \frac{P\dot{v_2}}{RT} = \frac{P\dot{V_T}y_2}{RT} = \frac{PV_T\frac{\dot{p}_2}{P}}{RT} = \frac{V_T P_2}{RT} \tag{7}$$

In the equation (7), P is the total pressure at permeate side, v̇ is the volume flow rate, y is the mole fraction, V_T is total volume flow rate through a membrane, p is the partial pressure of xylene at the permeate side through membrane, R is the gas constant, and T is the temperature of the permeation measurements. Table 3.3 shows the example to calculate the permeance of xylene isomers using those equations.

Table 3.3 Example for the calculation of permeance

	p-xylene	*o*-xylene
Area of the FID peak	244	32
Partial pressure (Pa)[1]	26.132	3.437
Molar flow rate (mole/s)[2]	$\dot{n_1} = \frac{V_T P_1}{RT} = \frac{52*10^{-6}\cdot 26.132}{8.314\cdot 298.15\cdot 60} = 8.83 \times 10^{-9}$	$\dot{n_2} = \frac{V_T P_2}{RT} = \frac{52*10^{-6}\cdot 3.437}{8.314\cdot 298.15\cdot 60} = 1.16 \times 10^{-9}$
Flux (mole $\cdot$ m^{-2} $\cdot$ s^{-1}) [3]	$J_1 = \frac{\dot{n_1}}{A} = \frac{8.83 \times 10^{-9}}{3.14 \times 10^{-4}} = 2.8 \times 10^{-5}$	$J_2 = \frac{\dot{n_2}}{A} = \frac{1.16 \times 10^{-9}}{3.14 \times 10^{-4}} = 3.7 \times 10^{-6}$
Permeance[4] (10^{-10} mole m^{-2}s^{-1}Pa^{-1})	$\pi_1 = \frac{J_1}{\Delta P_1} = \frac{2.8 \times 10^{-5}}{460} = 608$	$\pi_2 = \frac{J_2}{\Delta P_2} = \frac{3.7 \times 10^{-6}}{460} = 80$

[1] The partial pressure is obtained using calibration curve
[2] Total flow rate: 52 ml/min, temperature: 25oC
[3] Diameter of membrane: 20 mm
[4] Partial pressure at feed side: p-xylene = 0.46kPa, o-xylene=0.46kPa

3.6 Analytical methods

3.6.1 Electron microscopy

Scanning Electron Microcopy (SEM, JEOL JSM-6400) was taken the images of zeolite membranes and OMS microspheres to evaluate the morphology, thickness, and grain size. Energy dispersive X-ray spectroscopy (EDS, JEOL JSM-6400) was used for analyzing the amount of Au and Pd elements left after removal of passivation layer by etching process. Mesostructure of OMS microspheres was characterized by Transmission Electron Microscopy (TEM, JEOL JEM-2010) operated at 200 kV.

3.6.2 X-ray diffraction

X-ray diffraction analysis of zeolite membranes was used to characterize an orientation of membranes. X-ray diffraction (XRD) measurements were carried out on a RigaKu MiniFlex^{TM} II with Cu-Kα radiation (λ = 1.54Å). The internal mesostructure of OMS microspheres was confirmed by measuring a small angle X-ray scattering (SAXS, Bruker-AXS) with Cu-Kα radiation (λ = 1.54Å).

3.6.3 Optical microscopy

The silicalite-1 seed layers and membranes as well as OMS microspheres were imaged using an optical microscope (Axiovert 200M, Zeiss).

CHAPTER IV

B-ORIENTED MFI SILICALITE-1 THIN FILMS BY THE MICRO-TILES-AND-MORTAR METHOD*

4.1 Introduction

Since zeolite membranes are polycrystalline in nature, their microstructure plays an important role in determining their performance as membranes.[39] Therefore, controlling the microstructure of zeolite membranes such as the size and orientation of the grain and grain boundary structures has great implications.[3, 5, 40] It has both experimentally[39, 103] and computationally[104] been demonstrated that *b*-oriented MFI membranes show superior performance for organic vapor separations. Lai et al.[39] experimentally showed that the selectivity of *p*-xylene (kinetic diameter ~ 0.58 nm) over *o*-xylene (kinetic diameter ~ 0.68 nm) through their b-oriented MFI membranes was unprecedented (above 450) while the permeance of the membranes approached to that of the porous alumina support. This unprecedented increase in the membrane performance has been attributed to two main factors: 1) channels are straight along the b-axis, thus effectively enhancing selective intracrystalline diffusion of molecules and 2) *b*-oriented membranes result in better grain structures as compared to those of membranes with other orientation, thus effectively reducing non-selective intercrystalline diffusion of molecules through the

* Reprinted with permission from "mu-Tiles and mortar approach: A simple technique for the facile fabrication of continuous b-oriented MFI silicalite-1 thin films" by I. Lee, J.L. Buday, and H.-K. Jeong, Microporous and Mesoporous Materials 2009, 122, 288-293. Copyright 2009 by Elsevier B.V.

grain boundary. In addition, better grain structures result in improved resistance to crack formation during the organic template removal step via calcination.

Several groups have reported *b*-oriented ZSM-5 membranes by both in situ and secondary growth methods.[7-12] However, Tsapatsis' group is the first to report the permeation results for b-oriented MFI membranes which were prepared by a secondary growth (i.e. seeded growth) method.[6, 13] In order to make their b-oriented MFI membranes, they first prepared b-oriented seed layers on mesoporous silica-coated α-Al_2O_3 substrates using a chemical interaction-based method developed by Yoon's group.[112] They then engineered relative growth rates along each crystallographic direction by using custom-made organic templates (so called, dimer-TPA and trimer-TPA),[113] such that the growth rate along the b-axis is comparable to that along the c-axis while significantly faster than that along the a-axis. By doing so, they were able to preserve the crystallographic orientation of the zeolite seed crystals during the secondary growth process. Later, the same group reported a-oriented MFI membranes using the same strategy.[114] Despite the remarkable performance of their b-oriented MFI membranes, the complexity of their manufacturing process (i.e. time-consuming preparation steps and the need for organic solvents and template synthesis) makes it difficult to produce high performance b-oriented MFI membranes in a reproducible and cost-effective way for the commercial application.

Apart from control of the preferred crystal orientation, there are a number of challenges that need to be addressed to find more commercial applications of zeolite membranes, particularly MFI membranes.[3, 40] Some of these challenges include: 1)

synthesis of membranes with high permeability and selectivity (i.e., oriented, thin layers and small effective thicknesses) in a commercially viable manner, 2) reproducibility and long-term stability of membrane performance, 3) scaling-up of membrane modules, 4) cost of membranes (i.e. manufacturing cost and substrate cost), and 5) easy crack healing during membrane operation.

We demonstrate a novel synthesis method which enables the fabrication of *b*-oriented MFI thin films and membranes in a simple manner with the potential to address some of the current engineering challenges listed above. The new fabrication method is analogous to a macroscopic tiling process, i.e. assembling tiles and jointing them with mortar.[5] This method (see the Figure 4.1) involves three main steps: 1) rapidly assembling *b*-oriented MFI micro-crystals on the substrates using manual assembly[79] (i.e. direct assembly by rubbing crystals on functionalized surfaces), 2) passivating the out-of-plane crystal faces, i.e. the (010) faces, to prevent the nucleation and growth of the crystals in the out-of-plane direction while allowing the growth of the crystals in the in-plane direction, and lastly 3) filling the gaps between the MFI micro-tiles by allowing the crystals to grow only in the plane while preventing out-of-plane growth. The key to successful secondary growth is to promote the in-plane (parallel to the support) growth of the zeolite tiles so as to eliminate intercrystal gaps and generate a continuous film while preventing the out-of-plane (perpendicular to the support) growth and nucleation of mis-oriented grains. In addition, since one can calcine templates before the formation of continuous thin films, our method does not require the template removal step using a

high temperature calcination process, thus avoiding the potential crack-formation during this process.

4.2 Experimental

MFI silicalite-1 films on the silicon wafer were synthesized by our novel micro-tiles-and-mortar method that was modified secondary growth method. The synthesis of seed crystals, seeding, passivation of faces of seed crystal layer, and secondary growth are described in subsection 3.2 in detail.

4.3 Results and discussion

Figure 4.1 illustrates the procedure to synthesize *b*-oriented MFI thin films on glass or silicon wafer substrates. First, plate-like MFI seed crystals were hydrothermally synthesized following procedures reported in the literature.[6, 79, 115] To achieve *b*-oriented seed crystal layers, the seed crystals were then manually assembled onto substrates (tethered with poly(ethyleneimine) (PEI), a polymeric electrolyte, as a linker) by simply rubbing the crystals onto the substrates following the procedure developed by Yoon and his coworkers.[79] This step typically takes only a few minutes depending on the size of the substrate and does not require organic solvent. In contrast, it takes several hours with multiple surface functionalization and cleaning steps to make seed layers using the so called "reflux and stirring" method used by Lai et al.[6, 13]

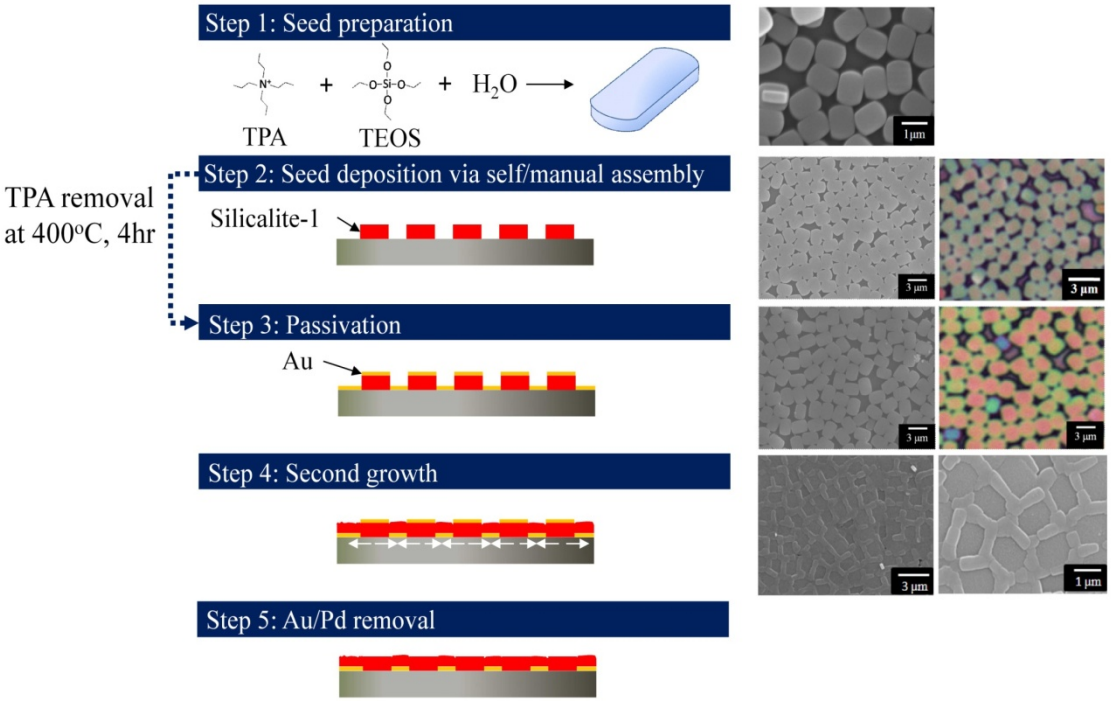

Figure 4.1 Schematic illustration of the micro-tiles-and-mortar approach: 1) hydrothermal synthesis of plate-like uniform MFI seed crystals, 2) manual assembly of a b-oriented seed layer on a PEI-coated substrate and calcination of organic templates, 3) sputtering a Au/Pd passivation layer on the seed layers, 4) secondary growth of the seed crystals, and 5) removal of Au/Pd layers in etchant solutions

The silicalite-1 monolayer was then calcined at 400^{o}C for 4 hrs to remove the organic template, tetrapropylammonium (TPA), thus activating the channels of the crystals. It is worth mentioning here that since the highly packed seed crystals with about 95% of surface coverage were calcined before being grown into continuous films, the final calcination process of zeolite films may not be necessary if one is willing to sacrifice a small reduction (about 5%) in total mass flow. This avoidance of the calcination of continuous zeolite films at high temperature may have significant practical implications since typically the calcination step to remove templates from pores of zeolite membranes is time-consuming and oftentimes leads to crack formation in zeolite membranes even with very careful temperature programming.[40, 116, 117] Thin Au/Pd layers were then sputtered onto the MFI silicalite-1 monolayer to prevent the seed crystals from growing out-of-plane along the b-axis. The *b*-oriented MFI silicalite-1 monolayer was finally hydrothermally grown to fill the gaps between the crystals by secondary growth.

The key feature of our method is to passivate the out-of-plane crystal faces, i.e., the (010) faces, with thin Au/Pd layers to prevent the nucleation and growth of the seed crystals in the out-of-plane direction while allowing the growth of the seed crystals in the in-plane direction. In a typical synthesis of MFI silicalite-1 with monomer-TPA as a template, the growth along the *a*- and *c*-axis (the in-plane direction) is much faster than along the *b*-axis (the out-of-plane direction).[5] Thus one may expect that during the secondary growth of the *b*-oriented seed layers, the intercrystal gaps can be reduced with slight increase in the thickness of membranes. However, as reported by Lai et al.[6] this is

not the case due to the substantial twinning process, which produces 90°-intergrown parasitic crystals on the (010) planes of the mother crystals with their *a*-axis perpendicular to the *b*-faces. Since the crystals grow along the *a*-axis much faster than along the *b*-axis, even with highly *b*-oriented seed layers, membranes with *a*-oriented top layer and *b*-oriented bottom layer are obtained. In order to address this issue, two approaches are possible: 1) increasing the growth rate of MFI seed crystals along the *b*-axis relative to the *a*-axis or 2) preventing the out-of-plane nucleation and growth of the MFI crystals. The first approach was taken successfully by Tsapatsis' group where dimer- and trimer-TPA molecules were used as templates to manipulate the relative crystal growth rates along different crystallographic axes.[6, 13, 113] In this dissertation, we take the second approach where a thin Au/Pd layer was sputtered to passivate the (010) faces of the MFI seed crystals. Figure 4.2 shows the growth of a *b*-oriented seed layer that was manually assembled on a silicon wafer with a 50 nm thick Au/Pd passivation layer (bottom) as compared to that without a passivation layer (top). As can be clearly seen in the figure, without the passivation layer the crystals nucleate and grow in the plane as well as out of the plane after 1h of secondary growth at 175°C. After 2h of secondary growth, substantial numbers of twinned crystals have already formed. With the passivation layer, however, the nucleation and growth of the MFI crystals from the passivated flat faces is prohibited even after 2h of secondary growth while the nucleation and growth of the crystals is allowed in the plane, thus filling the intercrystal gaps without forming twinned crystals.

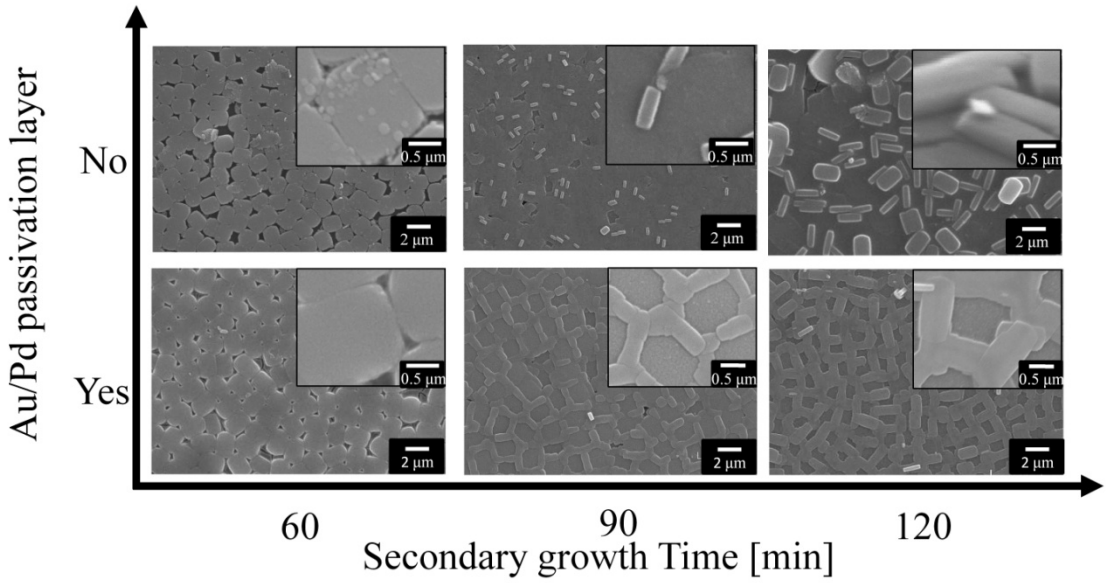

Figure 4.2 Effect of the presence of the Au/Pd passivation layers on the secondary growth of seed crystals: SEM images of MFI films prepared with the Au/Pd layer and without the Au/Pd passivation layers at 175 ^{o}C for various growth times

The cross-sectional view of a *b*-oriented MFI film with a passivation layer shows that the gaps are filled due to the in-plane growth of the seed crystals as shown in Figure 4.3. It also reveals that the thickness of the film is essentially the same as the seed crystals, thereby revealing potential capability of making submicrometer thick *b*-oriented MFI membranes. The ability to synthesize submicron thick *b*-oriented MFI membranes is of practical importance since the flux is inversely proportional to the membrane thickness. X-ray diffraction patterns of both films show substantial out-of-plane orientation along the *b*-axis as shown in Figure 4.4. Interestingly, there was no noticeable difference in the diffraction patterns of both films prepared with and without passivation layers. This is due to the fact that the (010) planes perpendicular to the substrate of the film significantly outnumbers the (100) planes of twinned crystals, thus the diffractions are not resolved (the Bragg angles of (010) and (100) planes are very close).

In order to prevent the seed crystals from growing out of the plane while allowing them to grow in the plane, the deposition of a passivation layer is critically important as described above. Metal sputtering has been chosen since sputtering enables the line-of-sight deposition of materials (i.e. planes facing the target will be preferentially deposited) as opposed to metal evaporation.[118] Even though the metal deposition via sputtering is line-of-sight, it is expected that if the metal layers are too thick there might be metal deposited on the planes of MFI seed crystals perpendicular to the substrate (i.e. the (100) and (001) faces). Indeed, the thinner the Au/Pd passivation layers are, the faster the in-plane growth is observed to be as shown in Figure 4.5).

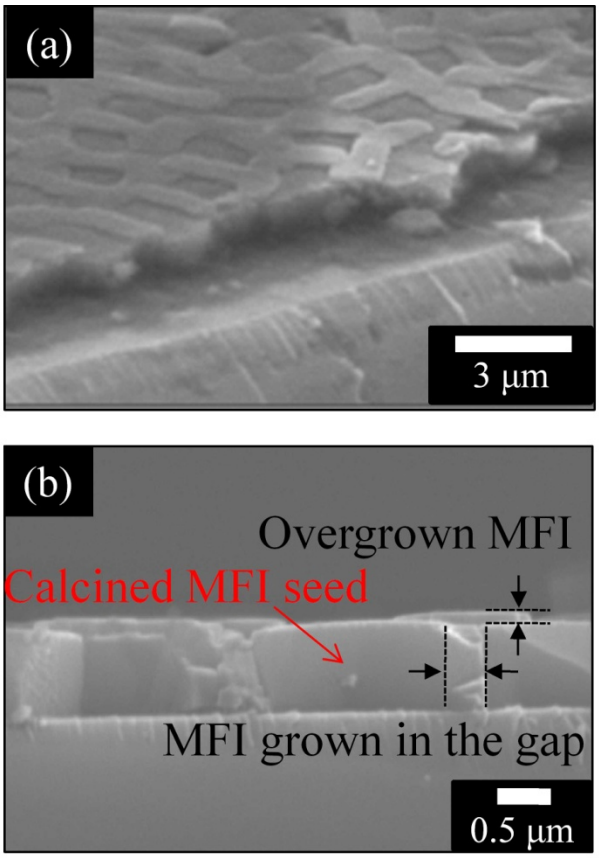

Figure 4.3 Cross-sectional views of b-oriented MFI films with a passivation layer: (a) lower magniciation and (b) higher magnification. The secondary growth was carried out at 175 ^{o}C for 90 min

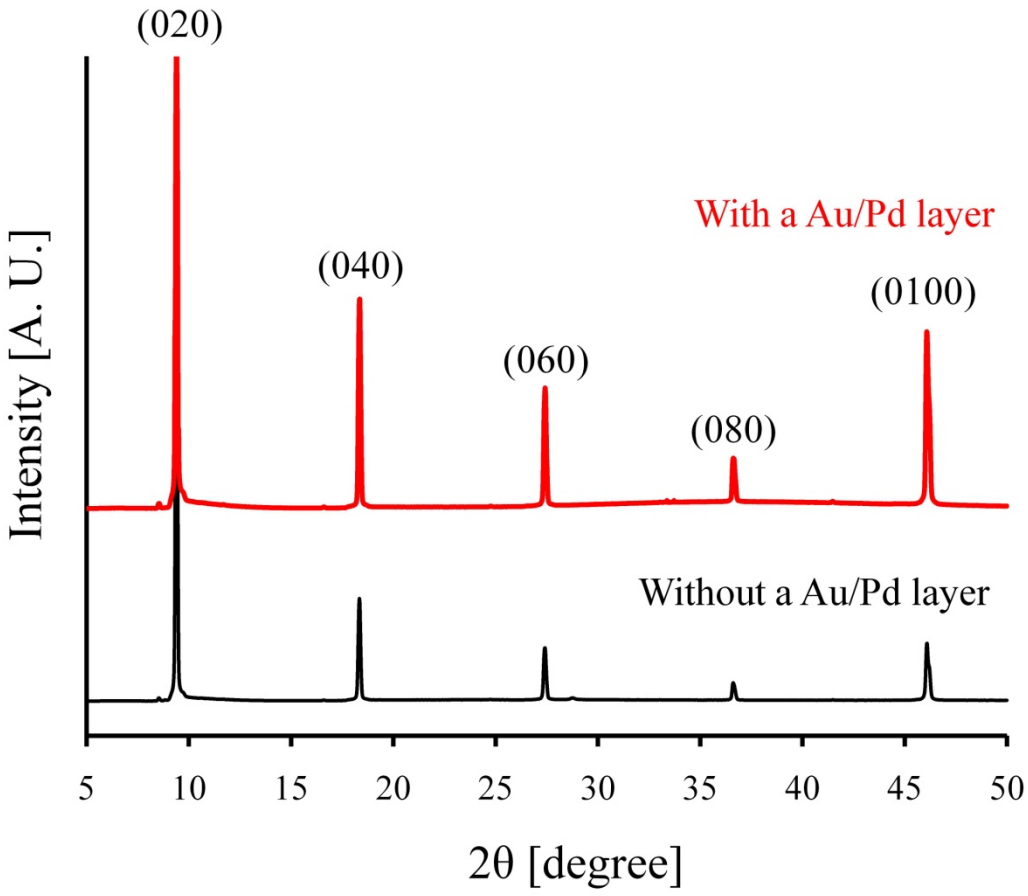

Figure 4.4 X-ray diffraction patterns of MFI films with and without Au/Pd passivation layers. The diffraction pattern of the MFI film prepared with the passivation layer is in red, whereas that of the film without the passivation layer is in black. Both of the samples were grown at 175^{o}C for 90 min

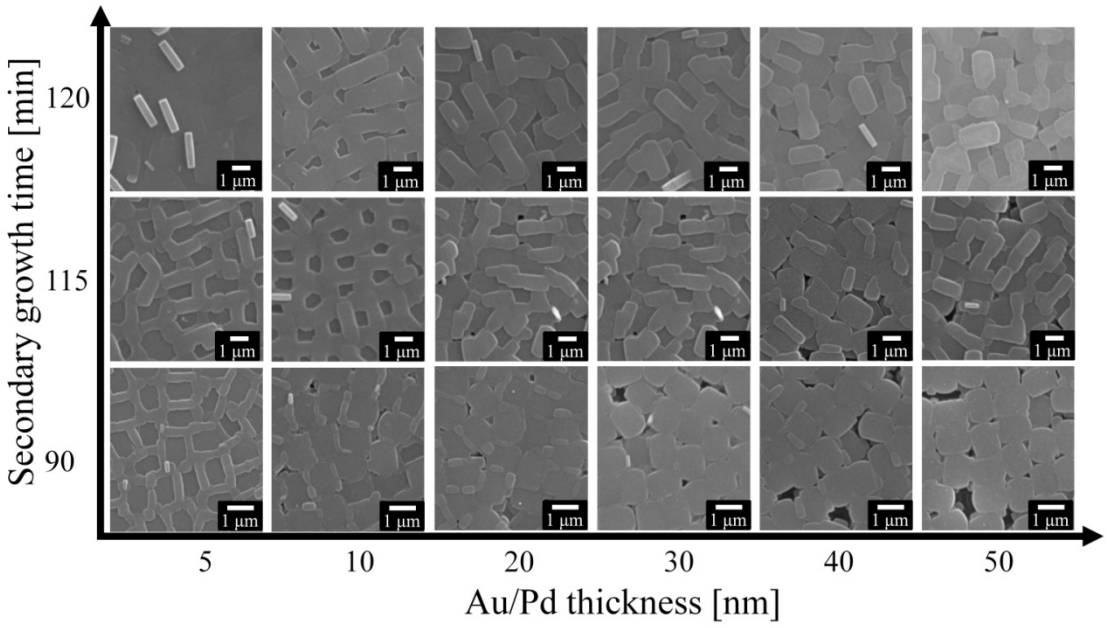

Figure 4.5 The effect of the thickness of the passivation layers on preserving the orientation of seed layer during the secondary growth at 175^{o}C for various growth times

The microstructure of grain boundaries has a substantial effect on the performance of membranes.[6] This is the case because of 1) non-selective intercrystalline diffusion (i.e. diffusion through the grain boundary) as well as 2) resistance to crack formation during the calcination process is determined by grain microstructure. In this regard, it is of great interest to control the number density of grain boundaries. The lower the number density of grain boundaries, the smaller the contribution of non-selective intercrystalline diffusion and the greater the resistance to crack formation during the template removal process via calcination. In our method, control of the density of grain boundaries can be easily achieved by varying the size of the seed crystals (0.8 μm, 1.7 μm, 2.5 μm, and 5.0 μm) as presented in Figure 4.6. With seed crystals of smaller size (0.8 and 1.3 μm), the degrees of close packing (DCP) and surface coverage (DSC) were better, thereby enabling the preparation of continuous films in a shorter growth time. Meanwhile, bigger seed crystals result in a bigger single crystal domain, i.e. lower density of grain boundaries which is therefore beneficial for membrane performance due to the reduced contribution of non-selective intercrystalline diffusion. However, with bigger seed crystals the intercrystalline gaps are bigger, which requires longer time to fill the gaps. In addition, the seed crystals of 5.0μm show elongated coffin-shape morphology along the *c*-axis, rendering large uniform surface coverage more difficult. It is worth mentioning that with large dissimilar intercrystal gaps it was very difficult to fill the gaps uniformly over large length scales, thus leaving areas with incompletely filled gaps after secondary growth.

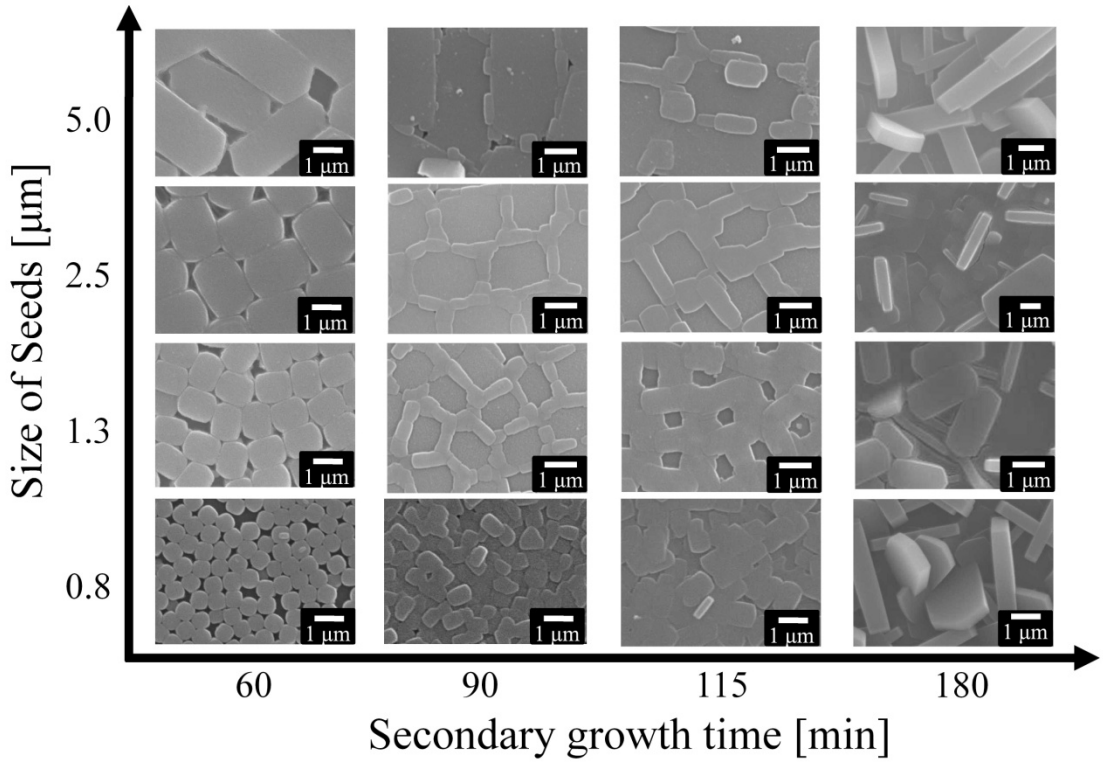

Figure 4.6 Effect of the size of MFI seed crystals on the preparation of continuous MFI silicalite-1 films during the secondary growth step at 175 ^{o}C for various growth times

Seeds consisting of both bigger and smaller crystals in size were manually assembled in order to reduce the growth time necessary to eliminate the intercrystal gaps as shown in Figure 4.7. Two seed layers made of 5μm/0.8μm and 2.5μm/0.8μm seed crystals were prepared by first assembling seed layers with bigger crystals followed by pushing smaller crystals onto the bigger crystal layers on substrates. As shown in the figure, the gaps between the seed crystals were greatly reduced due to the insertion of the smaller crystals. However, the smaller crystals in the gaps are randomly oriented, thus compromising overall preferred orientation. Subsequent secondary growth enabled the well inter-growth of the bigger and smaller seeds in the plane within 1.5h, resulting in *b*-oriented MFI zeolite films with randomly oriented grain boundaries. To the best of our knowledge, this type of MFI film (i.e., with single crystal domains preferentially oriented along the *b*-axis and grain boundaries randomly oriented) has never been reported. Comparison of the performance of these membranes with that of *b*-oriented membranes would enable us to determine the relative importance of single domain orientation and the grain boundary effect on the unprecedented enhancement of the performance of *b*-oriented MFI membranes.

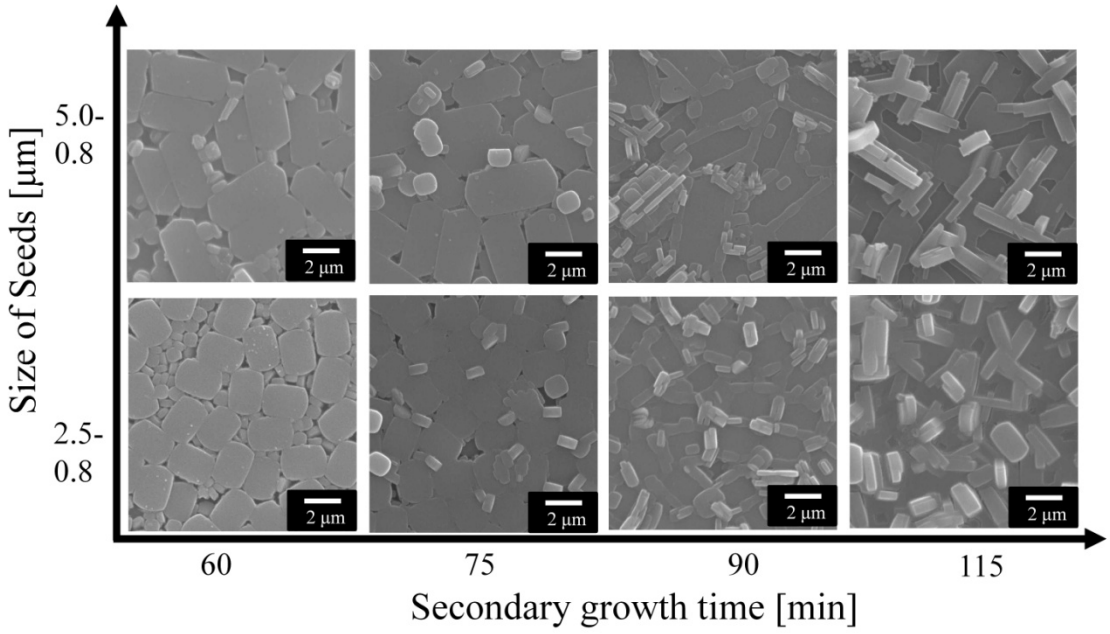

Figure 4.7 Secondary growth of MFI seed layers consisting of bigger and smaller seed crystals at 175 ^{o}C for various growth times. The bigger seeds were manually assembed into *b*-oriented seed layers and the smaller seeds were then manually pushed into the gaps between seed crystals

4.4 Conclusion

In summary, we have developed a simple method based on a secondary growth technique, which we call the micro-tiles-and-mortar method, to rapidly fabricate highly oriented zeolite thin films. The method enabled us to fabricate *b*-oriented MFI silicalite-1 thin films within several hours including the template removal process. The key step in our method is to passivate the flat facets of the seed crystals of the oriented seed layer, thus preventing the nucleation and growth of the crystals from the flat surface of the zeolite seed crystals while allowing the seed crystals to nucleate and grow in the plane. Our method requires neither complicated steps nor custom-made organic templates. The thickness of the zeolite films is essentially determined by that of the seed crystals which are less than 1 μm. Also for the first time, MFI films with single crystal domains preferentially oriented along the b-axis and grain boundaries randomly oriented were prepared from seed layers made of crystals of two different sizes. Our method is expected to offer new opportunities for the practical application of zeolite thin films and membranes.

CHAPTER V

OPTIMIZATION OF THE MICRO-TILES-AND-MORTAR METHOD

5.1 Introduction

In Chapter IV, we demonstrated the novel synthesis method for the *b*-oriented silicalite-1 MFI films with controlled microstructure on the silicon wafers. The *b*-oriented silicalite-1 films were synthesized by modified secondary growth. Our method suggested the easy ways to control membrane microstructure, such as thickness, orientation, and grain boundaries, which may influence their performance.

For the gas separation, the silicalite-1 films need to be prepared on the porous supports if they are supported zeolite membranes. Various types of supports have been used for the supported zeolite membranes. In particular, α-Al_2O_3 is by far the most largely used although other inorganic ceramic materials such as γ-Al_2O_3,[119, 120] TiO_2,[121] and ZrO_2,[122] as well as stainless steel [123, 124] have been reported.

The physical and chemical properties of porous supports considerably influence the zeolite membrane characteristics. For instance, cracks or defects formed in the zeolite membranes result in the difference in thermal expansion coefficients between the zeolite layer and porous support. Thus properties of porous supports should be considered when they are chosen. Among many physical and chemical properties, it is important to control the roughness of porous supports for the high quality of zeolite membranes with controlled microstructure. It is desirable to deposit seed crystals onto porous substrates with smooth surface like silicon wafers. The simple way to make a smooth surface of α-

Al_2O_3 is to polish it mechanically. Although the polishing is quite simple, it has a limitation to apply for the tubular supports. An alternative method for making smooth surface on the porous supports is to introduce an intermediate layer, which plays important roles 1) to create a smooth surface, 2) to prevent the zeolite layer from penetrating the support, or 3) to limit support leaching.[125] Inorganic SiO_2, γ-Al_2O_3, or ZrO_2 are widely used as an intermediate layer. Also, polymer films such as PVA, chitosan, and PEO are used in an intermediated layer on the porous α-Al_2O_3 for the *b*-oriented MFI membranes.[126]

In this dissertation, α-Al_2O_3 discs are used for the porous supports for the synthesis of the silicalite-1 membranes. It was shown that the orientation of silicalite-1 films was determined by the orientation of the seed layer. To prepare *b*-oriented silicalite-1 MFI membrane by our method, *b*-oriented seed layer first should be formed on the porous α-Al_2O_3 discs by manual assembly. In order to make *b*-oriented seed layer, α-Al_2O_3 discs must provide smooth surface. In this chapter, the proper intermediate layer is selected and optimized conditions are determined to make a smooth surface on α-Al_2O_3 discs. Microstructure of the silicalite-1 membranes are also controlled on the α-Al_2O_3 discs. The silicalite-1 membranes fabricated by optimized conditions are tested using single and binary gas separation.

5.2 Experimental

b-oriented silicalite-1 MFI membranes on the porous alumina supports were synthesized by our novel micro-tiles-and-mortar method. The preparation methods of the

porous alumina discs, seed crystals, seeding, passivation of faces of the seed crystal layer, and secondary growth are described in subsection 3.3 in detail.

Permeation measurement for single and binary gases is described in subsection 3.5. For the single gas permeance, H_2, He, CO_2, CH_4, and N_2 were measured in two different membranes; one with the activated grain boundaries, and the other with non-activated grain boundaries.

The surface morphology and cross sectional view of silicalite-1 membranes were characterized by Scanning Electron Microscopy (SEM) and the orientation of silicalite-1 film was confirmed by XRD. A detailed explanation about characterization of MFI silicalite-1 membranes was included in subsection 3.6.

5.3 Results and discussion

Figure 5.1 shows the schematic procedure for the synthesis of the silicalite-1 membranes on the porous α-Al_2O_3 discs. The orientation of the zeolite membranes is determined by the orientation of the zeolite seed layer. In order to make *b*-oriented silicalite-1 membranes, it is necessary to form the *b*-oriented seed monolayer. Although the porous α-Al_2O_3 supports are polished before the seed crystals are deposited on the supports, they still have a rough surface that may affect to lose the orientation of the seed layer. We tested two intermediated layers for providing a smooth surface on the porous α-Al_2O_3 discs; one is a **γ-**alumina inorganic layer and the other is a PVA polymer layer. The optimized condition will be discussed in the following sections (5.3.1 and 5.3.2).

To enhance bonding strength between seed crystals and the porous supports, polyamines are coated on the intermediate layer providing the hydrogen bonding between amine (NH_2) groups and hydroxyl (OH) groups. In this research, TMS-PEI was used for the polyamine linkers that consist of both polyethyleneimine (PEI) main chains and tetramethoxysilane (TMS) side chains. Compared to other PEI polymers, TMS-PEIs make strong bonding because they have two reactive sites; one is an imine in PEI main chain, and the other is a methoxysiliane in TMS that reacts with hydroxyl groups either on the PVA intermediate layer or on the surface of seed crystals. The spin coating for TMS-PEI on the α-Al_2O_3 discs was carried out in the clean environment to minimize defects generated by particle contamination.

To achieve the *b*-oriented seed crystal layer, the seed crystals are then manually assembled onto porous supports by simply rubbing the crystals following the procedure developed by Yoon and his coworkers.[79] This step typically took a couple of minutes depending on the size of the porous supports. A silicalite-1 seed layer is then calcined at 475^{o}C for 8h to remove not only the organic templates, tetrapropylammonium (TPA) occupied in the zeolite pore channels, but also the polymer layers such as PVA and TMS-PEI under the silicalite-1 seed layer. During the calcination process, silicalite-1 seed crystals make strong covalent bonding with hydroxyl group on α-Al_2O_3 discs by the dehydration reaction. It is worth mentioning here that since the highly packed seed crystals with about 95% of surface coverage were calcined before being grown into continuous films. The final calcination process of zeolite membranes may not be necessary if one is willing to sacrifice a small reduction (about 5%) in total mass flow.

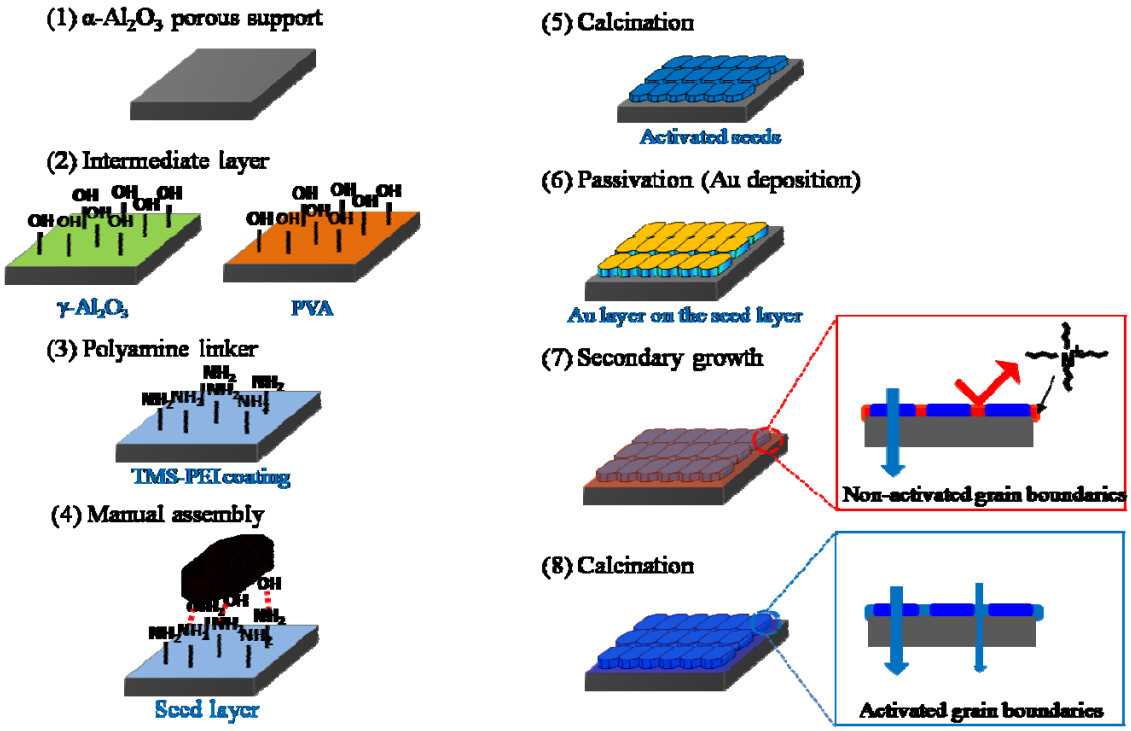

Figure 5.1 Schematic procedure for the *b*-oriented silicalite-1 membranes; (1) preparation of the porous α-Al_2O_3 supports, (2) spin coating of the intermediate layer either γ- Al_2O_3 or PVA, (3) TMS-PEI linkers to enhance bonding strength between seed crystals and surface of supports, (4) manual assembly of silicalite-1 seed crystals onto the α-Al_2O_3 tethered with PEI linkers, (5) calcination to activate pores in the zeolite seed layer and to remove polymer layers, (6) passivation of the faces of the zeolite seed layer to prevent the growth out-of-plane direction, (7) secondary growth to make continuous silicalite-1 membranes with non-activated grain boundaries, and (8) optional calcination to active pores in grain boundaries

This avoidance of the calcination of continuous zeolite films at high temperatures may have significant practical implications since typically the calcination step is time-consuming and oftentimes leads to crack formation in zeolite membranes even with very careful temperature programming.[40, 116, 117]

Thin Au/Pd layers are sputtered onto the MFI silicalite-1 monolayer to prevent the seed crystals from growing along the out-of-plane direction (i.e., along the *b*-axis). The *b*-oriented MFI silicalite-1 monolayer is finally hydrothermally grown to fill the gaps between the crystals by secondary growth. It is also of great interest to study the effect of the grain boundaries on the performance of zeolite membranes. If the membranes are not calcined after secondary growth, the diffusion of gas molecules will be only intracrystalline diffusion through zeolitic pores. However, if the membranes are calcined after secondary growth, there exist two different pathways; intracrystalline diffusion through zeolitic pores and intercrystalline diffusion through grain boundaries.

5.3.1 Optimization of γ-alumina layer on α-Al_2O_3

Among the different transition aluminas, γ-aluminas (γ-Al_2O_3) have attracted many interests due to their applications such as catalysts, membranes, and sensors.[127] The mesoporous γ-alumina layer is usually prepared by the sol-gel coating method. We prepare the γ-alumina films as an intermediate layer providing a smooth surface on the porous α-Al_2O_3 substrates. Although the sol-gel coating procedure for the γ-alumina layer has been well developed, the conditions such as molar composition of boehmite sol, PVA binder concentration, and drying rate of the solvents in the films are varied depending on the properties of porous supports such as porosity and pore diameter.

Thus, it is needed to optimize the coating parameters for a continuous γ-alumina layer on the porous α-Al_2O_3.

5.3.1.1 The molar composition of boehmite sol

The boehmite sol is made from an aluminium butoxide that reacts with excess water at 90^{o}C. After reaction with water, the aluminum butoxides became aluminum hydroxides. By peptization reaction with HNO_3, the aluminum hydroxide ($Al(OH)_3$) became $Al(OH)_3^+$ because $Al(OH)_3$ is generally a positive ion acceptor. These positive charge ions are able to repel each other; as a result, particles of alumina are reduced to a very small size of a few nanometers.

Two boehmite sols with different molar compositions (1ALTSB: 100H_2O, and 1ALTSB: 50H_2O) were prepared here. For a dilute boehmite sol (1ALTSB: 100H_2O), γ-alumina layer was not continuous as shown in Figure 5.2 (a). Since the dilute boehmite sol has a low density of colloidal aluminum nanoparticles in the sol as well as the low viscosity, boehmite sol may penetrate into the pores of α-Al_2O_3 supports forming island feature. However, higher molar composition of 1ALTSB: 50H_2O shows a continuous γ-alumina layer with leaf-shape patterns on the surface as shown in Figure 5.2 (b). We speculate that the leaf-shape patterns can be formed by PVA binders in the boehmite sol. It is concluded that the molar composition of 1ALTSB: 50H_2O make continuous γ-alumina layers, but the concentration of PVA binders needs further study to get a smooth surface.

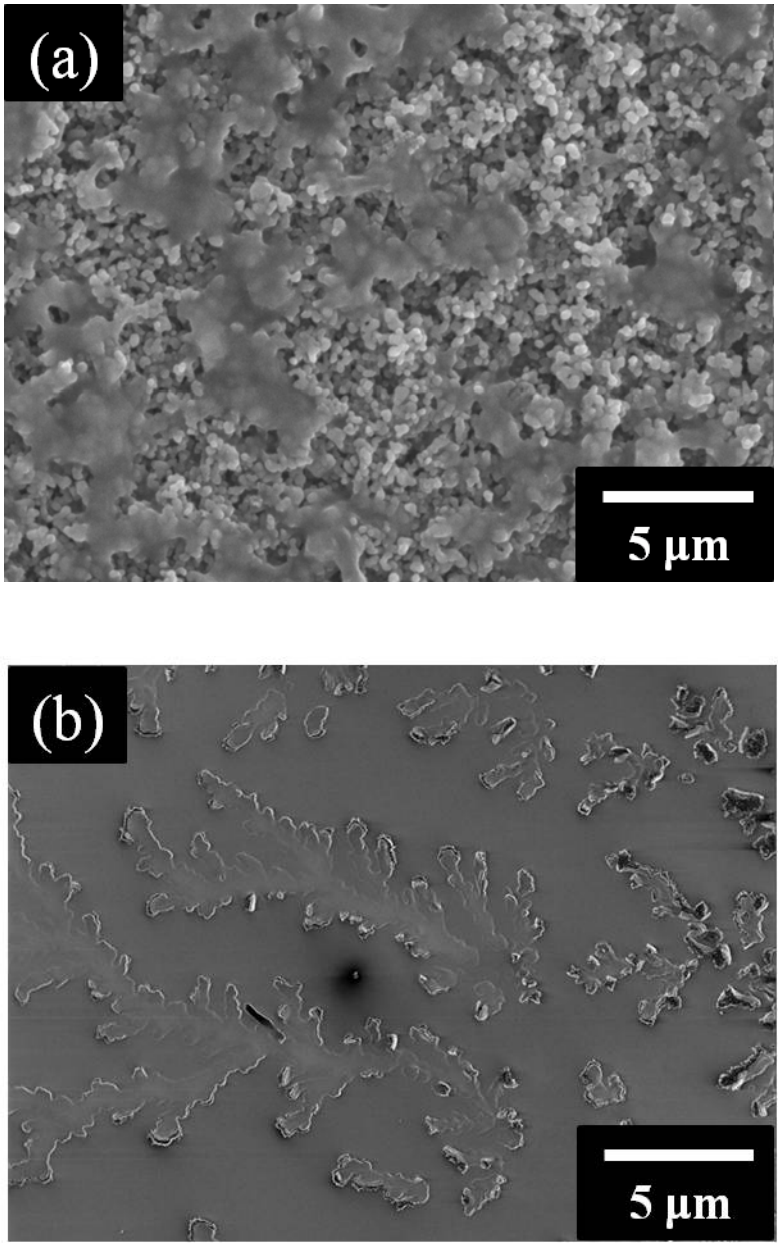

Figure 5.2 SEM images of the γ-Al_2O_3 layer formed by two different molar compositions of the boehmite sol: (a) 1ALTSB: 100H_2O, (b) 1ALTSB: 50H_2O

5.3.1.2 The concentration of the PVA binder

Boehmite sol is composed of aluminum hydroxide and PVA polymer. PVA polymers play two important roles in the boehmite sol. First, PVA serves as the binder that makes a strong γ-alumina layer resulting in crack- or defect-free films. Second, PVA polymers provide the mesopore structure in the γ-alumina layer after calcination. In this dissertation, the concentration of PVA is optimized for the formation of continuous γ-alumina layer.

Two concentrations of PVA (3% and 5%, wt %) were studied to make defect-free γ-alumina layer. Figure 5.3 shows the top view of SEM of the γ-alumina layer in terms of the PVA concentration. The lower concentration of the PVA (3%, Figure 5.3 (a)) shows the hole defects on the surface. However, the higher concentration of the PVA (5%, Figure 5.3 (b)) shows a very smooth surface without any hole defects. A high concentration of PVA helps colloidal alumina nanoparticles making dense network particulates in the Boehmite sol so that continuous γ-alumina layer was formed. Therefore 5% (wt %) of the PVA in boehmite sol was used for the formation of a continuous γ-alumina layer.

5.3.1.3 Drying method

In the thin film fabrication by the sol-gel method, the control of drying is crucial for the crack-free continuous films. The drying-induced cracks are general phenomena like mud and clay produce fracture patterns in the dry season. Figure 5.4 (a) shows drying-induced cracks on the γ-alumina layer.

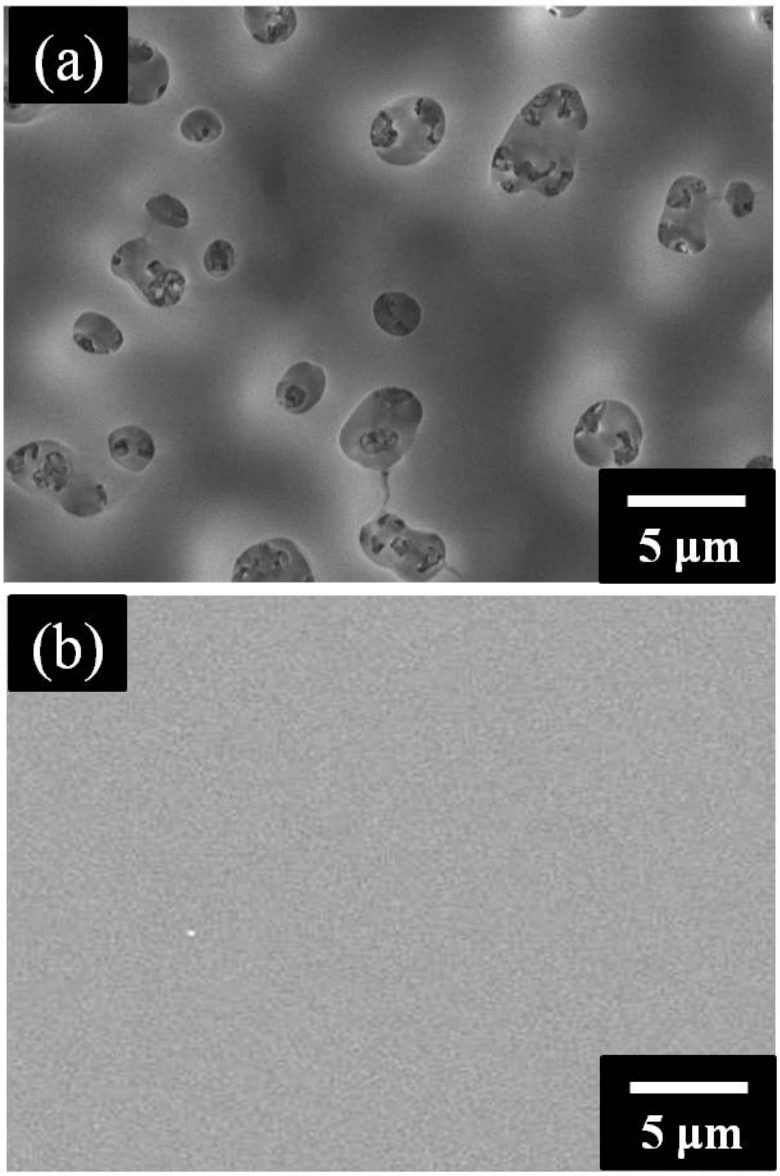

Figure 5.3 SEM top view of the γ-Al_2O_3 layer formed using two different PVA concentrations (weight percent %): (a) 3%, (b) 5%

In order to avoid cracks, understanding of the mechanism of the crack formation during the drying process is needed. When boehmite sol is coated on the rigid substrate, the solvents in the film start to evaporate and concentrate colloidal alumina nanoparticles into a close-packed array. When the rate of evaporation is less than the rate of liquid flow through the film, uniform shrinkage of the volume can occur. However, if the rate of evaporation is faster than the transport of the liquid to the film interface, a capillary pressure gradient exists. Constrained by the rigid substrate, the capillary pressure accumulates resulting in tensile stress at the surface, which causes the crack formation. According to the energy-balanced concept, cracks will occur as the film thickness exceeds a critical value. The critical film thickness can be expressed as: [128]

$$h_c = \frac{2G_c E}{Z\sigma^2(1-\nu)} \quad (1)$$

where h_c is the critical film thickness, G_c is the critical strain-energy release rate, E is the young modulus, ν is Poisson's ratio, σ is the tensile stress, and Z is a geometry parameter. In order to prevent cracks based on equation (1), films have to get low tensile stress (σ). As far as the experiment is concerned, the tensile stress can be controlled by changing drying rate of the solvent. The slower the drying rate of the solvent, the lower the tensile stress. In this study, we decrease the rate of solvent evaporation by controlling relative humidity of water during the drying process. In Figure 5.4 (b), the γ-alumina layer dried under 100% relative humidity at 40^{o}C and shows no crack formation.

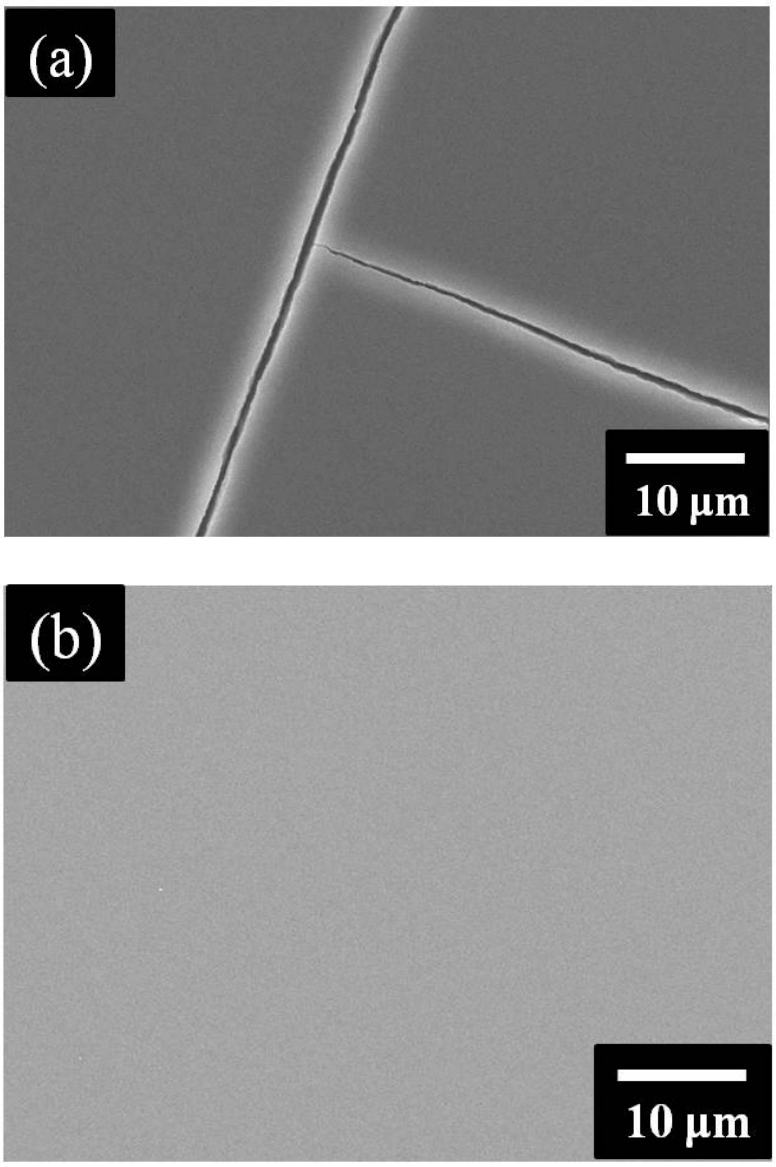

Figure 5.4 Control of the rate of solvent evaporation in the γ-Al_2O_3 layer by drying conditions: (a) drying under ambient environment, (b) 40^{o}C, 100% H_2O humidity

5.3.1.4 Fabrication of the silicalite-1 membranes on the porous α-Al_2O_3 supports with a γ-alumina intermediate layer

Silicalite-1 membranes were fabricated on the porous α-Al_2O_3 supports with a γ-alumina intermediate layer by the micro-tiles-and-mortar method. Figure 5.5 shows the SEM top view and cross sectional view of the silicalilte-1 membranes. Au passivation was deposited by sputtering with 20 nm in thickness, and secondary growth was carried out at 175^{o}C, for 3 h. From the SEM top view in Figure 5.5 (a), silicalite-1 membrane is dense. Intercrystal gaps were completely filled and *a*-oriented twin crystals appeared on the surface. Appearance of *a*-oriented twin crystals came from the newly overgrown layer, which is not passivated by Au. Although silicalite-1 membranes have *a*-oriented twin crystals on the surface, XRD showed that the dominant peaks are (020) and (040) as shown in Figure 5.5 (c). The orientation of seed layer is preserved by preventing the growth of seed layer along the out-of-plane direction and *b*-oriented silicalite-1 membranes are successfully obtained. The SEM cross sectional view shows the thickness of the membrane is about 1.1 μm in thickness and the intercrystal gaps are filled due to the growth of seed crystals along the in-plane direction during secondary growth. Thickness of membranes is similar to thickness of seed monolayer because seed layer prevents growing along the out-of-plane direction by Au passivation during secondary growth. It is concluded that b-oriented silicalite-1 membranes is fabricated on the porous α-Al_2O_3 support with a γ-alumina intermediate layer.

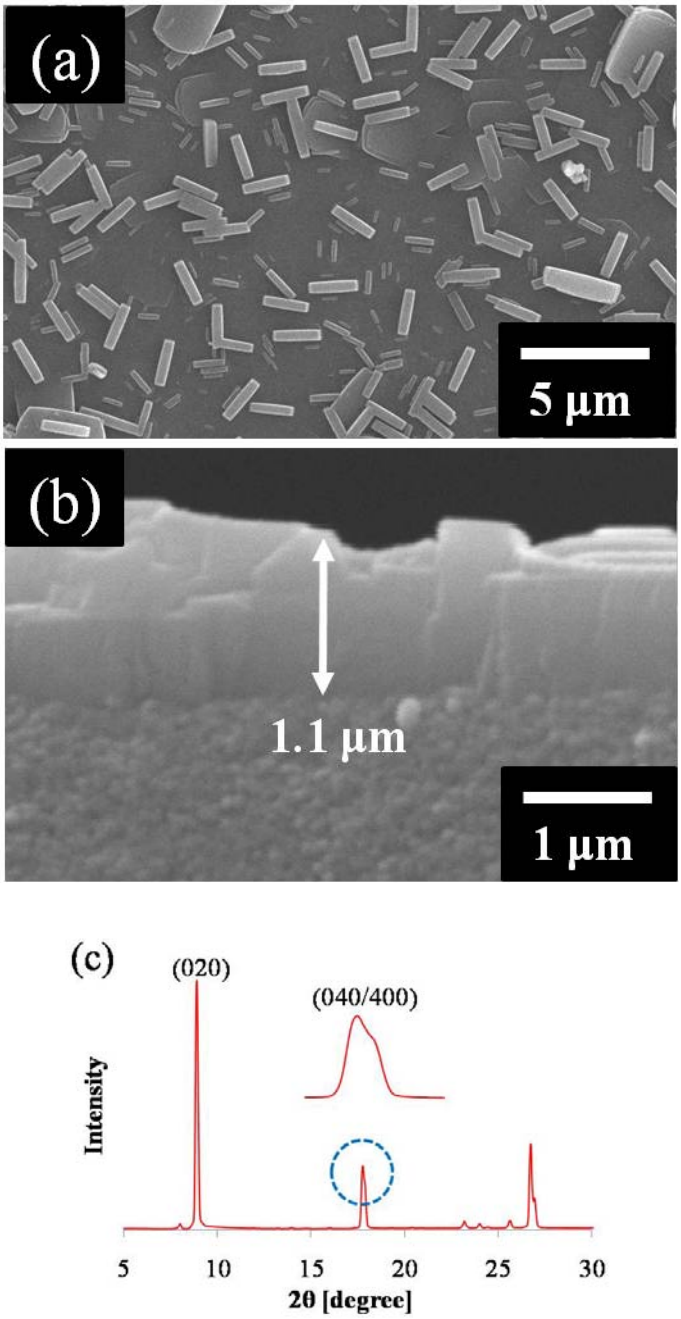

Figure 5.5 SEM images of the *b*-oriented silicalite-1 zeolite membranes on the γ-Al_2O_3 layer; (a) top view of the membranes, (b) cross sectional view of the membranes, and (c) XRD pattern

5.3.2 Optimization of the PVA layer on α-Al_2O_3

Hydrophilic PVA polymers are widely used as membrane materials due to their unique properties.[129] Compared to inorganic intermediate layers such as γ-Al_2O_3, TiO_2, and ZrO_2, PVA polymers are the cheapest and most cost-effective. Also, due to hydroxyl groups in the PVA structure, PVA polymers can be used coupling agents as linkers that provide a reaction of either covalent or ionic interaction. Recently, a zeolite seed monolayer was demonstrated on the α-Al_2O_3 substrates supported by a PVA thin film that was coated by the dip coating method.[126] Inspired by their work, in this section we try to find the conditions for the continuous PVA layer on the porous support.

Apart from the γ-Al_2O_3 layer discussed in the previous section, PVA films are tested as an intermediate layer. In this research, spin coating is used for the formation of the PVA films. Spin coating provides the way to control precisely the film thickness by changing the spin RPM and composition of coating solution. The optimized coating solution is determined to prepare a continuous PVA layer.

5.3.2.1 Molecular weight

According to an average molecular weight of PVA polymers, the properties of PVA coating solution can be changed. For example, the higher molecular weight of PVA made a viscous solution to affect the film formation because the coating solution is not uniformly spread very well on the substrate during spin coating. However, the lower molecular weight of PVA makes the coating solution with low viscosity giving a change to penetrate easily into pores in the α-Al_2O_3 substrates.

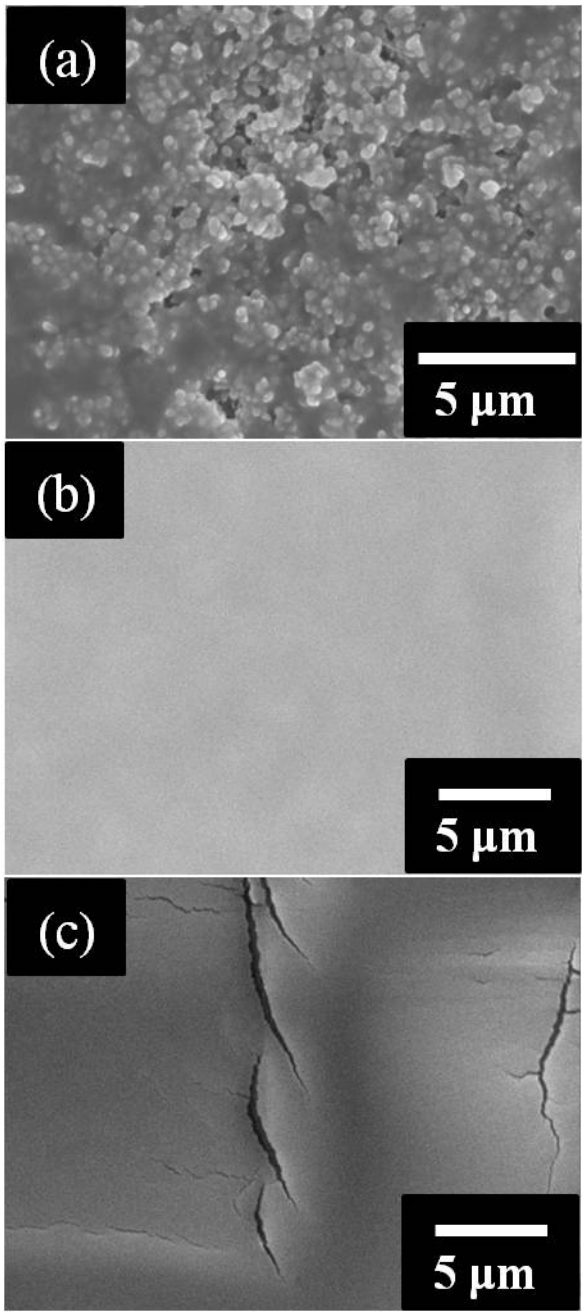

Figure 5.6 Typical SEM top views of the PVA layers formed by spin coating using different molecular weight of PVA. (a) Mw = 31,000 ~ 50,000; (b) Mw = 85,000 ~ 124,000; and (c) Mw = 146,000 ~ 186,000

In order to synthesize the continuous PVA layer, three PVA coating solutions with different average molecular weight ((1) Mw=31,000 ~ 50,000; (2) Mw=85,000 ~ 124,000;, and (3) Mw 146,000~ 186,000) were tested. The concentration of the PVA coating solution was 5% of weight percent. A typical SEM surface image of the PVA layer using lower molecular weight (Mw=31,000 ~ 50,000; Figure 5.6 (a)) showed a rough surface morphology. The coating solution with low molecular weight may penetrate into the pores of the porous substrate due to the low viscosity. A typical SEM surface image of the PVA layer using higher molecular weight (Mw=146.000 ~ 186,000) showed cracks as shown in Figure 5.6 (c). The PVA layer has cracks on the surface because the thickness of the PVA layer goes over critical thickness of crack formation during the drying process after spin coating. A typical SEM surface image of the PVA layer using medium molecular weight (Mw=85,000 ~ 124,000) showed a continuous crack-free PVA layer. It was determined that the average molecular weight Mw=85,000~124,000 of PVA for the coating solution is the best.

Silicalite-1 membranes were then fabricated on the α-Al_2O_3 substrates with the PVA polymer intermediate layer as shown in Figure 5.7. Au passivation was deposited by sputtering with 20 nm in thickness and secondary growth was carried out at 175^{o}C, for 3 h. The top view of the SEM image in Figure 5.7 (a) shows the continuous dense silicalite-1 membranes. From the cross sectional view of SEM images in Figure 5.7 (b), the thickness of silicalite-1 membranes was about 1.3μm. Although *a*-oriented twin crystals are on the surface of silicalite-1 membranes, XRD confirms that silicalite-1 membranes are *b*-oriented membranes.

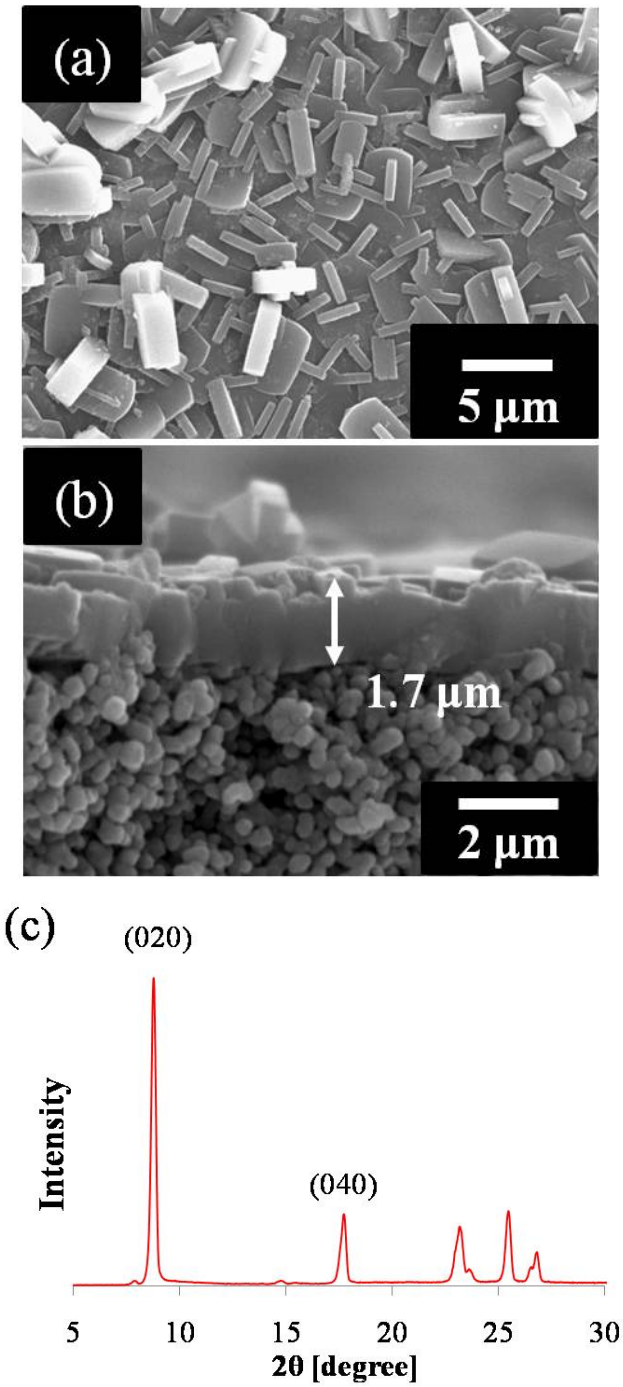

Figure 5.7 SEM images of the *b*-oriented silicalite-1 zeolite membranes on the PVA layer: (a) top view of the membranes, (b) cross sectional view of the membranes, and (c) XRD pattern

5.3.3 Removal of Au/Pd passivation layer

After secondary growth, Au passivation layer deposited on the surface of seed crystals have to be removed to open the entrance of diffusion pathway in zeolite membranes. Au/Pd metals are removed by wet etching in microfabrication. Wet etching solution is a mixture of 3HCl: $1HNO_3$: $2H_2O$. To confirm the removal of passivation layer after etching process, EDS element analysis was carried out. Figure 5.8 shows amount of elements on the silicalite-1 membranes before and after etching process. Before etching process, Au elements were detected. However, Au molecules were disappeared after etching for 5 min. It was concluded that Au passivation layer on the silicalite-1 membranes was completely removed by etching process after 5 min.

5.3.4 Membrane quality

The *b*-oriented silicalite-1 membranes were fabricated on the α-Al_2O_3 supports with either γ-alumina layer or PVA film, respectively. As discussed in the previous sections, after secondary growth the silicalite-1 membranes were overgrown over the seed layer. Thus, the membranes are needed to activate pores by calcination.

After calcination, membranes were inspected by SEM as shown in Figure 5.9. The silicalite-1 membranes on the γ-alumina layer showed the cracks due to the thermal stress during calcination. The silicalite-1 MFI crystals contract due to removal of TPA^+ during calcination, while the γ-alumina layer expands. For that reason, a thermal stress develops in the membranes, which leads to formation of cracks or defects. However, cracks were not observed on the membranes fabricated on the α-Al_2O_3 substrates intermediated by the PVA polymer layer.

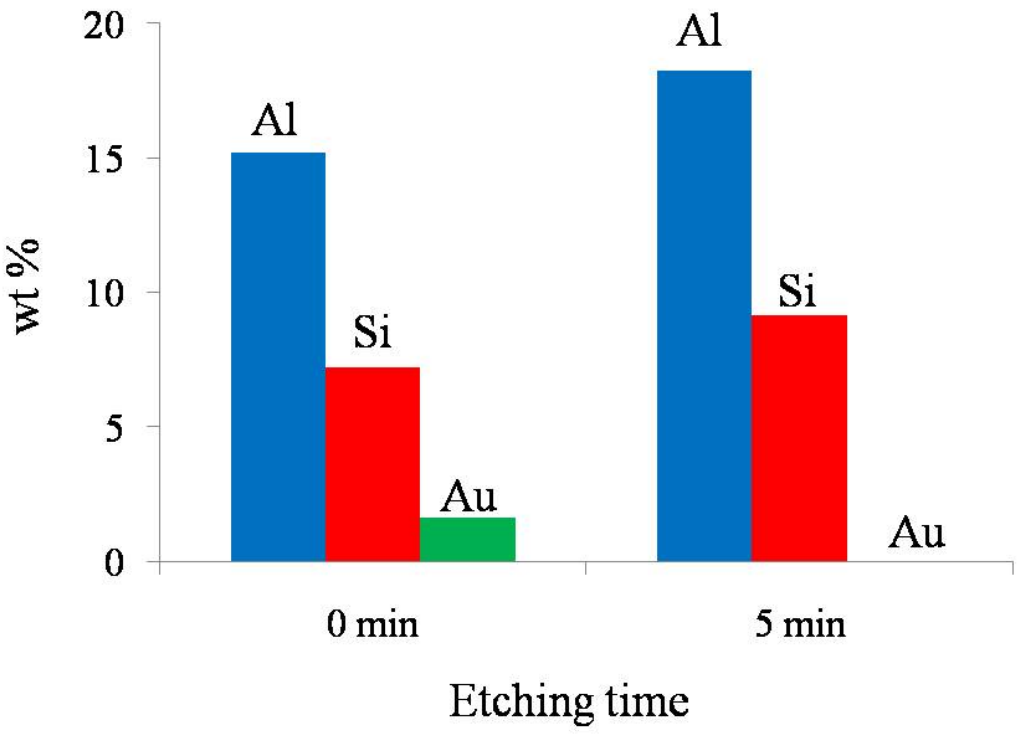

Figure 5.8 Metal elements analysis on the silicalite-1 membranes by EDS. Two samples were prepared. One is as-synthesized MFI membranes before etching (0 min), the other is etched for 5 min

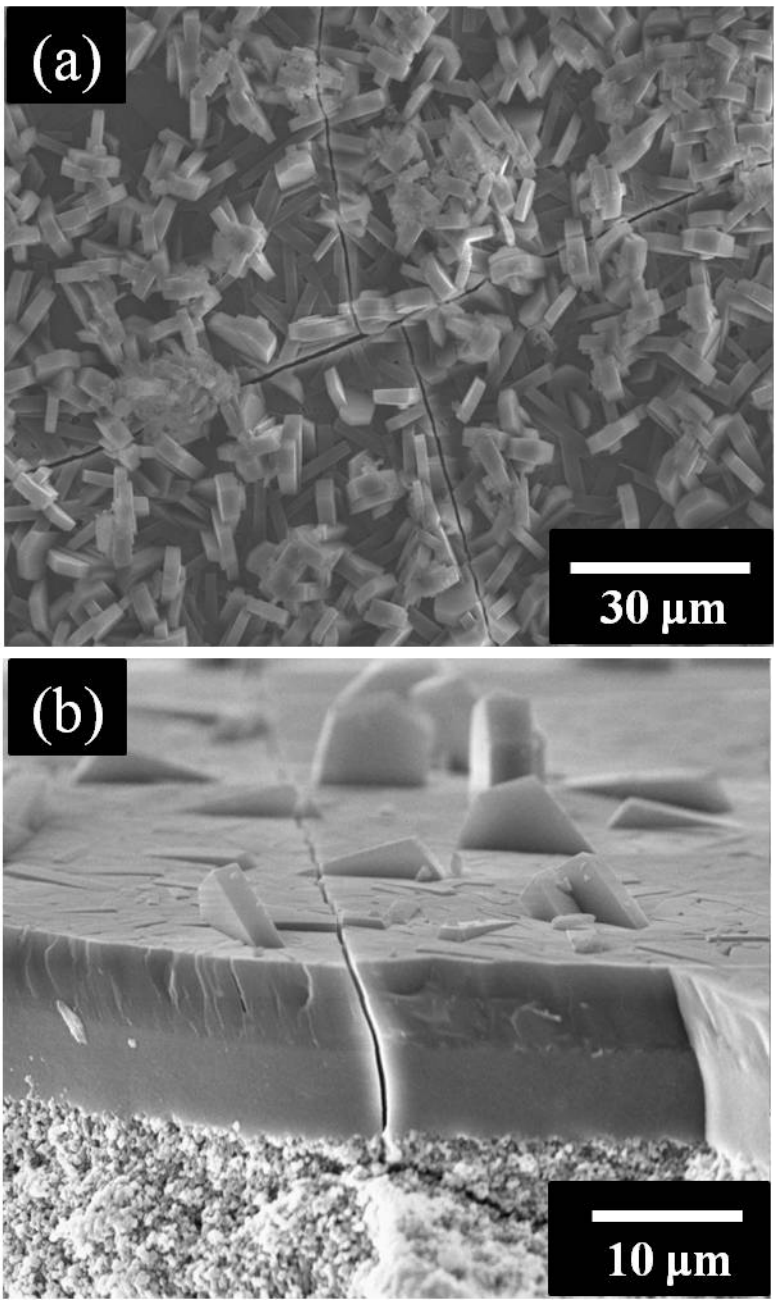

Figure 5.9 The formation of cracks on the silicalite-1 membranes intermediated the γ-alumina layer after calcination: (a) top view, and (b) cross sectional view

Since the PVA polymer layer was removed during the calcination for silicalite-1 seed layer, silicalite-1 membranes were directly bound to the α-Al_2O_3 after secondary growth. However, due to a rough surface of α-Al_2O_3, silicalite-1 membranes had a weak bonding with α-Al_2O_3 support, which causes to produce lower thermal stress in the membranes. Silicalite-1 membranes formed on the PVA layer are likely to be crack-free membranes. Figure 5.10 shows a large area of silicalite-1 membranes taken by SEM. This membrane was fabricated on the PVA layer using our micro-tiles-mortar method.

5.3.5 Single gas permeation results

Single gas permeation results are shown in Figure 5.11. The permeance was measured by the time-lag method described in subsection 3.5. H_2, CO_2, N_2, and CH_4 were used for the single components whose molecular size is smaller than pore size in the zeolite membranes. Two different types of silicalite-1 membranes were measured. One was the silicalite-1 membranes with activated grain boundaries where TPA molecules were completely removed; in other words, after secondary growth the TPA molecules from the newly grown MFI were calcined. The other was the silicalite-1 membranes with non-activated grain boundaries where the TPA molecules from the newly grown after secondary growth were not removed. The permeance of the membranes with non-activated grain boundaries was about 20% lower than that with activated grain boundaries. The difference of permeance of two samples caused from two reasons: 1) enhancing intercrystalline diffusion through the defects in the grain boundaries, 2) increasing diffusion through cracks on the membranes.

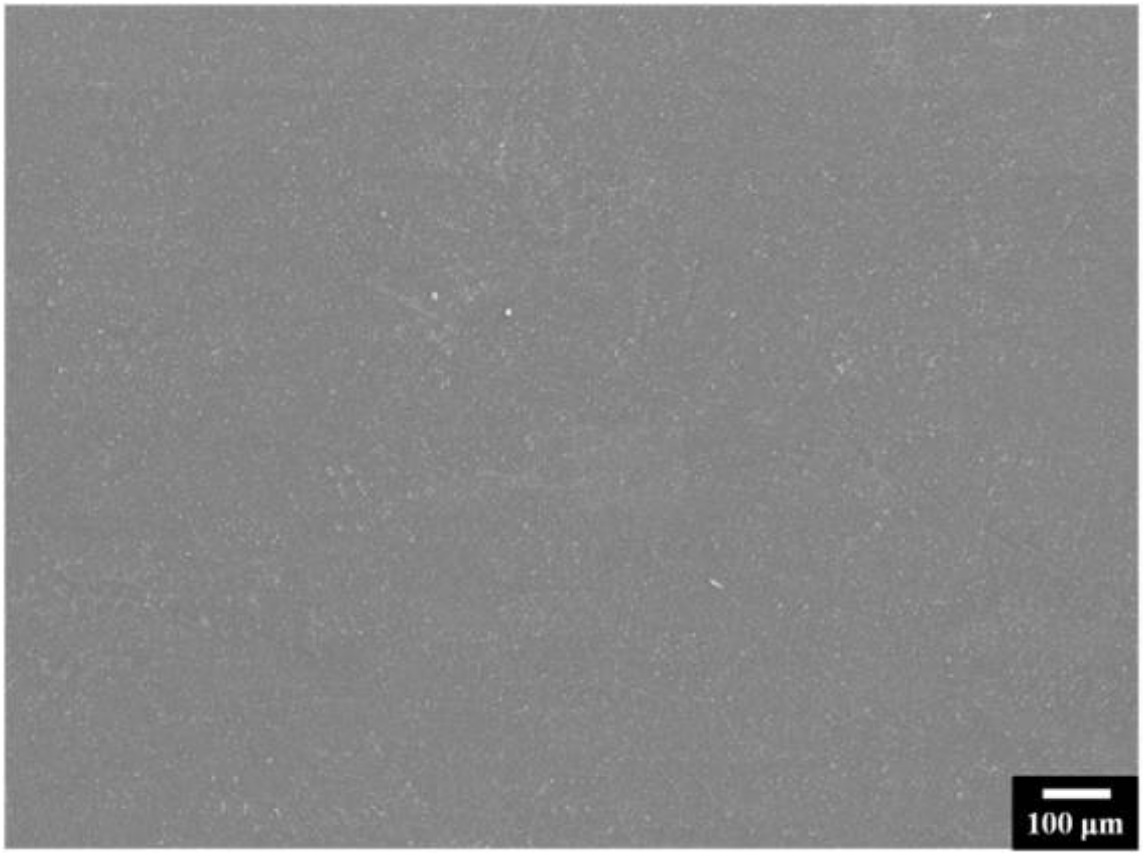

Figure 5.10 SEM image taken from a large area of silicalite-1 membranes formed on a PVA polymer layer

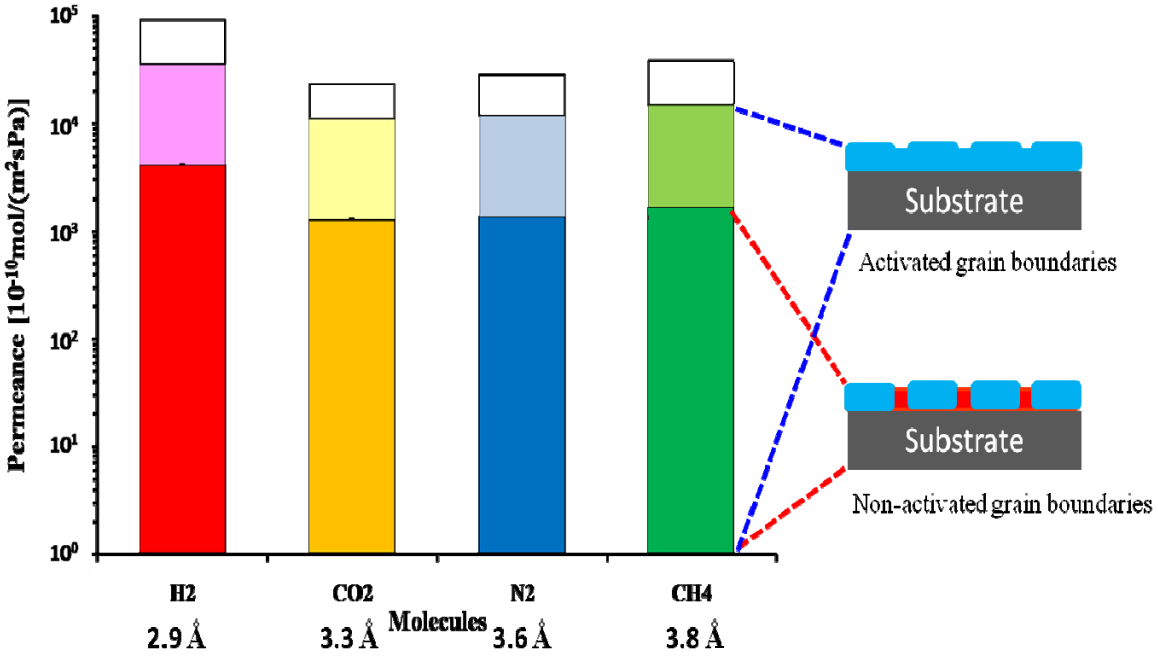

Figure 5.11. Single gas permeance through two different types of silicalite-1 membranes. Bright colors represent the permeance of the membranes with activated grain boundaries; in other words, TPA molecules newly grown after secondary growth were calcined. Dark colors show the permeance of the membranes with non-activated grain boundaries where TPA molecules were not removed. Blank areas represent the permeance through bare α-Al_2O_3

During the calcination of the silicalite-1 membranes, defects and cracks might form in the grain boundaries. We will discuss more about the formation of defects and cracks in next chapter. We concluded that the effective membrane surface area is about 80% of the total membrane area, which is reasonably consistent with the degree of surface coverage by the seed crystals.

5.4 Conclusion

We demonstrated the *b*-oriented silicalite-1 membranes on the porous α-Al_2O_3 supports by the micro-tiles-and-mortar method. As the intermediate layer is used to provide a smooth surface, both γ-alumina and PVA polymer, respectively, were tested to coat on the porous supports. The silicalite-1 membranes were fabricated successfully on both intermediated layers. However, the silicalite-1 membrane on the γ-alumina showed the formation of cracks due to thermal stress during calcinations. It was determined that the PVA polymer used as an intermediate layer on the α-Al_2O_3 provided a smooth surface. After seeding of silicalite-1 crystals on the PVA layer by manual assembly, the calcination was carried out not only for activation of pores in MFI seed crystals, but for PVA intermediate layer removal. The quality of silicalite-1 membranes was measured by a large area of SEM and by single gas permeance. The large area of SEM confirmed that there were no big cracks on the membranes. For the single gas permeance, two types of membranes were tested. It was concluded that the effective area of membranes with non-activated grain boundaries was 80%, which is consistent with the degree of surface coverage by the seed crystals.

CHAPTER VI

PERMEATION OF XYLENE ISOMERS THROUGH B-ORIENTED SILICALITE-1 MEMBRANES

6.1 Introduction

Industrial interest in cost effective way to separate hydrocarbon isomers has been increasing. In particular, separation of *p*-xylene molecules (kinetic diameter = 5.8 Å) from *o*-xylene molecules (kinetic diameter = 6.8 Å) is very important in the petroleum industry because *p*-xylene is a starting material to produce monomers for the production of PET plastics and polyester clothing. Due to the close boiling point of xylene isomers (411K ~ 417K), distillation is not practical. Instead, adsorption based separation for xylene isomers have been accomplished in batch reactor. However, this technique is very energy and cost intensive because of the batch process. Thus, energy and cost effective separation method are demanding.

Zeolite membranes with good thermal, chemical stability and well defined pores of molecular dimensions has suggested new opportunities for the separation of hydrocarbon isomers in low energy and cost demand operation. The MFI zeolite membranes have been used to successfully separate *p*-xylene from *o*-/or *m*-xylene by means of molecular sieving (~ 5.5 Å).[6, 39, 72, 99, 102, 105, 114, 130-135] For instance, Keizer et al.[133] reported separation factor was about 60 at 400 K. Xomeritakis et al.[102] showed the separation factor was 3.8 at 373K. Lai et al.[39] experimentally showed that the selectivity of *p*-xylene over *o*-xylene was unprecedented (speration factor was above 400).

From the separation data reported from many researchers, it may be doubt that the separation factors through MFI zeolite membranes for xylene isomers were not consistent. There are a few reasons for the inconsistent separation performance of MFI zeolite membranes. First, the orientation of MFI membranes highly affects the separation performance. For instance, *b*-oriented MFI membranes dramatically increased separation performance for xylene isomers compared to other oriented membranes because channels are straight along the *b*-axis, thus effectively enhancing selective intracrystalline diffusion of molecules. Second, defects and cracks formed during calcination of template removal cause the low spearation performance. Most MFI zeolite membranes have been fabricated on the porous supports such as inorganic alumina and stainless steel. Due to the thermal expansion mismatch between MFI zeolite layer and porous supports, detects and cracks are formed during calcination.

In Chapter V, we showed the simple preparation of the *b*-oriented MFI membranes by the micro-tiles-mortar-method. This method suggested simple way to control the orientation of membranes by preparing oriented zeolite seed layer. Also, this method provided the MFI zeolite membranes with controlled grain boundaries. The density of grain boundaries was controlled by changing size of seed crystals, and the structure of grain boundaries was changed by using two different sizes of seed crystals. It was also controlled the pore structures in the grain boundaries by the final calcination process. Since the highly packed seed crystals with about 95 % of surface coverage were calcined before being grown into continuous films, the final calcination process of zeolite

membranes may not be necessary if one is willing to sacrifice a small reduction (about 5 %) in total mass flow.

In this Chapter, we demonstrate separation performance of *b*-oriented silcalite-1 membranes fabricated by our method. The permeance and separation factor of xylene isomers have been measured by the Wicke-Kallenbach (WK) method. The separation performance of our *b*-oriented membranes is compared to reference data. The effect of the density and structure of grain boundaries on the xylene separation is discussed experimentally for the first time.

6.2 Experimental

6.2.1 Synthesis of *b*-oriented silicalite-1 membranes with controlled grain boundaries

Thin *b*-oriented silicalite-1 membranes were synthesized by our method described in subsection 3.3. The structure of grain boundaries was controlled by using two different sizes of seed crystals; bigger size of crystals (~ 1.3 μm) as tiles and smaller size of crystals (~150 nm) as mortar. First, bigger seed crystals were deposited on the porous support by rubbing method and then smaller seeds were pushing to fill the gaps between bigger seeds. Calcination of seed layer and secondary growth were carried out to make continuous membranes described in Chapter 3.3. After secondary growth, two different silicalite-1 membranes were prepared to control the structure of grain boundaries. One membrane was not carried out calcination after secondary growth, which had non-activated pores in grain boundaries. The other was calcined to activate pores in grain

boundaries. Two membranes with controlled the structure of grain boundaries were measured permeance of xylene isomers.

The silicalite-1 membranes with controlled the density of grain boundaries were also prepared by changing size of seed crystals. Four different sizes of seeds (0.8 μm, 1.3 μm, 2.5 μm and 8.0 μm) were deposited on the supports and continuous membranes were fabricated by secondary growth. The silicalite-1 membranes with controlled the density of grain boundaries were tested by measuring permeance of xylene isomers.

6.2.2 Permeation of xylene isomers

Xylene isomers (*p*- and *o*-xylene) were used to evaluate the performance of our MFI silicalite-1 membranes. The measurement and calculation of permeance and separation factor were described in subsection 3.5 in detail.

6.3 Results and discussion

6.3.1 Xylene permeation results

Figure 6.1 shows representative binary permeation behavior of xylene isomers through *b*-oriented silicalite-1 membranes synthesized by our novel method. The silicalite-1 membrane was prepared by seeded secondary growth at 175^{o}C for 3h. The surface of seed layer was passivated by depositing Au/Pd of 20 nm thick. After secondary growth, the membrane was calcined to open the pores at 465^{o}C for 8 h with 0.5^{o}C/min ramp rate. The feed stream was generated by He gas bubbling in the xylene

solutions at 25°C. The partial pressure of the feed mixture consists of 0.45 kPa for *p*-xylene and 0.45 kPa for *o*-xylene.

In Figure 6.1 (a), the permeance of *p*-xylene is slightly decreasing with temperature and is close to upper limit. The permeance of *o*-xylene is continuously decreasing with temperature. The maximum separation factor is about 4 as shown in Figure 6.1 (b). These permeation behaviors are different from those of *b*-oriented MFI membranes reported by Lai et al.[6, 39] It was shown that the permeance of *p*-xylene had a weak maximum at 125°C and permeance of *o*-xylene was dramatically decreasing with temperature. The separation factor was about 450 at 220°C.

To check the consistency of permeance data, three identical membranes were prepared using the same experiment conditions. Table 6.1 shows the permeance and separation factors of three membrane samples at 125°C. Permeance of *p*-xylene on the three samples is reproducible. However, considerable variation is observed for *o*-xylene. Compared to the binary permeation from Lai et al., the permeation behavior is similar to those of their *b&a&h0h/c*-oriented or *b&a* oriented MFI membranes showing low separation factor.

To analyze the different permeation behaviors of xylene isomers through our *b*-oriented membranes, top view of SEM was taken in Figure 6.2. It was observed that cracks were formed on the membranes. Those cracks that provide the non-zeolitic diffusion pathway caused low separation factor. It is well known that a thermal expansion mismatch between bonded materials result in stress and consequently cracks.

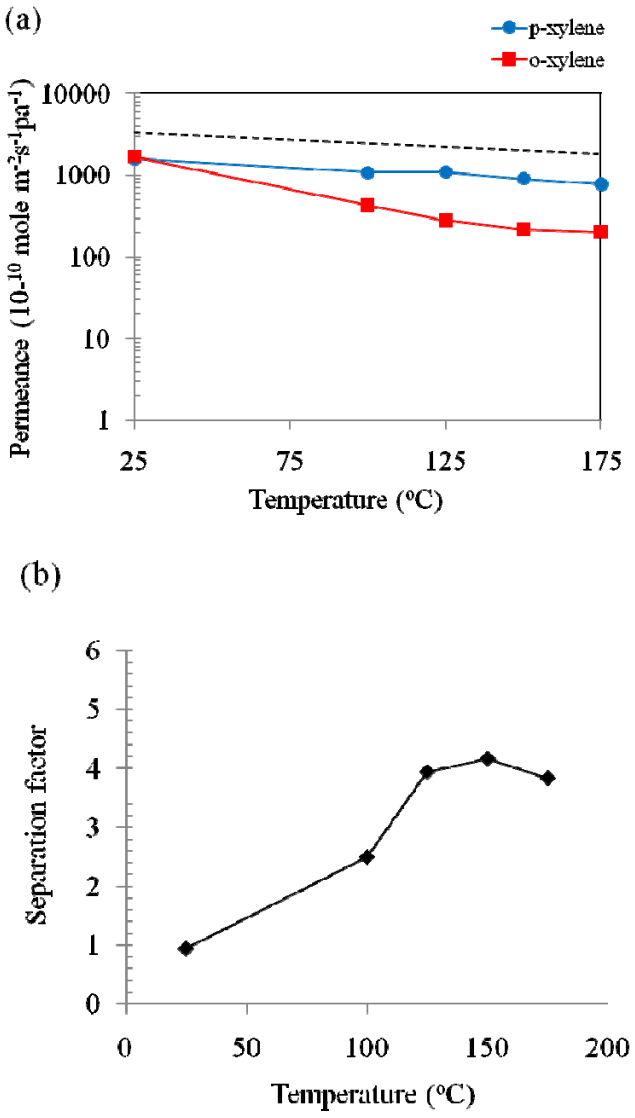

Figure 6.1 Binary permeation results of xylene isomers (a) *p*-xylene (circle symbols) and *o*-xylene (square symbols) permeance (b) separation factor. Feed partial pressure: *p*-xylene =0.45 kPa, *o*-xylene=0.45 kPa. Dashed line: permeance of *p*-xylene through the α-Al_2O_3 support

Table 6.1 Binary permeation results for three silicalite-1 MFI membrane samples prepared using the same synthesis conditions. Size of seed crystals is 1.3 μm, thickness of Au passivation layer is 20 nm, secondary growth is carried out at 175^{o}C for 3 h, and calcination at 465^{o}C for 8 h with 0.5^{o}C/min ramping rate

Sample	Permeance (10^{-10} mol $m^{-2}s^{-1}Pa^{-1}$)		Separation factor
	p-xylene	o-xylene	
1	1143. 5	469.5	2.5
2	1096.1	278.1	3.9
3	1281.5	719.1	1.8

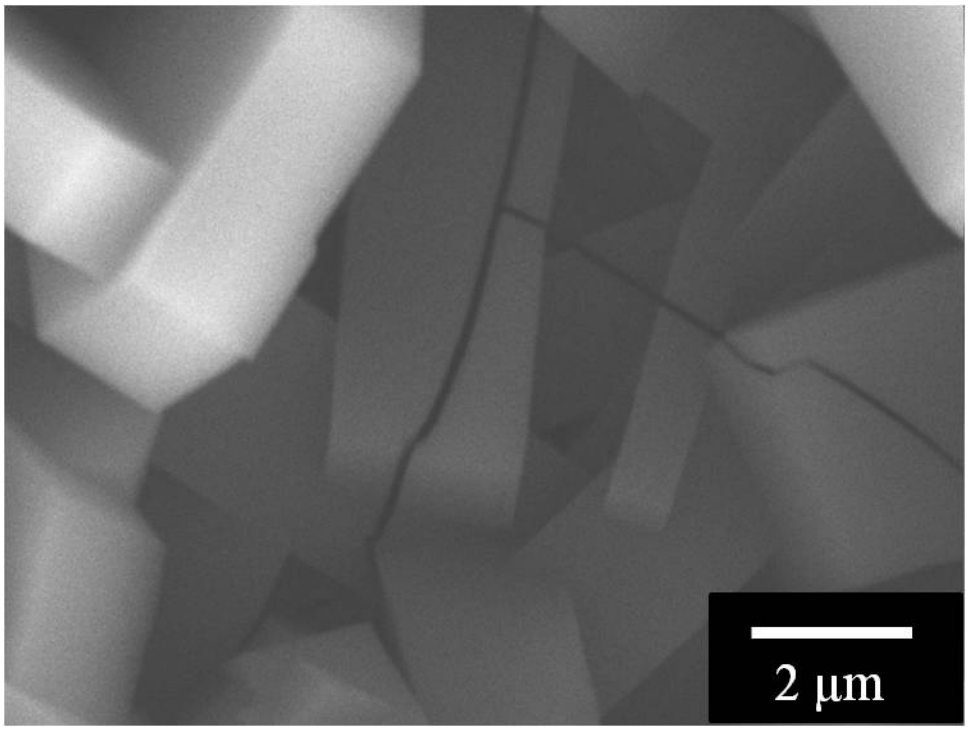

Figure 6.2 SEM image of cracks formed on the membranes after calcination

The MFI structure experiences a strong contraction during template removal while α-alumina porous supports expand during heating. Thus cracks were frequently formed in MFI membranes synthesized on α-alumina porous support during calcination.

6.3.2 Hypothesis for the low separation factor

For the application of gas separation, separation performance is highly influenced the microstructure of membranes. In particular, the orientation of membranes plays important role to separate xylene isomers through MFI membranes. For the first time, Lai ea al. demonstrated significant improvement on separation of xylene isomers through *b*-oriented MFI membranes. It has suggested that *b*-oriented MFI membranes have straight channels along the *b*-axis providing the fastest pathway. Also, the structure of grain boundaries made better contact between neighboring seed crystals in the b-oriented MFI membranes showing high crack resistance during calcination.

We also expected that *b*-oriented MFI membranes formed by our method would show similar permeation behaviors as Lai's membranes. However separation factor was only about 4 at most. It was observed that the cracks were formed on the membranes after calcination, which caused low separation performance. This observation of low separation is opposite to the argument that *b*-oriented MFI membranes have high crack resistance during calcination. Thus, we came up with the hypothesis about the crack formation in terms of membrane orientation and degree of intergrowth between seed crystals.

Recently, Gualtieri et al. reported the change of the strain along different crystallographic directions in the MFI films as a function of temperature by in situ high temperature synchrotron powder diffraction as shown in Figure 6.3.[136] According to their results, compressive stain was observed along the *a*- and the *c*-axis, but tensile strain along the *b*-axis. Inspired by their results, we hypothesize that the formation of cracks or defects would be highly depending on the orientation of membranes and degree of intergrowth of crystals during calcination as illustrated in Figure 6.4.

For the *b*-oriented MFI membranes in Figure 6.4 (a), compressive strain along the *a*- and the *c*-direction is observed. The *b*-oriented MFI membranes experienced tensile stress along the in-plane direction (i.e. along the *a*-/*c*-axis) because α-Al_2O_3 supports expand during calcination. If the seed crystals are highly intergrown after secondary growth, seeds and newly grown layer in the grain boundaries are equally strong, and thermal tensile stress is released to generate cracks on the membranes. In case of less intergrown seed layer, chances are likely to open the grain boundaries instead of formation of cracks during calcination. In case of *a*- or *c*-oriented MFI membranes in Figure 6.4 (b), they experienced compressive stress along the in-plane direction during calcination. The *a*- or the *c*-oriented MFI membranes could have more resistance of the formation of crack than *b*-oriented membranes during thermal treatment. With this hypothesis, we speculate that cracks or defects might be more easily formed on the *b*-oriented membranes than *a*- or *c*-oriented membranes.

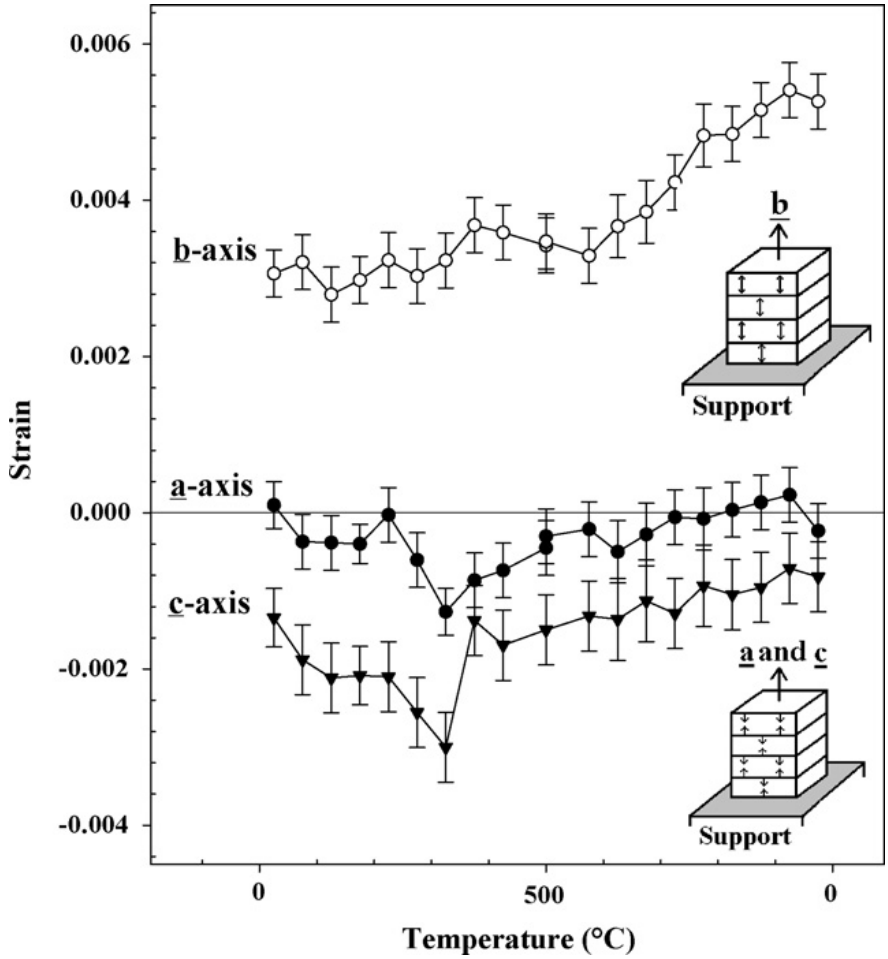

Figure 6.3 The strain along different crystallographic directions in the MFI film as a function of temperature. The direction of the strain is perpendicular to the film surface. The inserted sketches show that the crystallographic planes along *b* are under tensile strain while the ones along *a* and *c* are under compressive strain. Adapted from Gualtieri et al.[136]

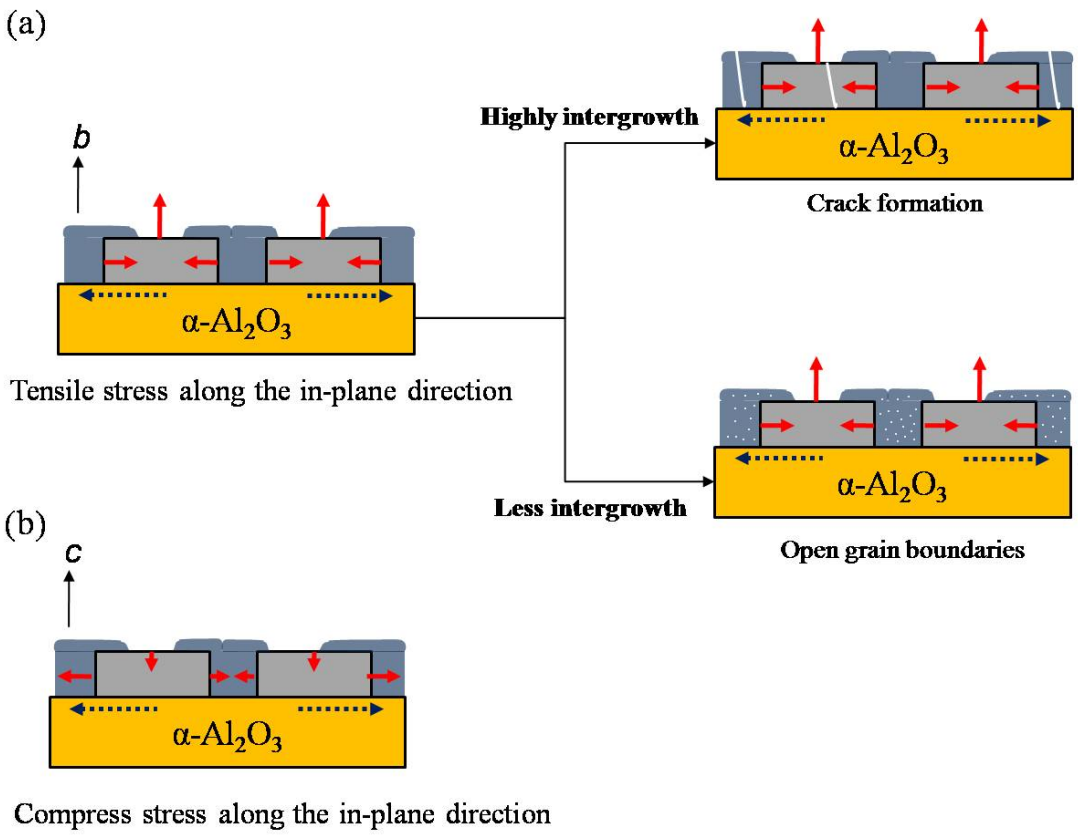

Figure 6.4 Hypothesis of the formation of cracks or defects according to the orientation of membranes and intergrowth of crystals. (a) The b-oriented membranes experience tensile stress in plane direction. If crystals are highly intergrown, cracks are developed. Fewer intergrown crystals result in the formation of open grain boundaries during calcination (b) while *a*- or *c*-oriented MFI membranes are under compress stress along the in-plane direction

If our hypothesis is correct, the question that *b*-oriented membranes reported by Lai et al. didn't have cracks or defects is still remained. One possible reason would be that trimer-TPA could make different structure of grain boundaries that is more resistant to crack formation. It is concluded that *b*-oriented MFI membranes are desirable to skip the calcination step to avoid the formation of cracks or defects after secondary growth if one is willing to sacrifice small reduction of permeance from newly grown grain boundaries with closed pores.

6.3.3 Secondary growth time

In previous section, we hypothesize that *b*-oriented MFI membranes tend to generate cracks and defects compared to other oriented membranes. In order to avoid the formation of cracks or defects, we suggest that calcination of the membranes after secondary growth should skip over in the processes for the preparation of the *b*-oriented membranes. The experiment conditions to fill only the intercrystal gaps without covering entire the seed layer during secondary growth are needed to optimize.

First, optimization of the secondary growth time was investigated to make continuous *b*-oriented MFI membranes. Figure 6.5 (a) shows representative separation factors as function of permeability of *p*-xylene through the membranes synthesized by four different secondary growth times (115 min, 120min, 135 min, and 180min, respectively) at 175^{o}C. The seed layer was prepared by rubbing method using the seed crystals with 1.3 μm length on the α-Al_2O_3 porous supports and 20 nm of Au passivation

layer was deposited on the surface of seed layer. Then secondary growth at 175^{o}C was carried out to make continuous membranes with four different secondary growth times.

The permeability of the membrane with the secondary growth time of 180 min is almost 30 times lower than permeability of the membranes calcined, which indicated that 96 % of surface area of membranes has been covered by newly overgrown layer as shown in Figure 6.5 (d). However, the short time of secondary growth (from 115 to 135min) was not filled all the gaps between seed crystals resulting in opening the gaps as shown in Figure 6.5 (b) and (c).

The separation factors for all samples indicate that xylene isomers go through those silicalite-1 MFI membranes resulting in no separation. For the short time of secondary growth from 115min to 135min, hole defects were found on the membranes. The membranes with secondary growth time of 180 min also showed low separation factor, which suggest that xylene isomers passed through the non-zeolitic pores existed in 4 % of the active membrane surface. The size distribution of the intercrystal gaps may cause in generating hole defects within the narrow range of secondary growth times. The narrow intercrystal gaps produce newly overgrown layer over the seed layer in short time, while the wide intercrystal gaps are not filled within growth time. Also, those short secondary growth times at 175^{o}C might be difficult to make high degree of intergrowth between seed crystals. Lower temperature of secondary growth, for instance 120 ~ 130^{o}C may be desirable to control degree of intergrowth between seed crystals providing wide range of secondary growth time.

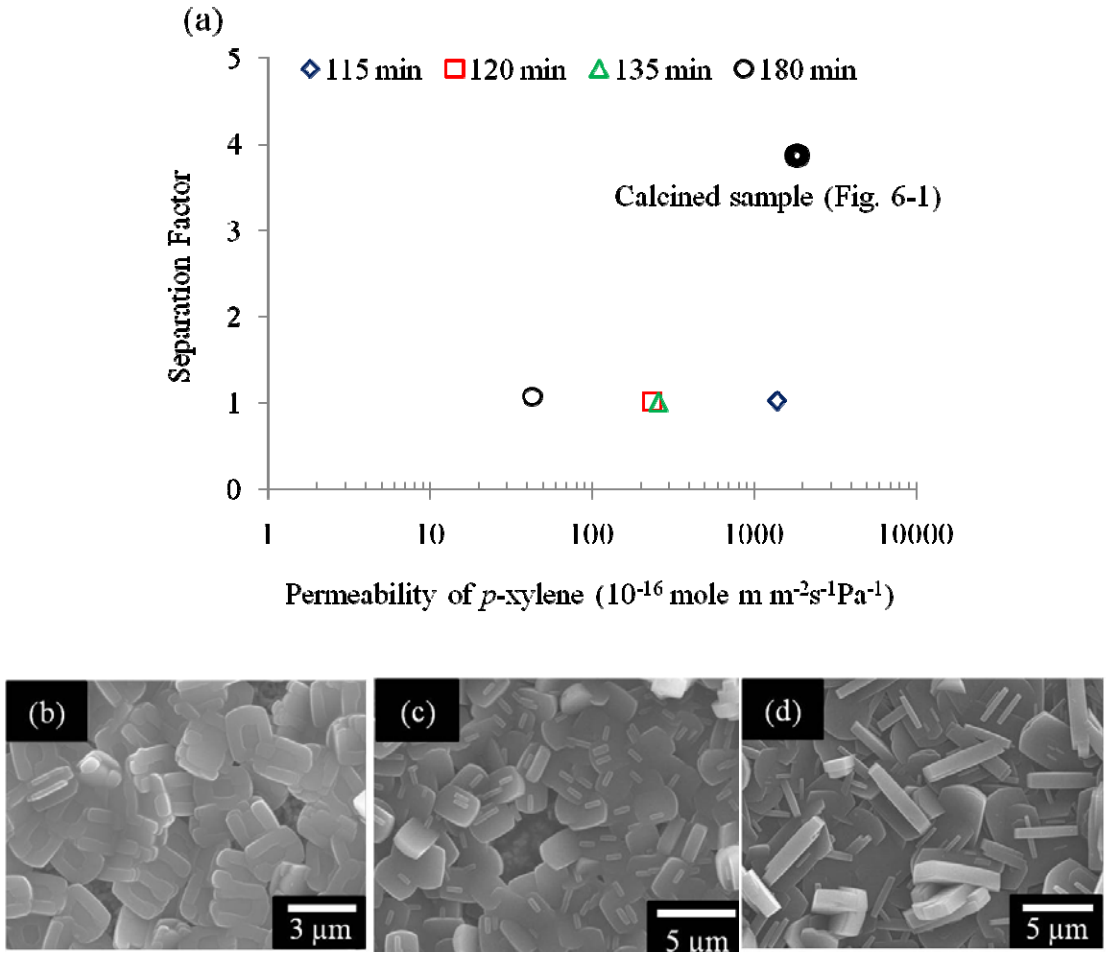

Figure 6.5 (a) Separation factors as a function of the permeability of *p*-xylene through silicalite-1 membranes synthesized by four different secondary growth times; 115 min (diamond), 120min (square), 135 min (triangle), and 180 min (circle), Top view of SEM micrographs for the secondary growth time of (b) 115 min, (c) 120 min, (d) 180 min

6.3.4 The effect of thickness of Au passivation layer

The Au/Pd passivation layer prevents not only growing the seed crystals along the out of plane direction (i.e. along the b-axis) but also generating twin crystals on the faces of seed layer. Once the intercrystal gaps are filled, newly overgrown layer in the gaps starts to grow along the in-plane direction to cover over the seed layer due to the fastest growth rate along the c-axis (i.e. in plane direction). The size of intercrystal gaps is randomly distributed so that the area with narrow intercrystal gaps is easily covered over the seed layer. However, the wide intercrystal gaps need to more growth time to be filled entirely. To prevent overgrowth in the narrow intercrystal gaps, it is desirable to deposit thick Au layer on the seed layer.

The effect of the thickness of Au/Pd passivation layer on the xylene separation was measured by binary permeation of xylene isomers. All silicalite-1 membranes with 1.3 μm seeds were synthesized by secondary growth at 175^{o}C for 2h. Au passivation layer was deposited on the seed layer with 10nm, 20nm, 30nm, and 40nm thick, respectively. Separation factors of xylene isomers were plotted as function of permeability of *p*-xylene through the membranes in terms of thickness of Au passivation layer as shown in Figure 6.6 (a).

The silicalite-1 membrane passivated by 10nm of Au layer showed low permeability and separation factor. Compared to permeability of calcined sample, it was known that 80% of surface area of the membranes has been covered by newly overgrown layer after secondary growth. Representative surface SEM micrograph of this membrane in Figure 6.6 (b) shows many randomly oriented crystals on the surface of membranes.

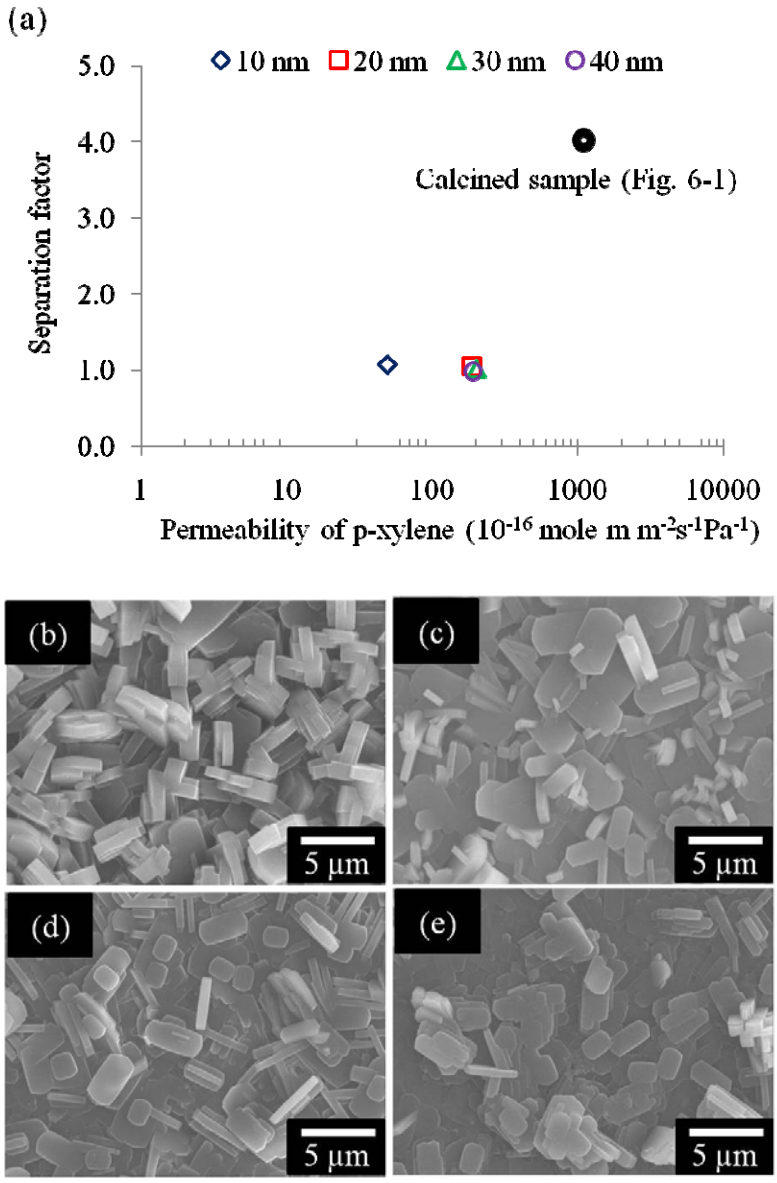

Figure 6.6 The effect of the thickness of Au passivation on the separation performance: (a) the plot of the separation factor for the silicalite-1 membranes with four different thickness of Au passivation as function of permeability of *p*-xylene. Top view of SEM image of membranes with Au passivation of (b) 10nm, (c) 20nm, (d) 30nm, (e) 40nm

In the case of thick Au passivation (40nm), the permeability of *p*-xylene through the membranes was increased to 5 times more than that of the silicalite-1 membrane with 10nm thick of Au passivation. 17% of total surface area was covered by newly overgrown layer and a few randomly oriented crystals were observed after secondary growth as shown in Figure 6.6 (e). The permeability of the membranes with 20nm and 30nm thick of Au layer were very similar to 40nm thick one. At the growth condition of 175^{o}C and 2h, Au passivation layer with the thickness of the range from 20nm to 40nm prevents overgrowth of seed crystals.

However, if the separation factors of four samples are considered, silicalite-1 membranes didn't separate xylene isomers showing the separation factor of around 1. We speculate that the wide intergrowth gaps might not be completely filled at those conditions providing non-zeolitic pathway. Also, there might be metal deposited on the planes of MFI seed crystals perpendicular to the substrate (i.e. the (100) and (001) faces), which might cause the mismatch at the interface between Au layer and newly overgrown layer. After removing Au passivation layer, the area of Au layer on the planes of MFI seed crystals perpendicular to the substrate might produce large voids such as defects. According to temperature dependence of permeation behavior through zeolitic or non-zeolitic pathway reported by Xomeritakis et al.[102] our permeance data were decreasing with temperature (data are not shown) indicating permeation through mesoporous diffusion pathway.

6.3.5 Control of the size of the intercrystal gaps by using mixed size seeding

For the improvement of separation performance, it is necessary to control distribution of the size intercrystal gaps and intergrowth of seed crystals. We controlled the size of the intercrystal gaps by filling smaller size of silicalite-1 seed crystals in the gaps between larger silicalite-1 seed layer. Figure 6.7 showed the separation performance and morphology of the silicalite-1 MFI membranes fabricated with filled gaps by smaller size of seed crystals. The seed layer was formed by depositing larger seed crystals with 1.3μm and smaller crystals with 0.15μm were filled in the gaps by rubbing method. Seed layer then was calcined to open the pores at 475^{o}C for 8h with 0.5^{o}C/min ramp rate. Au passivation layer with 20nm in thickness was deposited on the surface of the mixed seed layer, secondary growth was carried out using three different conditions: 1)175^{o}C, 2h, 2) 125^{o}C, 4h, and 3) 125^{o}C 6h. After secondary growth, Au passivation layer was removed by wet etching then dried completely prior to measure the permeance of xylene isomers.

For the sample grown at 175^{o}C for 2h, smaller seed crystals in the gaps between larger seed crystals were not grown to fill the intercrystal gaps due to the short time of secondary growth as shown in Figure 6.7 (b). No separation for xylene isomers was obtained through this membrane in Figure 6.7 (a). To improve intergrowth of seed layer, secondary growth is carried out at low temperature of 125^{o}C. Two membranes were synthesized at 125^{o}C for 4hr and for 6hr, respectively. In case of the sample grown at 125^{o}C for 6h, small seed crystals in the intercrystal gaps were emerged and overgrown over the seed layer as shown in Figure 6.7 (d). The permeance behavior of this sample

indicates that non-zeolitic pores are a dominant pathway resulting in separation factor around 1.

For the sample grown at 125^{o}C for 4h in Figure 6.7 (c), representative top view of SEM shows that smaller crystals were connected in the gaps and were not covered over the surface of seed layer. We expect that the dominant permeance pathways are zeolitic pores in seed crystals and non-zeolitic pores would not be existed in the membranes from the surface morphology. However, from the permeance behavior and separation, this is not the case. Separation factor of this membrane was around 1 indicating no separation of xylene isomers. When the permeance and separation factors obtained the silicalite-1 MFI membranes with different synthesis conditions were considered, all samples showed low separation factors. Based on the results, one possible scenario for the low separation factor of our membranes is described in the next section.

6.3.6 A scenario for the low separation performance

The key feature of our novel method is to passivate the surface of seed layer by depositing Au layer. The passivation Au layer prevents seed crystals from growing along the out of plane direction (along the b-axis) and allows them to grow along the in-plane direction. In order to make continuous silicalite-1 membranes with preserving orientation of seed layer during secondary growth, it is critical for Au passivation layer only to deposit on the faces of the seed layer parallel to substrates. If the Au is depositing on the faces of seed crystals perpendicular to substrates, the side of seed crystals might be prevented growth of seed crystals along the in-plane direction.

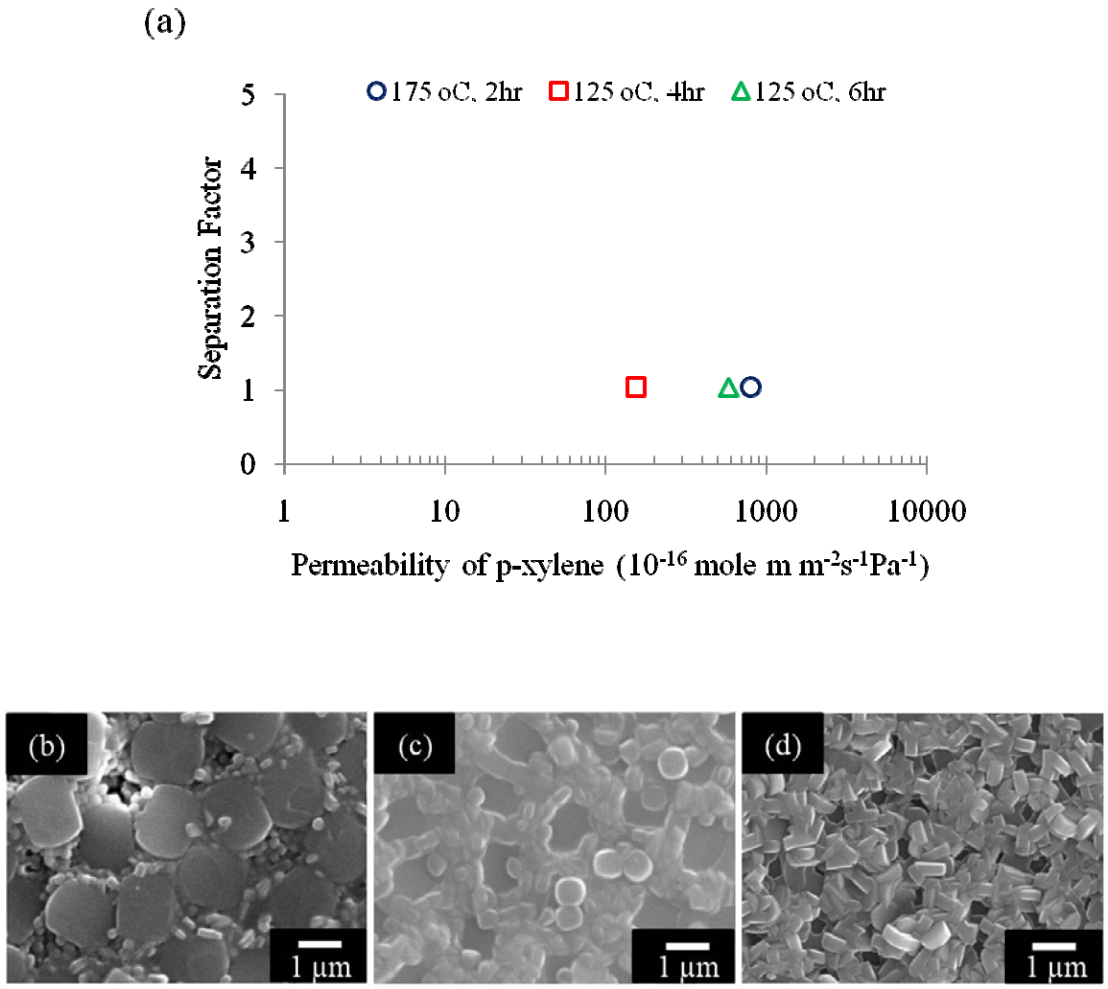

Figure 6.7 Silicalite-1 membranes with filled the gaps by using smaller seed crystals (1.3 µm as tiles and 0.15 µm as mortar): (a) the plot of the separation factors as function of permeability of *p*-xylene. Top view of SEM images of membranes with different secondary growth conditions (b) 175^{o}C, 2h, (c) 125^{o}C, 4h, and (d) 125^{o}C, 6h

Sputtering is a line of sight deposition method on the substrates. The target material bombarded with positive argon ions is sputtered away and deposited directionally onto the substrate. For this reason, the sputtering technique is chosen for the formation of Au passivation layer deposited on the faces of seed layer parallel to substrates. Figure 6.8 illustrates a scenario for the low separation performance obtained in our membranes. As discussed previous paragraph, Au layer deposited on the faces of seed crystals parallel to substrates may affect the intergrowth of seed crystals in the membranes. First, the Au layer could prevent growth of the seed crystals along the in plane direction, resulting in discontinuous membranes. Second, the Au layer might block the interconnection between seed crystals, which may form the voids at the interface between Au and newly grown silicalite-1 layer. The voids could provide non-zeolitic pathways that *o*-xylene go through the membranes along with *p*-xylene showing no separation performance.

To prove the scenario for the low separation performance, elements analysis is carried out by taking EDS as shown in Figure 6.9. The membrane shown in Figure 6.7 (c) is chosen and three areas that seed, grain boundary, and interface between seed and newly grown layer in the gap are taken for element analysis. At the surface of seeds, Au molecules are not detected (area 1). Au passivation layer on the silicalite-1 membranes is etched away after secondary growth. However at the gaps and the interface between larger seeds and smaller seeds grown (area 2 and 3), Au molecules are detected. Au molecules on the smaller seed crystals in the gaps are covered by newly grown silicalite-1 crystals after secondary growth such that etching solution cannot be reached to the Au layer.

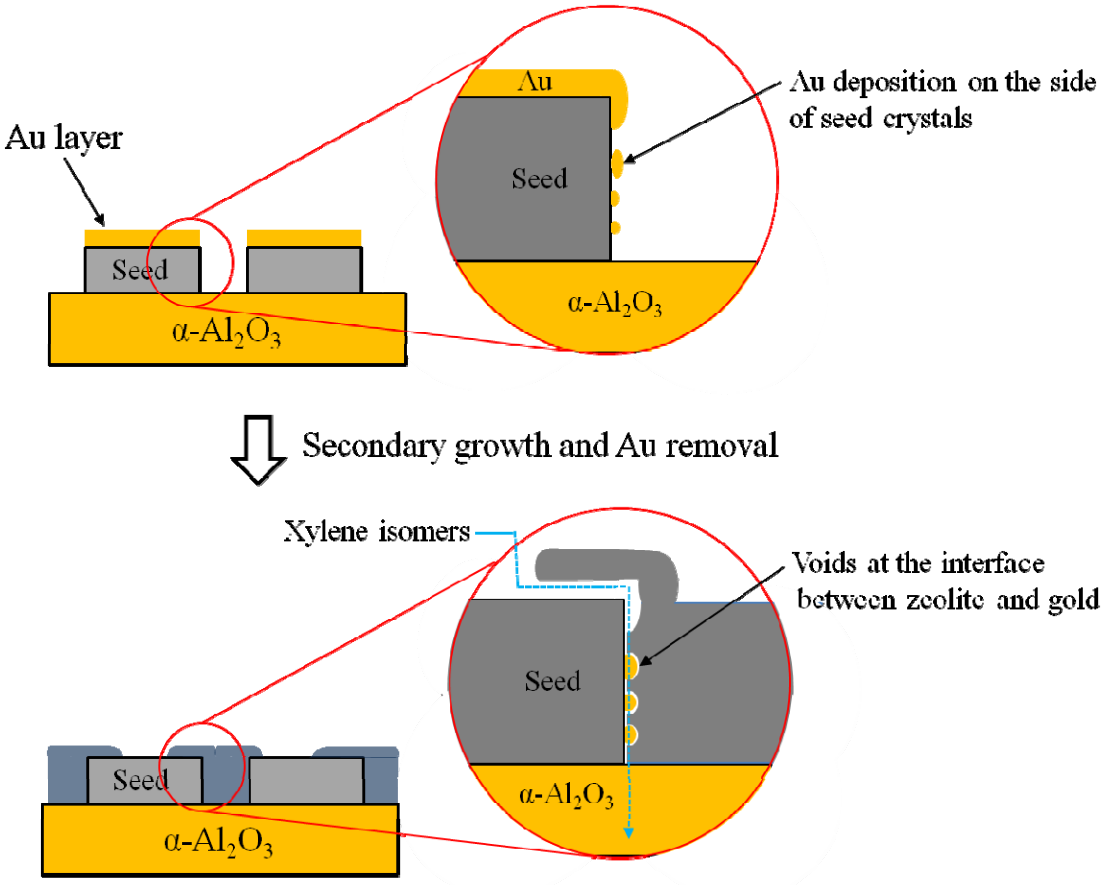

Figure 6.8 Schematic illustration for the low separation factor of xylene isomers through *b*-oriented silicalite-1 membranes fabricated by micro-tiles-and-mortar method

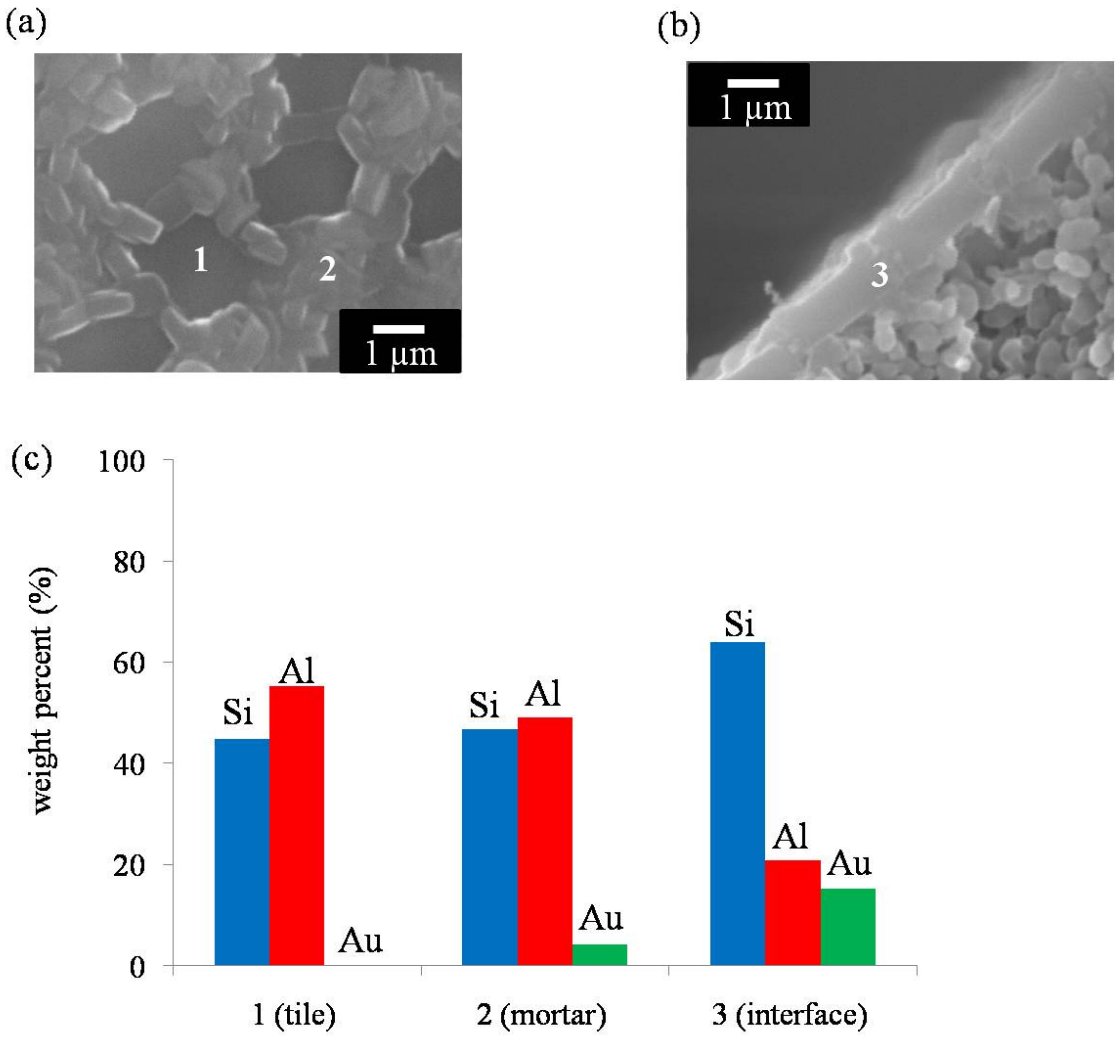

Figure 6.9 Element analysis of the silicalite-1 membranes by EDS. (a-b) top view and cross sectional SEM images (c) amount of elements detected at three different positions in the silicalite-1 membranes. The membrane was synthesized at 175^{o}C for 4 h with mixed size seed layer (1.3µm as tiles and 150nm as mortar). The Au passivation layer was deposited with 20 nm thick. After secondary growth, Au passivation layer was etched by wet etching solution (HCl: HNO_3: H_2O=3:1:2 volume ratio)

At the interface, as illustrated in Figure 6.8, Au molecules could be deposited on the faces of seed crystals perpendicular to substrates preventing interconnection of seed crystals, which result in forming voids at the interface. It is critical issue to prepare *b*-oriented silicalite-1 membranes by our novel method. It might be one reason why our membranes showed low separation performance even though they were fabricated with different conditions.

To avoid the formation of voids by Au passivation layer, one possible way is to make gold-silicon eutectic alloy at the interface between Au and silicalite-1 seed crystals, which may close the voids. According to gold-silicon phase diagram, it was reported that the eutectic temperature is $363 \pm 2^{o}C$.[137] The silicalite-1 membrane shown in figure 6.7 (c) was tried to make gold-silicon eutectic alloy at $465^{o}C$ for 8h and was measured binary permeation again to see the effect of the formation of gold-silicon eutectic alloy on the permeation. Figure 6.10 shows binary permeance behaviors as function of temperature for the silicalite-1 membranes before and after eutectic reaction. Before the eutectic reaction, no separation performance for the xylene isomers is obtained due to the non-zeolitic pores such as voids. After the eutectic reaction at $465^{o}C$ for 8h, the permeance of *p*-xylene increases about 8 times higher than that of the membranes before eutectic reaction. This behavior is because the pores in grain boundaries are also opened during eutectic reaction at high temperature. The separation factor after the reaction is a little increased. The slight increase of separation factor indicates that some of the voids might be closed during the reaction, but there would be still many voids needed to be closed. However, this approach shows the possibility to

improve separation performance of the *b*-oriented silicalite-1 membranes fabricated by the micro-tiles-and-mortar method.

The critical problem of the Au passivation by sputtering is to deposit the faces of seed layer perpendicular to the substrate. In order to solve this issue, we suggest surface modification of seed crystals using hydrophobic silane coupling agents by stamping method. The idea is that the faces of seed layer parallel to the substrate is modified with fluorosilicone ($CF_3(CF_2)_9C_2H_4Si(OCH_3)_3$) by the PDMS stamping. First, fluorosilicone is coated on the PDMS stamp by spin coating that is able to control the thickness of fluorosilicone. By PDMS stamping on the seed layer, the fluorosilicone layer is transferred to the faces of seed layer parallel to the substrate, which can act as passivation layer like Au passivation. It is worth to mention that the stamping method can transfer the fluorosilicone only on the surface of seed layer without coating the faces of seed layer perpendicular to the substrate. Thus the seed layer can grow to fill the intercrystal gaps.

Figure 6.11 shows the feasibility results for the passivation of fluorosilicone by stamping method. The silicalite-1 seed layer is passivated by fluorosilicone by PDMS stamping and then is carried out secondary growth at 175^{o}C for 90 min and 115 min, respectively. It is observed that the surface of seed layer passivated fluorosilicone didn't show crystal growth along the out of plane direction and the faces of seed layer perpendicular to the substrate grow to fill the gaps, which indicate that the fluorosilicone can work as the passivation layer. These are very feasible results so that the optimization for the preparation of silicalite-1 membrane is needed.

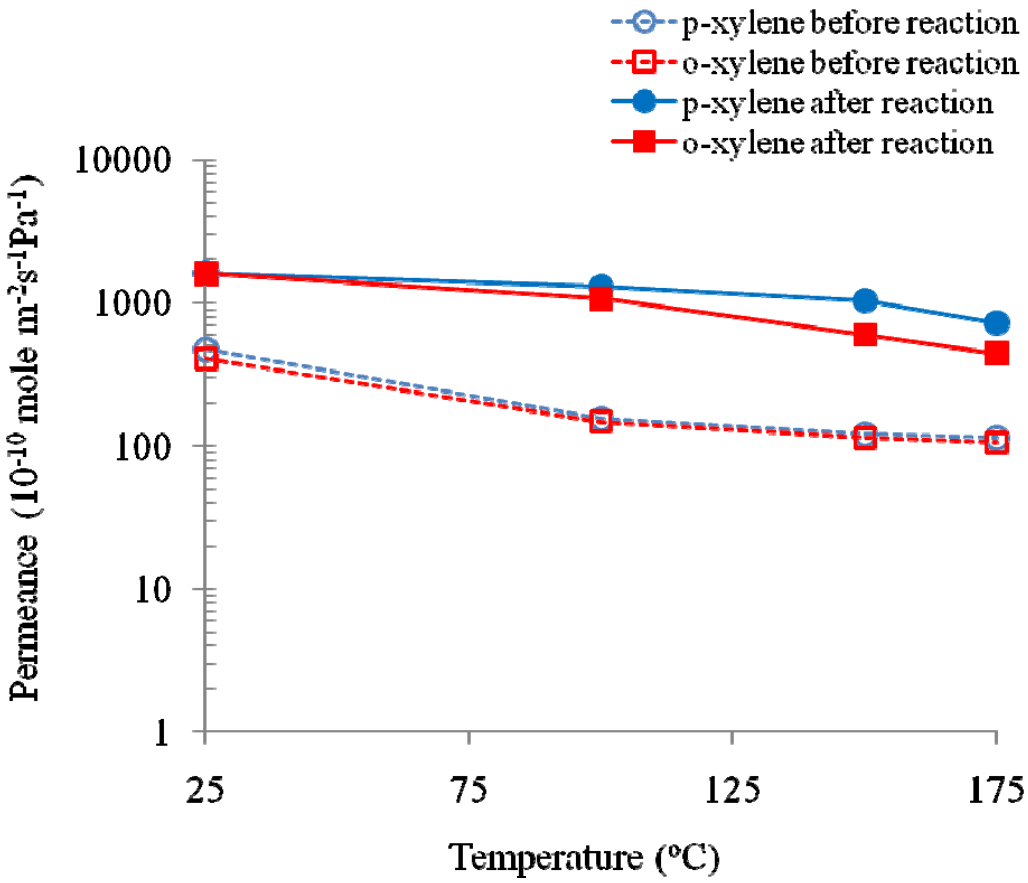

Figure 6.10 Permeance of xylene isomers through b-oriented silicalite-1 membranes before and after eutectic reaction. Solid lines represented the permeance of xylene isomers after the eutectic reaction and dashed line before the eutectic reaction. Blue circle symbol represents *p*-xylene and red rectangle for *o*-xylene. Silicalite-1 membrane was prepared by secondary growth at 125^{o}C for 4h. Eutectic reaction was carried out at 465^{o}C for 8h

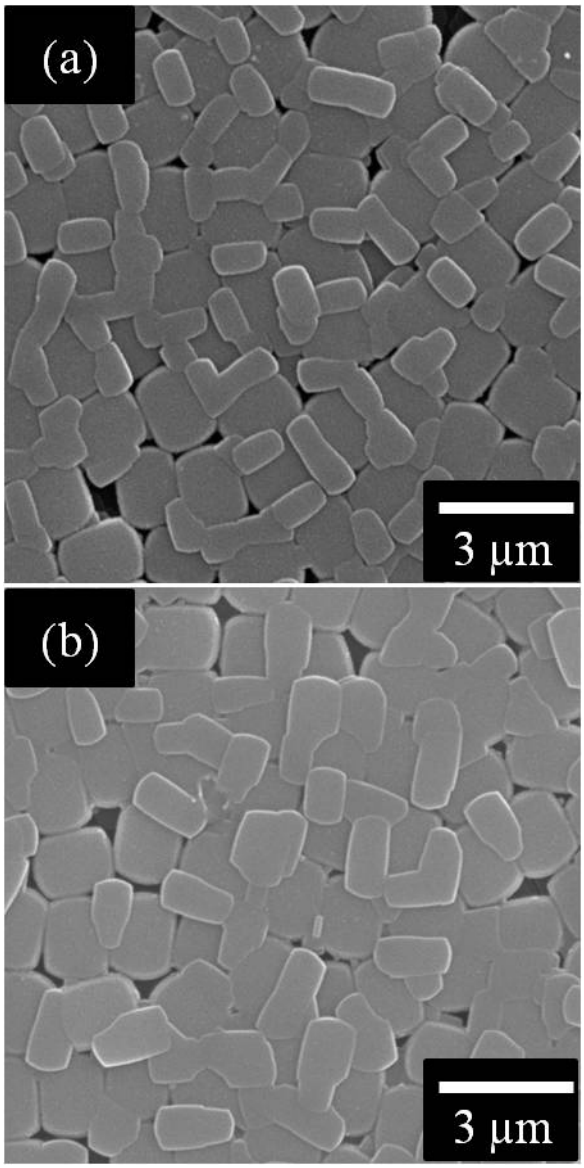

Figure 6-11. Top view SEM images of the silicalite-1 films with the passivation of fluorosilicone by PDMS stamping method after secondary growth at 175^{o}C for (a) 90 min, (b) 115 min

6.4 Conclusion

We demonstrated the separation performance for the xylene isomers through *b*-oriented silicalite-1 membranes fabricated by the micro-tiles-mortar method. The separation performance of our membranes was very different from that of membranes reported by Lai et al. because the cracks or defects were formed on the membranes during calcination. We proposed a hypothesis of the formation of cracks or defects according to the orientation of membranes. It was concluded that *b*-oriented membranes could easily form the cracks or defects compared to other orientation.

Based on the hypothesis, it was decided that fabrication of the *b*-oriented membranes should stop prior to calcination step to prevent cracks. To determine optimization conditions such as secondary growth time, thickness of Au passivation, and mixed size seed layer were accomplished and measured binary separation. However those parameters didn't improve the separation performance. Low separation might casue from the distribution of the size of the intercrystal gaps. At the current secondary growth condition, narrow intercrystal gaps were easily overgrown over the seed layer and wide intercrystal gaps were not filled completely resulting in hole defects.

To minimize the distribution of the size of the intercrystal gaps in the seed layer, smaller size of seed crystals (150nm) were filled the intercrystal gaps as mortar. Then, silicalite-1 membranes were synthesized with mixed size seed layer, but no separation was obtained. We speculated that Au deposition layer could deposit the faces of seed crystals perpendicular to the substrates which may generate voids at the interface between zeolite and Au. The element analysis by EDS conformed that Au existed at the

grain boundaries and interface between silicalite-1 and Au passivation resulting in the formation of voids. The voids were tried to close by Au-silicon eutectic reaction at 465^{o}C for 8h. Separation factor was a little increase after eutectic reaction. To effectively passivate the seed layer, we suggested that fluorosilicone were deposited on the seed layer by PDMS stamping and subsequently, secondary growth was carried out. The feasible data showed the possibility of fluorosilicone as passivation layer. The optimization for the fluorosilicone is needed to study.

CHAPTER VII

GENERATION OF MONODISPERSE MESOPOROUS SILICA MICROSPHERES WITH CONTROLLABLE SIZE AND SURFACE MORPHOLOGY IN A MICROFLUIDIC DEVICE*

7.1 Introduction

Surfactant-templated ordered mesoporous silica (hereafter OMS) are highly ordered materials containing uniform pores in the range of 2 – 50 nm,[138-140] thus finding a range of applications in catalysis,[14] selective adsorption, separation,[15, 16] drug delivery,[20] and electronics.[21] Mesoporous silica spheres of uniform size are of particular interest due to their potential applications in non-conventional areas such as sensors,[17, 18] biomolecule delivery,[19] and potentially micro devices. In addition to the uniformity in size, the controlled surface morphology would be desirable to extend their applications.

Yano and co-workers have reported a modified Stober method to synthesize monodisperse mesoporous silica particles of controllable size in submicrometer scale.[22] They have also been able to make core-shell type mesoporous silicate spheres with hydrophilic core and hydrophobic shell by preparing the spheres in a successive manner.[25] Ward and co-workers have used a spray drying method, which is an evaporation-induced self-assembly (EISA) method, using a well-defined orifice to prepare monodisperse mesoporous silicate spheres of several micrometers.[23, 141] Despite

* This is the pre-peer reviewed version of the following article: "Generation of monodisperse mesoporous silica microspheres with controllable size and surface morphology in a microfluidic device" by I. Lee, Y. Yoo, Z. Cheng, and H.-K. Jeong, Advanced Functional Materials 2008, 18 4014-4012.

these efforts, it is still of technological challenge to have precise control of particle size over wider ranges, surface morphology, and multi-functionality.[25] Andersson, et al., recently reported the preparation of well-ordered 2D hexagonal OMS microspheres by combining emulsification and solvent evaporation (ESE) in oil,[142] in a way similar to the EISA process in liquid/gas system. This work paves a way to the possibility to generate inorganic mesoporous materials in the microfluidic devices by the EISA process.

Making particles in microfluidic devices is of great interest due to its ability to control size, shape, internal structures, and multi-functionalities by generating droplets of precursor solutions and rapidly converting the droplets into particles with various sizes and shapes.[26-35, 37] Although the generation of monodisperse multi-functional polymer particles (either spherical or non-spherical) in microfluidic devices has attracted a great deal of research interest over the last decade, the one-step *in situ* synthesis of inorganic mesoporous materials using microfluidic devices still has technological difficulties. Unlike polymeric materials, mesoporous materials require long formation times that are difficult to provide in typical microfluidic devices that involve fast fluid flow through short devices. Recently, Carroll and co-workers reported generation of monodisperse mesoporous microspheres with worm-like disordered pore structure by forming uniform droplets of an aqueous-based precursor solution in a microfluidic device followed by an EISA process.[143] Their method, however, is a two-step process in which monodisperse precursor droplets are first generated in the microfluidic device and the formation of mesostructures follows *ex situ* in a batch reactor outside the microfluidic device. This might pose limitations to the realization of the full potential of

microfluidic-based particle generation (for instance, controlling particle morphology and generating Janus particles). Though an aqueous-based sol is more desirable when biological molecules or cells are involved, an ethanol-based sol offers better opportunity to obtain highly ordered structures with a variety of crystal lattices.[24, 144]

In the present work, we report a one-step *in situ* method that combines a microfluidic emulsification technique and a rapid solvent diffusion-induced self-assembly technique inside microfluidic devices (referred as microfluidic DISA which is an equivalent EISA but in liquid/liquid systems) to generate highly ordered mesoporous microspheres. Uniform droplets of an ethanol-rich precursor solution are generated in the soft microfluidic devices upstream and are subsequently allowed into the mesostructured surfactant/silica microspheres downstream by rapid solvent diffusion-induced self-assembly in the microfluidic channels. Our method, microfluidic DISA, makes it possible to control the particle sizes in the scale of micrometers and also to manipulate the surface morphologies of the OMS spheres by changing synthesis parameters such as the design of microfluidic channels, the flow rate of the precursor solution and oil, and the type of oil. It is expected that OMS microspheres with precisely controlled size and surface morphology might be very useful for advanced applications such as in sensors, biomolecule delivery, and micro devices.

7.2 Experimental

7.2.2 Materials and chemicals

All chemicals were used as received without further purification. Tetraethylorthosilicate (TEOS) and Sigmacote® were purchased from Sigma-Aldrich. Hexadecane (98%) and acetone (99.5%) were supplied by Fisher chemicals. Ethanol (99.5%) and isopropanol (99.5%) were acquired from Acros. Span®80 (sobitan monoloeate, viscosity 1200 ~ 2000 mPa·s at 20^{o}C) was supplied by Fluka. Poly (dimethylsiloxane) elastomer (Sylgard 184) was purchased from Dow corning. P135 (a polymeric PEG-30 dipoly(hydroxysterate)) was kindly provided by Uniquema. All Pluronic block copolymers (L121, P104, P105 and F108) used in this study were obtained as gifts from BASF Corp. (Parispany, NJ).

7.2.2 Preparation of precursor solution

Typical mesoporous silicate precursor solution was prepared by hydrolyzing 5.2g TEOS in the mixture of 6 g ethanol and 2.7 g dilute hydrochloric acid (0.07 M, pH 2) solution under vigorous stirring at room temperature for 20 min. 0.8 g of P104 (a pluronic block copolymer) was dissolved in 8g of ethanol before being mixed with the hydrolyzed TEOS solution. The final molar ratio was 1TEOS: 0.005 P104: 12.174 Ethanol: 0.0176 HCl: 5.97 H_2O.

7.2.3 Fabrication of PDMS microfluidic devices

PDMS microfluidic devices were fabricated using a soft lithography procedure.[145] These devices were made of rectangular channels of 100 μm height and 100 μm widths. The flow focusing point of the devices was decreased to 50 μm. The PDMS devices were placed on glass slides coated with PDMS films to ensure that precursor only contacts to the PDMS surfaces. In order to prevent the precursor solution from wetting on the PDMS surface, the surface of PDMS was coated with Sigmacote®, a water-repellant.

7.2.4 Characterization

Precursor and oil phase were supplied to the microfluidic devices using syringe pumps (PHD-2000, Harvard Apparatus). Droplet generation is observed using a high-speed camera (Phantom V4.2, Vision Research) mounted on an inverted optical microscope. OMS spheres were imaged using an optical microscope (Axiovert 200M, ZEISS) and scanning electron microscope (JEOL JSM-6400). Mesostructures of the OMS spheres were characterized using a JEOL JEM-2010 transmission electron microscope (TEM) operating at 200 kV and a small angle X-ray scattering (SAXS, Bruker-AXS) with Cu-Kα radiation (λ = 1.54 Å).

7.3 Results and discussion

7.3.1 Generation of monodisperse OMS droplets in the microfluidic device

Figure 7.1 (a) shows schematic illustration of the synthesis of OMS particles in a microfluidic device. Monodisperse emulsion droplets are generated in a T-shape hydrodynamic-flow-focusing geometry[38] by introducing two perpendicular intersecting flows, one continuous oil phase and the other ethanol-rich precursor phase through microchannels. The flow-focusing geometry enables continuous breakage of the precursor flow into droplets by controlling the relative flow rates of the two fluids. An optical micrograph in Figure 7.1 (b) shows the formation of uniform OMS precursor droplets at the T-junction as a result of competition between viscous stress and capillary stress stemming from the surface tension of the two immiscible fluids.[146] In order to stabilize the droplets of the precursor solution in the oil phase, oil-soluble emulsifying reagents are required. While most of the studies in emulsion technology have been done on either water-in-oil or oil-in-water droplets, relatively few studies have been carried out on ethanol-in-oil emulsions where the amphiphilic nature of ethanol poses a challenge. To address this challenge, we have investigated various emulsifiers with different hydrophile/lipophile balance (HLB) and identified a diblock copolymer, P135 (HLB = 5.5), as an emulsifier to make rather stable ethanol-rich precursor droplets in oil. Another challenge was to prevent the coalescence of the ethanol-rich droplets in the microchannels due to the inherent instability of the ethanol-rich emulsion droplets. The coalescence of the droplets can result from the collision of the droplets.

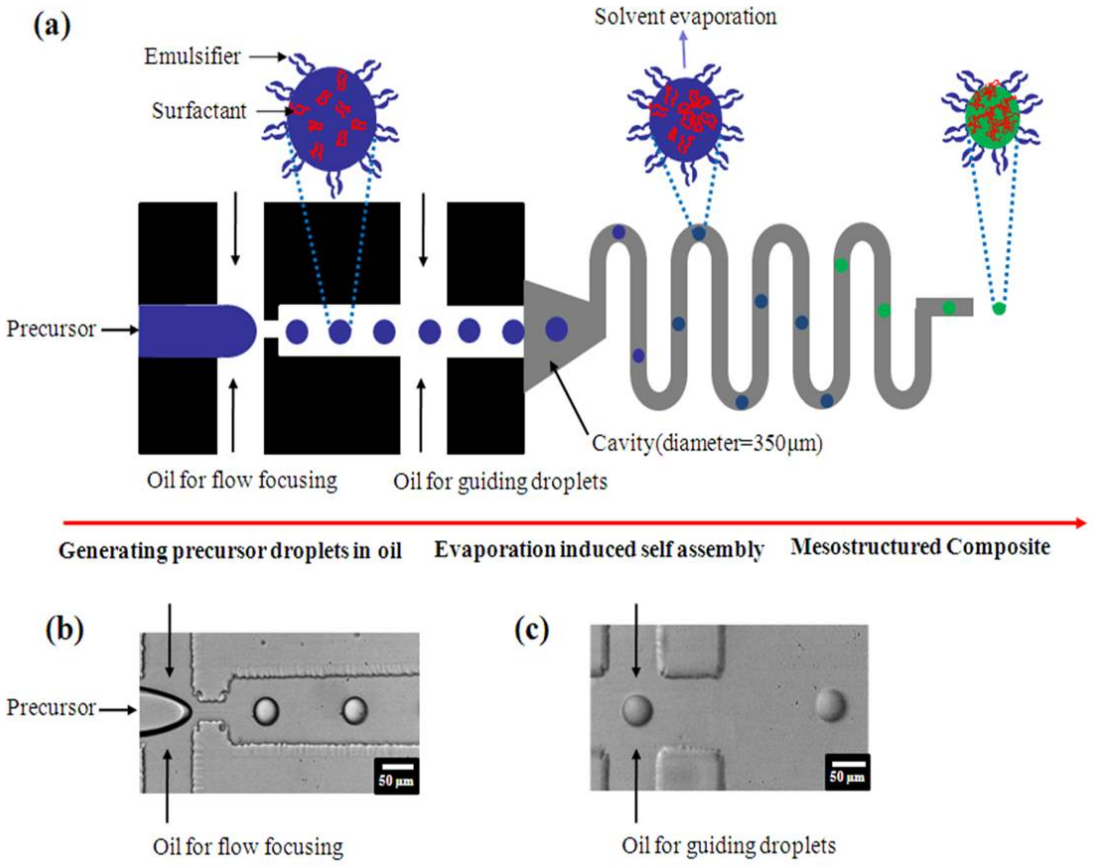

Figure 7.1 (a) Schematic illustration of the synthesis of OMS particles using μ-fluidic EISA. Monodisperse droplets are generated at the T-shape flow-focusing orifice and assembled into mesostructured silica/surfactant composite spheres via rapid diffusion-induced self-assembly (DISA) process *in situ* within the microchannel. Optical micrographs of the T-shape flow-focusing orifice generating droplets at the orifice (b) and the T-junction for guiding flow to prevent droplet collision by increasing inter-droplet distance (c)

In a cavity (about 350 μm diameter) in the downstream (see Figure 7.1 (a)) designed to connect to the collecting tube, the speed of the droplets entering from the microchannel (about 100 μm diameter) reduces substantially (~$(1/3.5)^2$ times) due to the decrease of the velocity of the continuous oil phase. This sudden decrease in velocity induces the collision of the droplets in the cavity and creates coalescence of the droplets.

To overcome the coalescence of the droplets, we added an additional flow to guide the droplets that is introduced immediately after the droplets are generated at the flow-focusing orifice as shown in Figure 7.1 (a) and (c). This guiding flow increases the speed of the oil phase, thereby preventing the collision of droplets by taking the droplets further apart. By the time droplets came out of the microfluidic channels, substantial amount of ethanol of the precursor droplets has already been removed within the microchannels. Therefore the formation of mesostructured surfactant/silicate hybrid microspheres takes place through the DISA process *in situ*. It is worth mentioning here that *in situ* DISA process within the microchannels is of practical importance by eliminating subsequent solvent evaporation step.

7.3.2 Size distribution of OMS microspheres

Figure 7.2 shows the fairly narrow distributions of the particle sizes after ethanol elimination within the microchannels (Figure 7.2 (a)) and after removal of surfactants by calcining at 500^{o}C for 5h (Figure 7.2 (b)). The coefficients of variation (CV), defined as standard deviation divided by average size of spheres, are 3.4% after elimination of solvent and 4.7% after removal of surfactant.

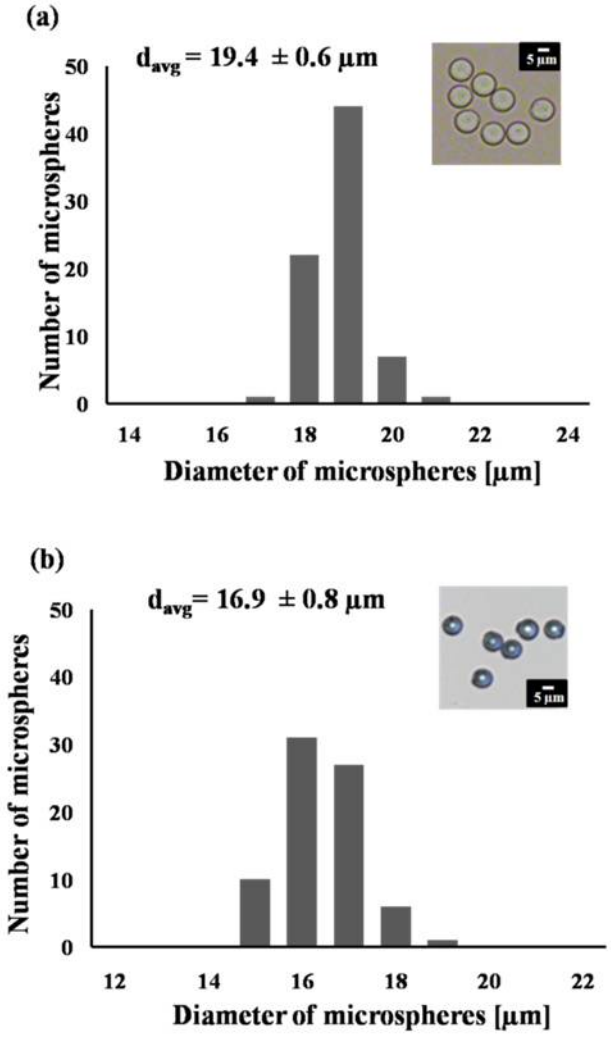

Figure 7.2 Particle size distributions and optical micrographs of (a) the mesostructured silica/surfactant composite microspheres after eliminating ethanol within the channel, and (b) the mesoporous silica microspheres after removing surfactants. Note the slight decrease of particle size after calcinations due to further condensation of silanol groups and complete removal of ethanol/surfactant molecules

We speculate the main source of the variation of the particle size comes from the fluctuation of the flow rates of the two fluids.[146] In principle, the monodispersity can, therefore, be further improved by using syringe pumps capable of better control over flow fluctuations. Inset optical micrographs confirm that both mesostructured hybrid and mesoporous microspheres are fairly monodispersed in size.

The size of the particles reduced about 12% after the removal of surfactant. This size reduction is attributed to the two factors: 1) complete removal of residual ethanol in the mesostructured hybrid spheres and 2) further condensation of silanol groups along with the removal of surfactants during the calcination step.

7.3.3 Control of surface morphology

Figure 7.3 shows typical SEM images of the OMS microspheres produced from the droplets in hexadecane and their surface morphology. As seen in Figure 7.3 (b) and (c), the surface of the OMS microspheres exhibits rough corrugated features in submicrometer scales (see also Figure 7.4). This roughened surface morphology of silica microspheres is very distinctive from the smooth surfaces of typical silica spheres prepared by other methods[22, 141, 147] and to the best of our knowledge, this type of surface morphology of OMS particles has not been reported. From a practical viewpoint, this rough surface may provide an efficient interface for external surface functionalization and nanocomposite applications. It is speculated that this distinctive surface morphology is due to the diffusion of oil-soluble precursor solution (ethanol, TEOS, and P104) into the oil phase and subsequent polymerization of inorganic silica precursors in the

interfacial subphase upon further diffusion of ethanol into the oil phase. Detailed explanation on a possible mechanism is given in the following paragraph. The structure of the surface was investigated using TEM and SEM as shown in Figure 7.4. The cross-sectional image of a broken microsphere shown in Figure 7.4 (a) reveals the thickness of the surface structure is about 2 μm.

A TEM micrograph shown in Figure 7.4 (b) reveals the presence of mesopores of larger than 15 nm in the rough surface. Figure 7.4 (c) shows a TEM image of well-ordered 2D hexagonal internal mesopores of about 5 nm.

Small-angle X-ray scattering data in Figure 7.5 shows only one diffraction peak at low Bragg angle assigned as (100) reflection with d-spacing of about 8.4 nm. The lack of higher order reflections such as (110) and (200) indicates that the structure is not as highly ordered as those prepared with the ESE method.[142]

It is speculated that the unique surface morphology of the OMS microspheres results from two kinetic processes: 1) diffusion of the precursor solution (i.e., ethanol, TEOS, HCl, and surfactant, P104) from the droplets to the hexadecane oil phase forming an interfacial subphase and 2) fast diffusion of ethanol from the interfacial subphase into hexadecane (as compared to the cases of the ESE method). Fast diffusion of ethanol is driven by a sharp concentration gradient of ethanol due to the continuously replenishing oil flow around the droplets in the microchannels as illustrated in Figure 7.6. This is in contrast to the ESE method,[142] where ethanol diffuses slowly in a batch reactor under vacuum since the solvent can only diffuse through the rather saturated hexadecane phase.

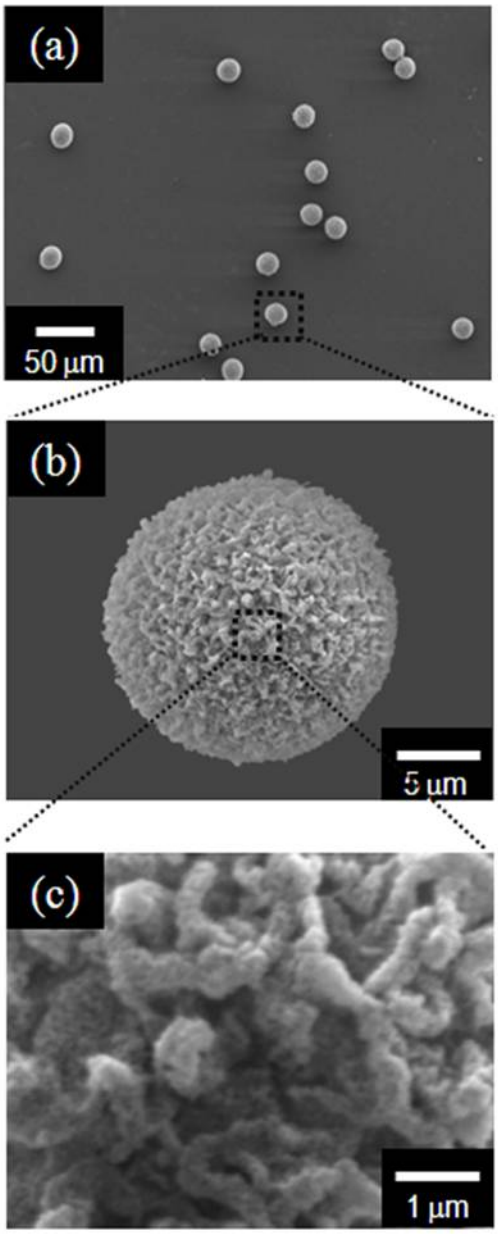

Figure 7.3 SEM images of typical mesoporous silica spheres at lower magnification (a) and at higher magnification (b) and a magnified image of the surface of an OMS sphere (c)

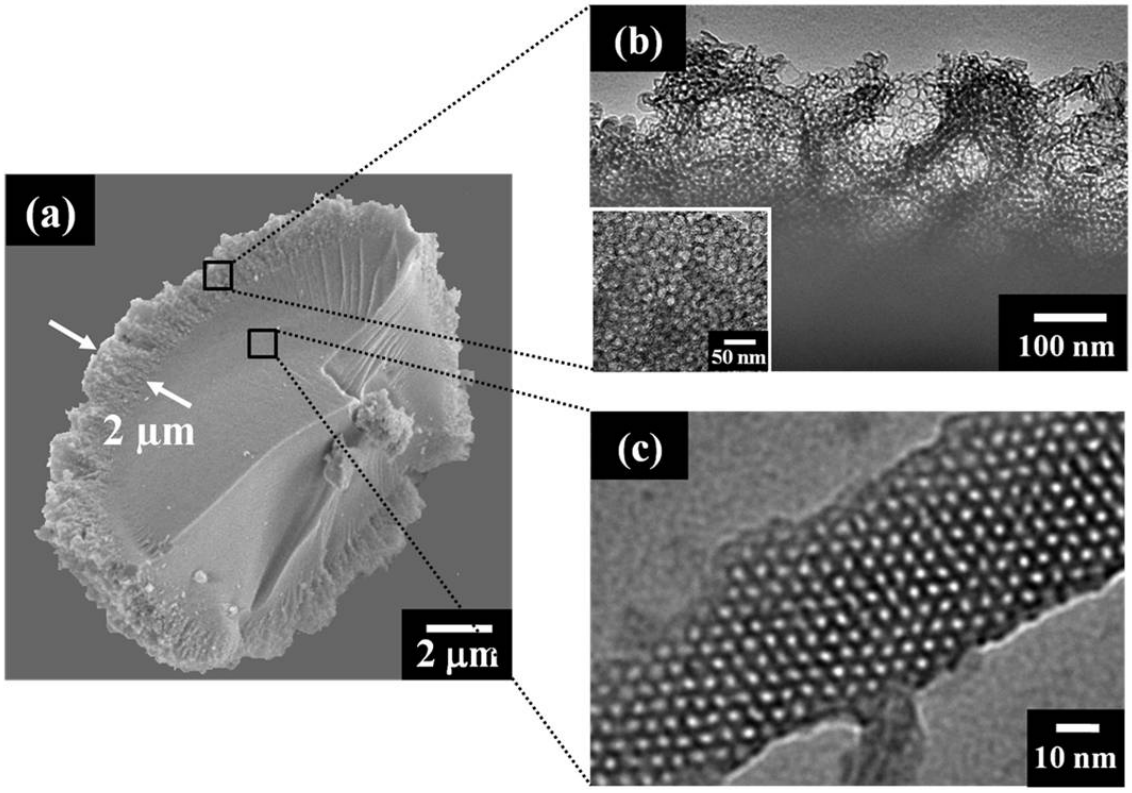

Figure 7.4 Electron micrographs of OMS microspheres: (a) a SEM cross section image of a fractured microsphere, (b) a TEM image of surface structure, revealing disordered worm-like mesopores of larger than 15 nm, and (c) a TEM image of internal structure, showing highly ordered 2D hexagonal pore structure of ~ 5 nm

This is also quite different from the case of Carroll and coworkers where aqueous-based precursor droplets were generated in a microfluidic device.[143] Since water does not readily diffuse into the oil phase in the microchannel, it requires *ex situ* evaporation of water in a macroscale batch reactor. As mentioned above, the droplets start to shrink due to the diffusion of ethanol into hexadecane right after the droplet formation at the flow focusing orifice (Figure 7.6 (a)). At the same time, oil-soluble TEOS and P104 can also diffuse into hexadecane along with ethanol (Figure 7.6 (b)). This diffusion of ethanol-rich precursor solution creates an interfacial subphase in which oil-soluble precursor solution and hexadecane are mixed along with the emulsifier (P135).[147] Ethanol continues to diffuse from the interfacial subphase to the hexadecane phase, thereby driving the self-assembly of surfactants and the polymerization of silica in the subphase (Figure 7.6 (c)). This process leads to the formation of irregular mesostructured silica shell in the interfacial region with a disordered worm-like structure of ~ 15nm and larger pores. It is surmised that these worm-like mesopores are dual-templated by surfactant (P104) and emulsifier (P135). Further diffusion of ethanol from the droplet core to hexadecane through the mesostructured shell results in well-ordered 2D hexagonal mesostructured silica cores of ~ 5 nm feature. We like to re-emphasize that both the formation of the interfacial subphase and subsequent fast diffusion of ethanol triggering the DISA process in the interfacial suphase are important for the formation of this unique surface morphology. If either one of the two kinetic processes did not exist, corrugated surface morphology would not have formed.

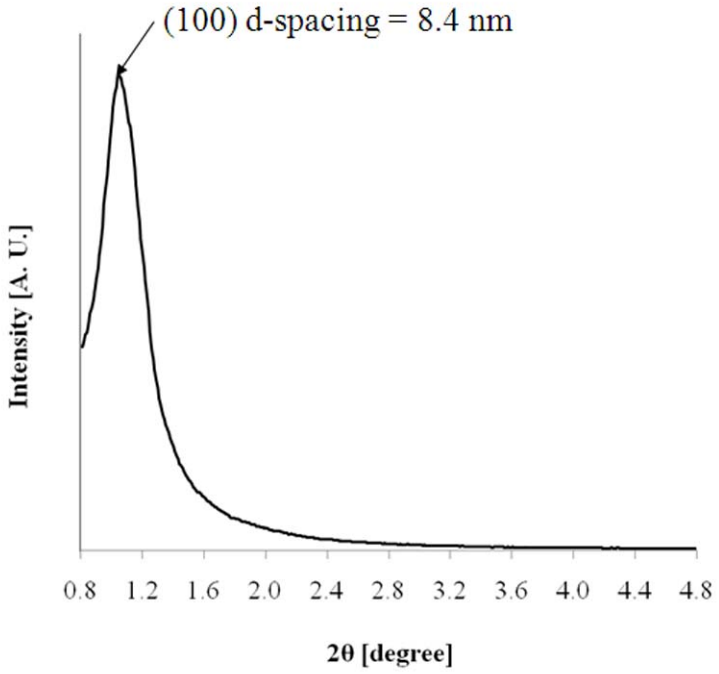

Figure 7.5 Small-angle X-ray scattering pattern of OMS microspheres

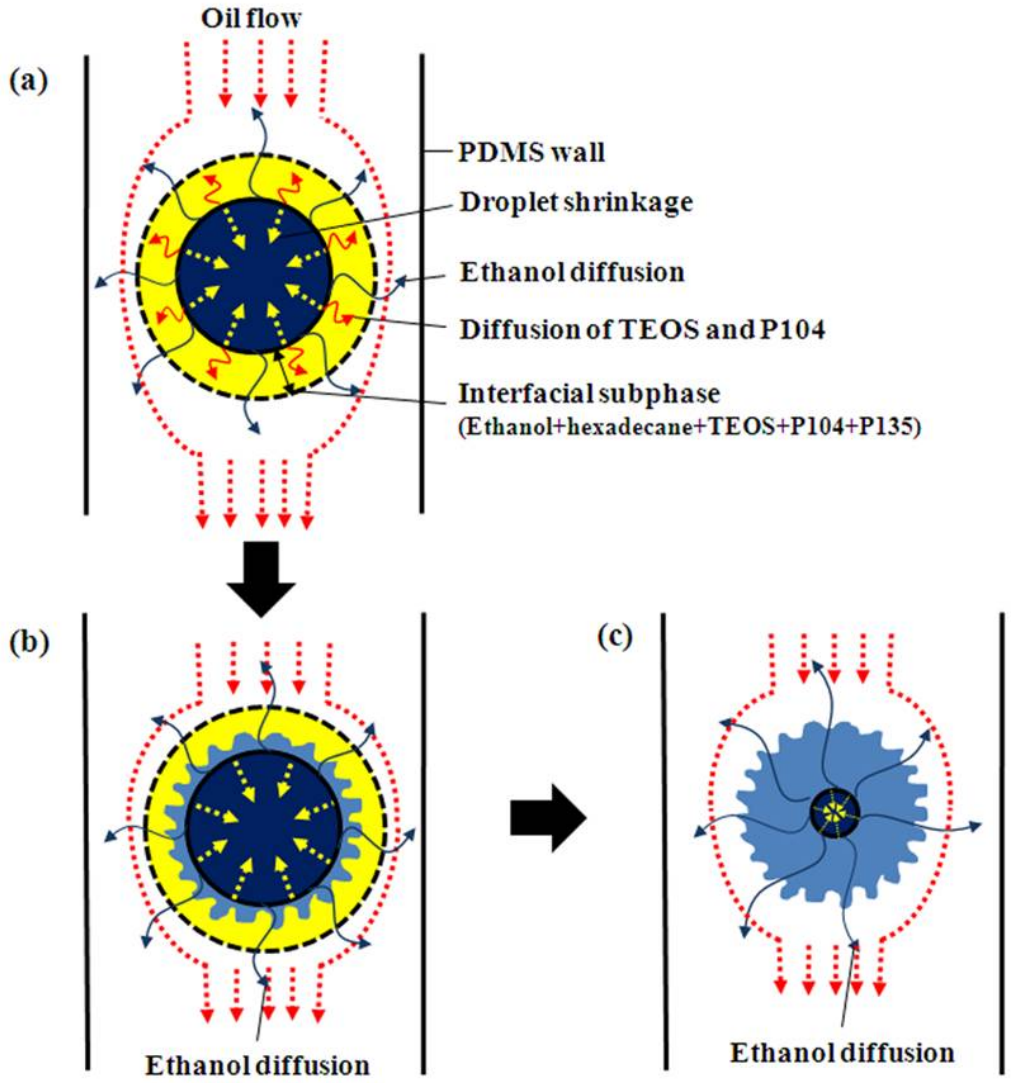

Figure 7.6 The process of solvent evaporation and self-assembly/polymerization inside a microfluidic channel; (a) formation of an interfacial subphase (b) formation of corrugated surface shell by fast diffusion of ethanol to hexadecane (c) formation of internal mesostructures by ethanol diffusion through shell structure

For instance, in the case of the ESE method,[142] ethanol evaporation is too slow and for the aqueous-based sol in microfluidics,[143] there is no interfacial subphase formed. Therefore, both cases produce mesoporous silica spheres with smooth surface morphology. If the above hypothesis holds, it is possible to control the surface structures of the mesoporous silica spheres by changing either the formation of subphase or the diffusion rate of solvent.

One simple way to change both the formation of subphase and the diffusion rate of ethanol is by changing solubility of ethanol in oil phase. This can be done by using different types of oil: for instance, immiscible mineral oil as opposed to partially miscible hexadecane (i.e. slower diffusion rate of ethanol in mineral oil).

Indeed, the OMS microsphere generated in mineral oil (Figure 7.7 (b)) shows smoother surface morphology as compared to that in hexadecane (Figure. 7.7 (a)). It is worthy of mentioning here that the droplets generated in the mineral oil needed to be further evaporated *ex situ* due to slow diffusion of ethanol. The smoother surface of OMS spheres made in mineral oil is presumably due to the fact that there is virtually no interfacial subphase formed because of the low solubility of ethanol in mineral oil (i.e., slow diffusion). We have adjusted the diffusion rate of ethanol from the droplets by altering the size of the droplets. The diffusion of solvent from the droplets is determined by the gradient of solvent concentration and the surface area through which diffusion takes place. The bigger the droplets are, the faster the linear velocity of the oil flow around the droplets becomes ($v_2/v_1 \sim R^2/(R-r)^2$, where R and r are the length scales of the channel and the droplet, respectively.

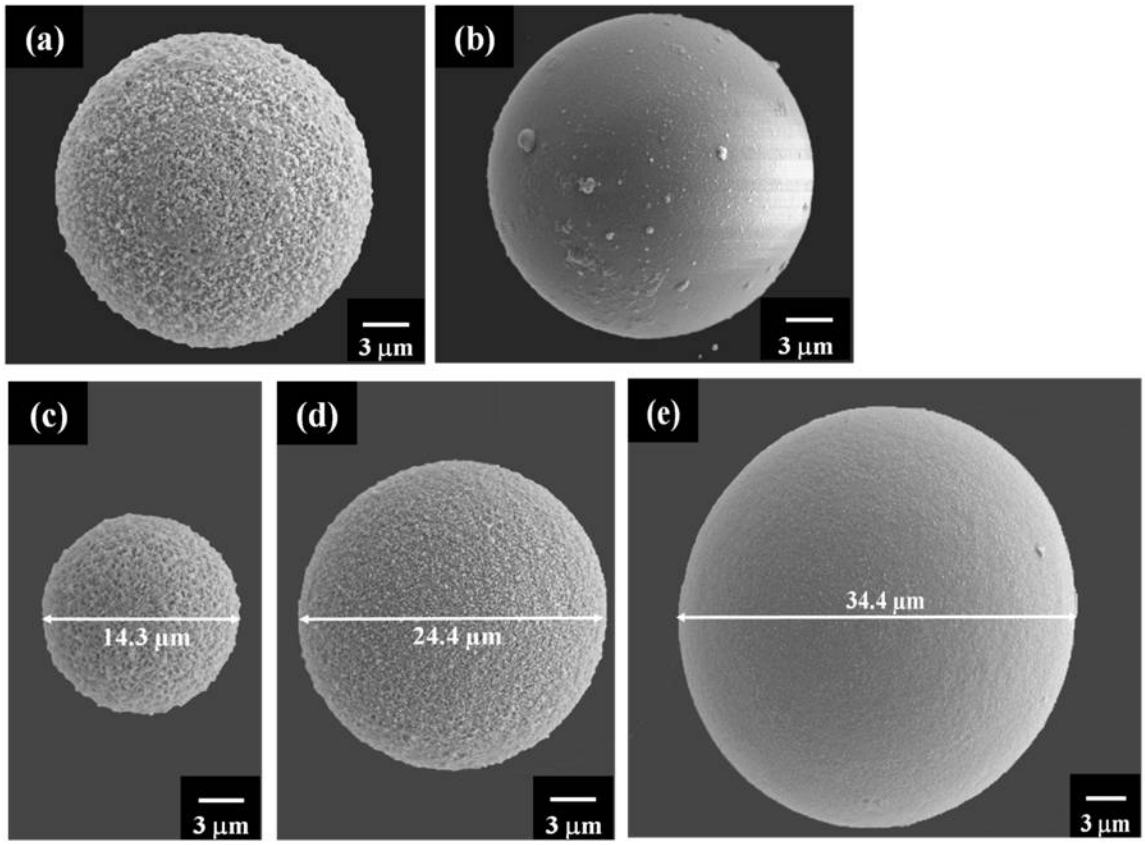

Figure 7.7 Control of the surface morphology of mesoporous silica microspheres: SEM images of mesoporous silica spheres generated in: (a) hexadecane and (b) mineral oil and with various size generated in hexadecane: (c) 14.3 μm, (d) 24.4 μm, and (e) 34.4 μm

The v_1 and v_2 are linear velocities of oils in the channel and around the droplet, respectively). In addition, the surface area becomes larger for bigger droplets. These two factors contribute to the faster diffusion of ethanol of the bigger droplets from the interfacial subphase to hexadecane, enabling faster solidification of mesostructured shell in the subphase as compared to the case of smaller droplets. Therefore, the process produces less corrugated surface morphology as shown in Figure 7.7 (c), (d), and (e).

7.3.4 Control of the size of OMS microspheres

The technology of microfluidics enables facile control over the size of droplets, thus controlling the size of OMS microspheres in a simple manner. It is known that the size of the droplets generated in a flow-focusing geometry are determined by balancing between viscous stress and interfacial stress on the interface as shown in the following equation,[148]

$$R \approx \frac{\gamma}{\eta U} h$$

where R is the terminal radius of the droplet, γ is the interfacial tension between the precursor solution and oil, η is the viscosity of continuous fluid, U is the velocity of the oil fluid at the orifice, and h is the size of the orifice in the microfluidic devices. Figure 7.8 (a) shows how the flow ratio of oil to precursor (Q_{oil}/Q_{pre}) affects the size of the precursor droplets. Increase in the flow ratio decreases droplet size down to about 25μm. Two different modes of droplet generation are observed depending on the relative flow rates: one dripping mode at lower Q_{oil}/Q_{pre} and the other jetting mode at higher Q_{oil}/Q_{pre}

as previously observed with W/O emulsion droplets in microchannels.[32] In the dripping mode, the size of the droplets linearly decreases as Q_{oil}/Q_{pre} increases while in the jetting mode, the size of the droplets decreases slightly. Another way to control the size of droplets is by changing the size of the orifice in the microfluidic devices as shown in Figure 7.8 (b). As one might expect, the larger the size of the orifice gap, the bigger the droplets become. The above relation indicates that the size of droplets can also be controlled by using oils with different viscosities. As predicted, indeed smaller droplets were made when hexadecane was replaced with mineral oil with higher viscosity under the same flow condition (data not shown here). Even though it was possible to control the size of droplets by adjusting the ratio of flow rate or by changing the size of the orifice gap, there was a limitation to how small droplets can be made in the microfluidic devices. The smallest droplets that could be made with the current method were about 20 μm in diameter.

In order to expand the range of controllable size of droplets, we have taken advantage of passive breakup of droplets in the microfluidic channels. This droplet breakup allows us to break a droplet into two pieces. Link and co-workers demonstrated experimentally passive breakup of water droplets in oil at symmetric and asymmetric T-junctions in microfluidic channels.[149] Later, De Menech developed a model on the breakup of droplets in a T-junction and showed that the critical capillary number for droplet breakup depends on the viscosity contrast.[150] The critical capillary number separating regions of breaking and non-breaking droplets is given by the function,[149, 150]

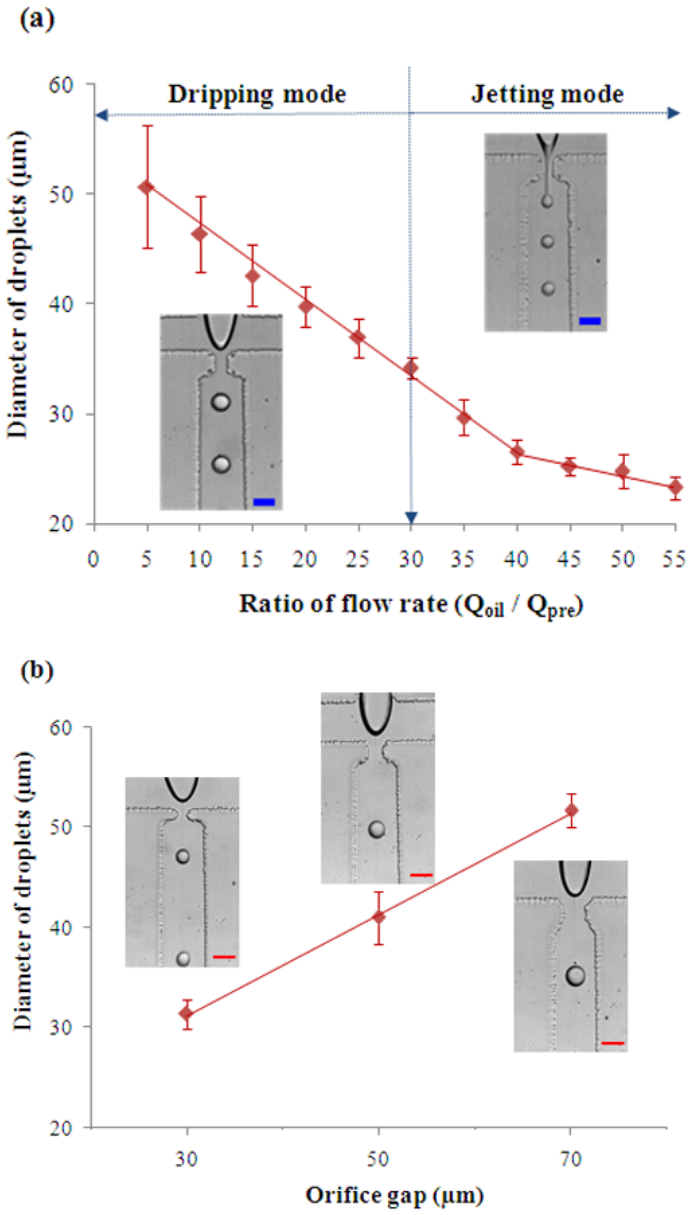

Figure 7.8 Control of the size of the droplets: (a) the effect of the relative flow ratio of oil to precursor phases (Q_{oil}/Q_{pre}, Q_{pre}=0.3μl/min) and (b) the effect of the size of the orifice gaps in the microfluidic devices. Scale bar is 50 μm

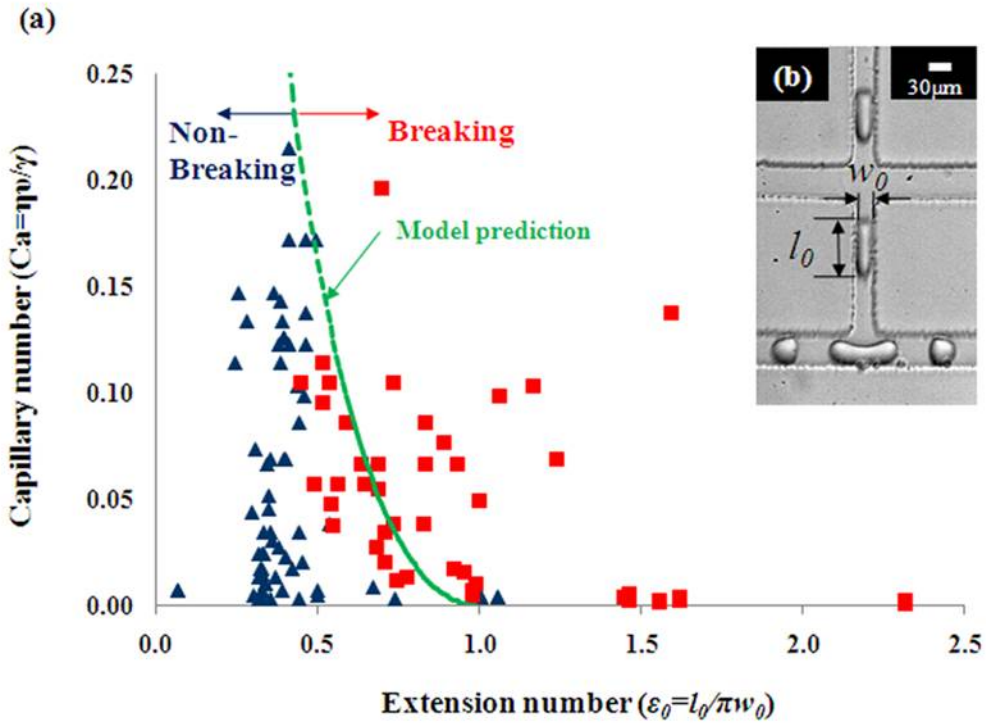

Figure 7.9 Control of size of droplets by symmetric breakup of droplets: critical condition for breaking or non-breaking of OMS precursor droplets as compared to the model prediction.[149] Inset is an optical micrograph showing the symmetric breakup of droplets at a T-junction

$$Ca_c = \alpha\varepsilon_0(1/\varepsilon_0^{2/3} - 1)^2 \quad (1)$$

where $\alpha(\lambda)$ is a constant which depends on the viscosity contrast ($\lambda=\eta_d/\eta_c$, η_d and η_c are viscosity of droplets and oil, respectively) and the details of the geometry.[150] ε_0 is the extension number defined as the ratio of length (l_0) to circumference ($\pi\omega_0$).[149] Since the principle of the breakup of droplets is the same, it is expected that the model should be applicable to the breakup of the ethanol-rich precursor droplets.

An optical micrograph (see inset in Figure 7.9) shows the extension, stretching, and breakup of the droplets in the microfluidic channels in the same way as the case of water in oil.[149] Figure 7.9 reveals, however, that the breakup behavior of ethanol-rich precursor droplets deviates slightly from the model prediction (dotted line). It is speculated that this is likely due to the uncertainty in our estimation of the capillary number and the roughness of the PDMS walls of our devices. For the estimation of the capillary numbers, the interfacial tension (λ) and viscosity (η_d) of the precursor solution were estimated using a simple mixing rule and the viscosity (η_c) of pure hexadecane was used. However, the interfacial tension and viscosity of the precursor solution may be different from the estimated values possibly due to the chemistry that takes place during the aging step of the precursor solution and in the microfluidic device. The viscosity of oil may also be altered due to the diffusion of ethanol into the oil phase. The roughness of the PDMS walls of our microfluidic devices (see inset Figure 7.9) may contribute to the deviated behavior from the model prediction as well. Droplets can be broken up more easily on the rough surface than the smoother surface.

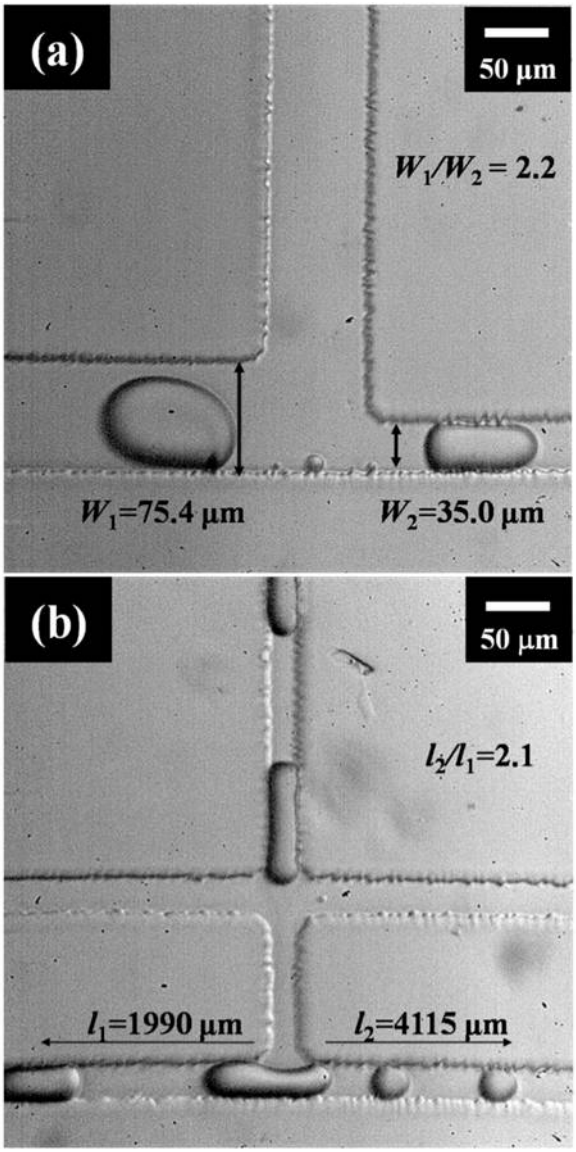

Figure 7.10 Control of size of droplets of asymmetric breakup of OMS droplets by adjusting (a) the relative width of the side channel (W_1/W_2 = 2.2) and (b) the relative length of the side channel (l_2/l_1 = 2.1)

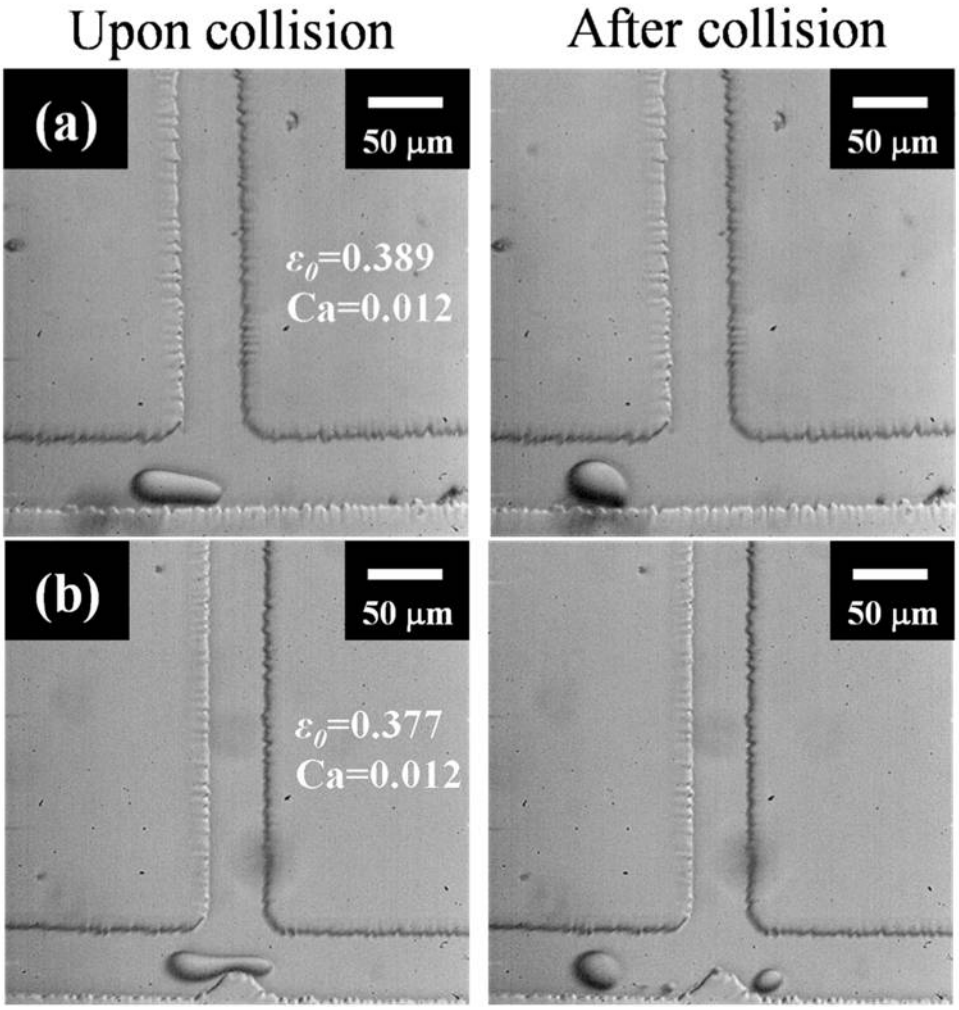

Figure 7.11 The effect of an obstacle constructed at the T-junction on the breakup of droplets; optical micrographs (a) show the droplets are not breaking upon collision at the T-junction and (b) show droplets are broken into two parts upon collision onto an obstacle at the T-junction. Note that the flow conditions are identical in both cases (i.e., with and without an obstacle)

We were also able to break the droplets asymmetrically as shown in Figure 7.10. The asymmetrical breakup of the drop was achieved by adjusting the relative of widths and lengths of the side channels as shown in Figure 7.10 (a) and (b), respectively. The ratio of the volumes of the droplets after breakup is proportional to the ratio of the volumetric flow rates of the fluids in the side channels ($V_1/V_2 \approx Q_1/Q_2$), which is proportional to the ratio of the widths of the side channels and inversely proportional to the ratio of the lengths of the side channels ($Q_1/Q_2 \approx W_1/W_2 \approx l_2/l_1$). The relative widths ($W_1/W_2$) of about 2.2 and the relative lengths (l_2/l_1) of about 2.1 of the side channels result in two asymmetric droplets with the volume ratios (V_1/V_2) of about 2.2 as shown in Figure 7.10.

We have also investigated the effect of an obstacle constructed at a T-junction for the breakup of droplets. Figure 7.11 shows that the droplets break at the sharp point of the obstacle and separated into two parts (Figure 7.11 (b)) even with the extension and capillary numbers that are not in the breaking regime (Figure 7.11 (a)).

7.4 Conclusion

In conclusion, we have developed a one-step *in situ* method, which we call microfluidic diffusion-induced self-assembly (DISA), for the synthesis of monodisperse OMS microspheres by combining microfluidic generations of uniform droplets and subsequent rapid solvent diffusion-induced self-assembly (DISA) *in situ* in the microfluidic devices. The OMS microspheres prepared by microfluidic DISA show very distinctive surface morphology (rough corrugated features in submicrometer scales) and

to the best of our knowledge, this type of surface morphology of OMS particles has not been reported previously. The surface morphology was controlled by adjusting the evaporation rate of ethanol. The size of OMS microspheres were controlled by simply changing microfluidic conditions such as relative flow rates of two immiscible solutions and flow focusing geometry. We have also demonstrated that it is possible to further control the size of OMS microspheres over the wider range by breaking up droplets in the microfluidic channel. The breakup of droplets allowed the droplets to break into smaller ones symmetrically and asymmetrically depending on the relative widths and the lengths of the side channels at the T-junctions. We believe that this microfluidic DISA method can offer new opportunities to make nanoporous materials with novel microstructures, such as Janus spheres, core-shell sphere, and hollow spheres, all of which can be applied to applications such as in energy, health and medicine, and sensing.

CHAPTER VIII

CONCLUSIONS AND FUTURE WORK

8.1 Conclusions

In this dissertation, we explored the novel synthesis of nanoporous materials and films with controlled microstructure. A simple and commercially viable synthesis method which we called "the micro-tiles-and-mortar method" has been demonstrated to prepare the *b*-oriented MFI silicalite-1 membranes with controlled microstructure such as thickness, orientation, and grain boundary. A novel synthesis, microfluidic DISA (Diffusion Induced Self Assembly) for the monodisperse OMS particles with controllable microstructure such as size, size distribution, and surface morphology has been also developed.

Our first objective in this regard was to demonstrate the ability to control the microstructure of the silicalite-1 films. This issue was addressed in Chapter IV. *b*-oriented silicalite-1 films were fabricated by passivating the flat facets of the seed crystals of the *b*-oriented seed layer, thus preventing the nucleation and growth of the crystals from the flat surface of the zeolite seed crystals while allowing the crystals to nucleate and grow in the plane. The thickness of the zeolite films was determined by that of the seed crystals. The density of grain boundary was controlled by varying the size of the seed crystals. Bigger crystals resulted in bigger single crystal domain, i.e., lower density of grain boundary. Also, the structure of grain boundaries was controlled by

preparing seed layers with two different sizes (larger seeds as tiles and smaller seeds as mortar) as well as by either activating their pores or not after secondary growth.

The second objective of this research was to study the effect of microstructure on permeation of xylene isomers through the silicalite-1 membranes. The optimization for the fabrication of silicalite-1 membranes on the porous supports was determined in Chapter V. The performance of silicalite-1 membranes was obtained by measuring permeance and selectivity of xylene isomers in Chapter VI. Though the micro-tiles-and-mortar method allowed synthesizing continuous *b*-oriented silicalite-1 films on the α-Al_2O_3 supports, permeation behavior and separation performance showed very different results compared to those of references. The difference in separation performance may be due to multiple factors, including a) formation of cracks and defects which provide non-zeolitic pathway; b) low density of intergrowth of seed crystals due to rather short time of secondary growth; and c) voids at the interface between Au passivation layer deposited on the side of seed crystals and newly grown silicalite-1 in the gaps. In Chapter V, we verified experimentally the reasons for the factors and suggested a couple of approaches to solve those issues.

The final objective was the focus of Chapter VII: synthesizing monodisperse OMS microspheres with controllable microstructure such as size, size distribution, and surface morphology. Here the novel synthesis that we called “microfluidic DISA” was demonstrated to make OMS microspheres combining DISA (Diffusion Induced Self Assembly) reaction of the OMS inorganic materials with microfluidic droplet technique. The size of OMS microspheres were controlled by simply changing microfluidic

conditions such as relative flow rates of two immiscible solutions and flow focusing geometry. We have also demonstrated that it is possible to further control the size of OMS microspheres over the wider range by breaking up droplets in the microfluidic channel. The breakup of droplets allowed the droplets to break into smaller ones symmetrically and asymmetrically depending on the relative widths and the lengths of the side channels at the T-junctions. The tunable surface morphology of OMS particles was obtained by controlling ethanol diffusion rate into oil phase.

8.2 Future work

Based on the results of this dissertation, there are suggestions and directions for the future work. For our synthesis method for the silicalite-1 membranes, the suggestions for the improvement of separation performance are discussed. Also, new synthesis-based studies are proposed by combining those two novel methods (the microfluidic DISA and the micro-tiles-and-mortar method) for the various applications.

8.2.1 Zeolite membranes

8.2.1.1 Passivation of the seed layer by PDMS stamping

In Chapter VI, *b*-oriented silicalite-1membranes by the micro-tiles-and-mortar method showed the low separation performance for the xylene isomers. It was explained that Au passivation layer deposited on the side of seed crystals could prevent interconnection between the growing crystals and may induce voids at the interface. In order to passivate only the surface of seed layer, PDMS stamping to transfer molecules

into target surface may be reliable approach. Hydrophobic silane coupling agent, for example, fluorosilicone ($CF_3(CF_2)_9C_2H_4Si(OCH_3)$) is used for the passivation of the silicalite-1 seed crystals. By controlling the thickness of fluorosilicone layer on the PDMS stamp, fluorosilicone could be transferred only to the surface of seed crystals. We demonstrated the feasibility of this method on the planar substrates in Chapter VI. It is worth to figure out the experiment conditions of PDMS stamping for transferring fluorosilicone to the surface of seed crystals on the porous supports.

8.2.1.2 The effect of grain boundary

One of the objectives of this dissertation was to study the effect of grain boundary on the separation performance. The density and structure of grain boundaries were controlled in Chapter IV. However, due to the low separation performance, effect of grain boundary is still questioned on the gas separation. If our new passivation method works, it is possible to fabricate b-oriented silicalite-1 membranes with controlled microstructure. Thus, it would be worth to study the effect of grain boundaries on the separation performance experimentally.

8.2.1.3 Tubular supports

For the industrial applications, it is much desirable to form zeolite membranes on the tubular supports. In this dissertation, α-Al_2O_3 disc was used for the porous supports. It would be interesting to try the micro-tiles-and-mortar method on the tubular supports. Particularly, it is critical to passivate the surface of seed crystals on the tubular supports.

Rolling the tubular supported seed layer on the PDMS stamps might be possible solution.

8.2.1.4 Micro-tiles-mortar method for other zeolites and porous materials

Among many zeolites, a few zeolites such as silicalite-1, zeolite A, zeolite Y, ZSM-5, faujasite, mordenite, ETS-10, and SAPO-34 have been reported as separation membranes by means of either in-situ method or secondary seeded growth. However, current methods have still many challenges to commercialize those membranes. One of many challenges is the process time. It normally took for days to prepare zeolite membranes, which make product cost high. Our method showed it only took a few hours. Thus it is also worth to apply our method for the preparation other zeolite membranes.

Recently a new class of porous crystalline materials has attracted much attention and made advances, so-called the Metal Organic Frameworks (MOFs), the Porous Coordination Polymers (PCPs), and the zeolitic imidazolate frameworks (ZIFs). These materials cover a much wider range of pore size than zeolites. The major studies of these materials have focused on dealing with synthesis for the applications of adsorption/separation and storage. The development of MOFs membranes has great potential for the important separations such as removal of CO_2, the separation hydrogen from other gases. There are two major hurdles to develop MOFs membranes; 1) seeding: more specifically coverage and interaction of seed crystals on the porous support; 2) intergrowth of seed crystals. In this dissertation, surface modification using high density of polymer linkers and sol-gel coating method for the zeolite seeding have been

thoroughly discussed. The micro-tiles-and-mortar method could provide high coverage and interaction of seed crystals on the supports. It would be interesting approach worth of the MOFs membranes.

8.2.2 Microfluidic DISA for OMS particles

8.2.2.1 Effect of microstructure

OMS microspheres with controllable microstructure have been demonstrated in this dissertation. Size, distribution of size and surface morphology were controlled by simply changing the microfluidic conditions. OMS microspheres have many interesting applications such as sensors, biomelecule delivery, and separation. When OMS particles are applied those applications, it would be interesting to study the effect of microstructure on the performance and efficiency. For instance, for the purpose of biomolecule immobilization, OMS particles with rougher surface would be desirable to attach bimolecules.

8.2.2.2 Janus particles

It is very interesting to make particles with two different properties, so-called Janus particles, for instance one side hydrophobic and the other side hydrophilic. Microfluidic synthesis allows polymer droplets to form biphasic Janus particles by introducing two different polymer precursor solutions into the flow focusing microfluidic device. However only polymer Janus particles have been reported so far.

In Chapter VII, monodisperse OMS microspheres were synthesized in the microfluidic device. Based on the findings from OMS synthesis, it would be worth for the first time to make organic-inorganic Janus particles in a microfluidic device. There would be a couple of hurdles to overcome: control of solvent diffusion rate versus polymerization rate, and mixing two precursor solutions at the interface. Once Janus droplets are generated at the flow focusing geometry, two precursor solutions in one droplet should change into solid particles maintaining interface. In order to do that, solvent diffusion rate in the inorganic solution and polymerization rate in the organic solution should be controlled.

REFERENCES

1. Baxter, J.; Bian, Z. X.; Chen, G.; Danielson, D.; Dresselhaus, M. S.; Fedorov, A. G.; Fisher, T. S.; Jones, C. W.; Maginn, E.; Kortshagen, U.; Manthiram, A.; Nozik, A.; Rolison, D. R.; Sands, T.; Shi, L.; Sholl, D.; Wu, Y. Y. *Energy & Environmental Science* **2009,** 2, 559-588.

2. Logar, N. Z.; Kaucic, V. *Acta Chimica Slovenica* **2006,** 53, 117-135.

3. Caro, J.; Noack, M. *Microporous and Mesoporous Materials* **2008,** 115, 215-233.

4. Meier, W. M.; Olson, D. H.; Baerlocher, C., *Atlas of Zeolite Structure Types*. Elsevier: Amsterdam, 1996.

5. Snyder, M. A.; Tsapatsis, M. *Angewandte Chemie-International Edition* **2007,** 46, 7560-7573.

6. Lai, Z. P.; Tsapatsis, M.; Nicolich, J. R. *Advanced Functional Materials* **2004,** 14, 716-729.

7. Jansen, J. C.; Vanrosmalen, G. M. *Journal of Crystal Growth* **1993,** 128, 1150-1156.

8. Wang, Z. B.; Yan, Y. S. *Chemistry of Materials* **2001,** 13, 1101-1107.

9. Wang, Z. B.; Yan, Y. S. *Microporous and Mesoporous Materials* **2001,** 48, 229-238.

10. Aguado, S.; McLeary, E. E.; Nijmeijer, A.; M., L.; Jansen, J. C.; Kapteijn, F. *Microporous and Mesoporous Materials* **2009,** 120, 165-169

11. Tricoli, V.; Sefcik, J.; McCormick, A. V. *Langmuir* **1997,** 13, 4193-4196.

12. Yan, Y. G.; Chaudhuri, S. R.; Sarkar, A. *Chemistry of Materials* **1996,** 8, 473-479.

13. Lai, Z. P.; Bonilla, G.; Diaz, I.; Nery, J. G.; Sujaoti, K.; Amat, M. A.; Kokkoli, E.; Terasaki, O.; Thompson, R. W.; Tsapatsis, M.; Vlachos, D. G. *Science* **2003,** 300, 456-460.

14. De Vos, D. E.; Dams, M.; Sels, B. F.; Jacobs, P. A. *Chemical Reviews* **2002,** 102, 3615-3640.

15. Xomeritakis, G.; Naik, S.; Braunbarth, C. M.; Cornelius, C. J.; Pardey, R.; Brinker, C. J. *Journal of Membrane Science* **2003,** 215, 225-233.

16. Brinker, C. J.; Ward, T. L.; Sehgal, R.; Raman, N. K.; Hietala, S. L.; Smith, D. M.; Hua, D. W.; Headley, T. J. *Journal of Membrane Science* **1993,** 77, 165-179.

17. Yamada, Y.; Nakamura, T.; Ishi, M.; Yano, K. *Langmuir* **2006,** 22, 2444-2446.

18. Scott, B. J.; Wirnsberger, G.; Stucky, G. D. *Chemistry of Materials* **2001,** 13, 3140-3150.

19. Torney, F.; Trewyn, B. G.; Lin, V. S. Y.; Wang, K. *Nature Nanotechnology* **2007,** 2, 295-300.

20. Slowing, II; Trewyn, B. G.; Giri, S.; Lin, V. S. Y. *Advanced Functional Materials* **2007,** 17, 1225-1236.

21. Lu, Y. F.; Fan, H. Y.; Doke, N.; Loy, D. A.; Assink, R. A.; LaVan, D. A.; Brinker, C. J. *Journal of the American Chemical Society* **2000,** 122, 5258-5261.

22. Yano, K.; Fukushima, Y. *Journal of Materials Chemistry* **2003,** 13, 2577-2581.

23. Rao, G. V. R.; Lopez, G. P.; Bravo, J.; Pham, H.; Datye, A. K.; Xu, H. F.; Ward, T. L. *Advanced Materials* **2002,** 14, 1301-1304.

24. Brinker, C. J.; Lu, Y. F.; Sellinger, A.; Fan, H. Y. *Advanced Materials* **1999,** 11, 579-585.

25. Yano, K.; Nakamura, T. *Chemistry Letters* **2006,** 35, 1014-1015.

26. Roh, K. H.; Yoshida, M.; Lahann, J. *Langmuir* **2007,** 23, 5683-5688.

27. Dendukuri, D.; Hatton, T. A.; Doyle, P. S. *Langmuir* **2007,** 23, 4669-4674.

28. Kim, J. W.; Utada, A. S.; Fernandez-Nieves, A.; Hu, Z. B.; Weitz, D. A. *Angewandte Chemie-International Edition* **2007,** 46, 1819-1822.

29. Shepherd, R. F.; Conrad, J. C.; Rhodes, S. K.; Link, D. R.; Marquez, M.; Weitz, D. A.; Lewis, J. A. *Langmuir* **2006,** 22, 8618-8622.

30. Nie, Z. H.; Li, W.; Seo, M.; Xu, S. Q.; Kumacheva, E. *Journal of the American Chemical Society* **2006,** 128, 9408-9412.

31. Oh, H. J.; Kim, S. H.; Baek, J. Y.; Seong, G. H.; Lee, S. H. *Journal of Micromechanics and Microengineering* **2006,** 16, 285-291.

32. Seo, M.; Nie, Z. H.; Xu, S. Q.; Mok, M.; Lewis, P. C.; Graham, R.; Kumacheva, E. *Langmuir* **2005,** 21, 11614-11622.

33. Roh, K. H.; Martin, D. C.; Lahann, J. *Nature Materials* **2005,** 4, 759-763.

34. Xu, S.; Nie, Z.; Seo, M.; Lewis, P.; Kumacheva, E.; Stone, H. A.; Garstecki, P.; Weibel, D. B.; Gitlin, I.; Whitesides, G. M. *Angewandte Chemie-International Edition* **2005,** 44, 3799-3799.

35. Utada, A. S.; Lorenceau, E.; Link, D. R.; Kaplan, P. D.; Stone, H. A.; Weitz, D. A. *Science* **2005,** 308, 537-541.

36. Xu, S. Q.; Nie, Z. H.; Seo, M.; Lewis, P.; Kumacheva, E.; Stone, H. A.; Garstecki, P.; Weibel, D. B.; Gitlin, I.; Whitesides, G. M. *Angewandte Chemie-International Edition* **2005,** 44, 724-728.

37. Jeong, W.; Kim, J.; Kim, S.; Lee, S.; Mensing, G.; Beebe, D. J. *Lab on a Chip* **2004,** 4, 576-580.

38. Anna, S. L.; Bontoux, N.; Stone, H. A. *Applied Physics Letters* **2003,** 82, 364-366.

39. Lai, Z.; Bonilla, G.; Diaz, I.; Nery, J. G.; Sujaoti, K.; Amat, M. A.; Kokkoli, E.; Terasaki, O.; Thompson, R. W.; Tsapatsis, M.; Vlachos, D. G. *Science* **2003,** 300, 456-460.

40. McLeary, E. E.; Jansen, J. C.; Kapteijn, F. *Microporous and Mesoporous Materials* **2006,** 90, 198-220.

41. Cheng, M.; Hu, G.; Tan, D.; Bao, X. *Microporous and Mesoporous Materials* **2001,** 50, 69-76.

42. Bein, T. *Chemistry of Materials* **1996,** 8, 1636-1653.

43. Wang, Z. B.; Wang, H. T.; Mitra, A.; Huang, L. M.; Yan, Y. S. *Advanced Materials* **2001,** 13, 746-749.

44. GRAAF, J. M. V. D. Permeation and Separation Properties of Supported Silicalite-1 Membranes. Aan De Technische Universiteit Delft, 1998.

45. Caro, J.; Noack, M.; Kolsch, P.; Schafer, R. *Microporous and Mesoporous Materials* **2000,** 38, 3-24.

46. Lin, Y. S.; Kumakiri, I.; Nair, B. N.; Alsyouri, H. *Separation and Purification Methods* **2002,** 31, 229-379.

47. Pradanos, P.; Palacio, L.; Hernandez, A.; Vilaseca, M.; Coronas, J.; Santamaria, J. *Boletin De La Sociedad Espanola De Ceramica Y Vidrio* **2004,** 43, 19-22.

48. Tavolaro, A.; Drioli, E. *Advanced Materials* **1999,** 11, 975-996.

49. Morigami, Y.; Kondo, M.; Abe, J.; Kita, H.; Okamoto, K. *Separation and Purification Technology* **2001,** 25, 251-260.

50. Suzuki, H. Composite membrane having a surface layer of an ultrathin film of cage-shaped zeolite and processes for production thereof. US 4699892, 1987.

51. Kong, C. L.; Lu, J. M.; Yang, J. H.; Wang, J. Q. *Journal of Membrane Science* **2006,** 285, 258-264.

52. Lin, X.; Chen, X. S.; Kita, H.; Okamoto, K. *Aiche Journal* **2003,** 49, 237-247.

53. Algieri, C.; Golemme, G.; Kallus, S.; Ramsay, J. D. F. *Microporous and Mesoporous Materials* **2001,** 47, 127-134.

54. Yan, Y. S.; Davis, M. E.; Gavalas, G. R. *Industrial & Engineering Chemistry Research* **1995,** 34, 1652-1661.

55. Geus, E. R.; Denexter, M. J.; Vanbekkum, H. *Journal of the Chemical Society-Faraday Transactions* **1992,** 88, 3101-3109.

56. Li, Y. S.; Chen, H. L.; Liu, J.; Yang, W. S. *Journal of Membrane Science* **2006,** 277, 230-239.

57. Xu, X. C.; Yang, W. S.; Liu, J.; Lin, L. W. *Microporous and Mesoporous Materials* **2001,** 43, 299-311.

58. Clet, G.; Gora, L.; Nishiyama, N.; Jansen, J. C.; van Bekkum, H.; Maschmeyer, T. *Chemical Communications* **2001**, 41-42.

59. Piera, E.; Salomon, M. A.; Coronas, J.; Menendez, M.; Santamaria, J. *Journal of Membrane Science* **1998,** 149, 99-114.

60. Dong, J. H.; Lin, Y. S. *Industrial & Engineering Chemistry Research* **1998,** 37, 2404-2409.

61. Poshusta, J. C.; Tuan, V. A.; Falconer, J. L.; Noble, R. D. *Industrial & Engineering Chemistry Research* **1998,** 37, 3924-3929.

62. Vilaseca, M.; Mateo, E.; Palacio, L.; Pradanos, P.; Hernandez, A.; Paniagua, A.; Coronas, J.; Santamaria, J. *Microporous and Mesoporous Materials* **2004,** 71, 33-37.

63. Miachon, S.; Landrivon, E.; Aouine, M.; Sun, Y.; Kumakiri, I.; Li, Y.; Prokopova, O. P.; Guilhaurne, N.; Giroir-Fendler, A.; Mozzanega, H.; Dalmon, J. A. *Journal of Membrane Science* **2006,** 281, 228-238.

64. Kolsch, P.; Venzke, D.; Noack, M.; Lieske, E.; Toussaint, P.; Caro, J. *Preparation and Testing of Silicalite-in-Metal-Membranes. In Zeolites and Related Microporous Materials: State of the Art* **1994**, 84, 1075-1082.

65. Vroon, Z.; Keizer, K.; Burggraaf, A. J.; Verweij, H. *Journal of Membrane Science* **1998,** 144, 65-76.

66. Yan, Y. S.; Davis, M. E.; Gavalas, G. R. *Journal of Membrane Science* **1997,** 123, 95-103.

67. Nomura, M.; Yamaguchi, T.; Nakao, S. *Industrial & Engineering Chemistry Research* **1997,** 36, 4217-4223.

68. Zhang, B. Q.; Wang, C.; Lang, L.; Cui, R. L.; Liu, X. F. *Advanced Functional Materials* **2008,** 18, 3434-3443.

69. Lovallo, M. C.; Gouzinis, A.; Tsapatsis, M. *Aiche Journal* **1998,** 44, 1903-1913.

70. Xomeritakis, G.; Nair, S.; Tsapatsis, M. *Microporous and Mesoporous Materials* **2000,** 38, 61-73.

71. Xomeritakis, G.; Gouzinis, A.; Nair, S.; Okubo, T.; He, M. Y.; Overney, R. M.; Tsapatsis, M. *Chemical Engineering Science* **1999,** 54, 3521-3531.

72. Xomeritakis, G.; Tsapatsis, M. *Chemistry of Materials* **1999,** 11, 875-878.

73. Motuzas, J.; Julbe, A.; Noble, R. D.; van der Lee, A.; Beresnevicius, Z. J. *Microporous and Mesoporous Materials* **2006,** 92, 259-269.

74. Huang, A. S.; Lin, Y. S.; Yang, W. S. *Journal of Membrane Science* **2004,** 245, 41-51.

75. Park, J. S.; Lee, G. S.; Lee, Y. J.; Park, Y. S.; Yoon, K. B. *Journal of the American Chemical Society* **2002,** 124, 13366-13367.

76. Ha, K.; Lee, Y. J.; Lee, H. J.; Yoon, K. B. *Advanced Materials* **2000,** 12, 1114-1117.

77. Choi, S. Y.; Lee, Y. J.; Park, Y. S.; Ha, K.; Yoon, K. B. *Journal of the American Chemical Society* **2000,** 122, 5201-5209.

78. Lee, J. S.; Ha, K.; Lee, Y. J.; Yoon, K. B. *Advanced Materials* **2005,** 17, (7), 837-841.

79. Lee, J. S.; Kim, J. H.; Lee, Y. J.; Jeong, N. C.; Yoon, K. B. *Angewandte Chemie-International Edition* **2007,** 46, 3087-3090.

80. Boudreau, L. C.; Kuck, J. A.; Tsapatsis, M. *Journal of Membrane Science* **1999,** 152, 41-59.

81. Kulak, A.; Lee, Y. J.; Park, Y. S.; Yoon, K. B. *Angewandte Chemie-International Edition* **2000,** 39, 950-953.

82. Kulak, A.; Park, Y. S.; Lee, Y. J.; Chun, Y. S.; Ha, K.; Yoon, K. B. *Journal of the American Chemical Society* **2000,** 122, 9308-9309.

83. Lee, S. R.; Son, Y. H.; Julbe, A.; Choy, J. H. *Thin Solid Films* **2006,** 495, 92-96.

84. Giannakopoulos, I. G.; Nikolakis, V. *Industrial & Engineering Chemistry Research* **2005,** 44, 226-230.

85. Nair, S.; Lai, Z. P.; Nikolakis, V.; Xomeritakis, G.; Bonilla, G.; Tsapatsis, M. *Microporous and Mesoporous Materials* **2001,** 48, 219-228.

86. Lassinantti, M.; Jareman, F.; Hedlund, J.; Creaser, D.; Sterte, J. *Catalysis Today* **2001,** 67, 109-119.

87. Pan, M.; Lin, Y. S. *Microporous and Mesoporous Materials* **2001,** 43, 319-327.

88. Lai, R.; Gavalas, G. R. *Microporous and Mesoporous Materials* **2000,** 38, 239-245.

89. Hedlund, J.; Noack, M.; Kolsch, P.; Creaser, D.; Caro, J.; Sterte, J. *Journal of Membrane Science* **1999,** 159, 263-273.

90. Cundy, C. S.; Cox, P. A. *Microporous and Mesoporous Materials* **2005,** 82, 1-78.

91. Weh, K.; Noack, M.; Sieber, I.; Caro, J. *Microporous and Mesoporous Materials* **2002,** 54, 27-36.

92. Tsai, T. G.; Shih, H. C.; Liao, S. J.; Chao, K. J. *Microporous and Mesoporous Materials* **1998,** 22, 333-341.

93. Coutinho, D.; Losilla, J. A.; Balkus, K. J. *Microporous and Mesoporous Materials* **2006,** 90, 229-236.

94. Motuzas, J.; Julbe, A.; Noble, R. D.; Guizard, C.; Beresnevicius, Z. J.; Cot, D. *Microporous and Mesoporous Materials* **2005,** 80, 73-83.

95. Tang, Z.; Kim, S. J.; Gu, X. H.; Dong, J. H. *Microporous and Mesoporous Materials* **2009,** 118, 224-231.

96. Chen, X. X.; Yan, W. F.; Shen, W. L.; Yu, J. H.; Cao, X. J.; Xu, R. R. *Microporous and Mesoporous Materials* **2007,** 104, 296-304.

97. Au, L. T. Y.; Mui, W. Y.; Lau, P. S.; Ariso, C. T.; Yeung, K. L. *Microporous and Mesoporous Materials* **2001,** 47, 203-216.

98. Lovallo, M. C.; Tsapatsis, M. *Aiche Journal* **1996,** 42, 3020-3029.

99. Choi, J.; Jeong, H. K.; Snyder, M. A.; Stoeger, J. A.; Masel, R. I.; Tsapatsis, M. *Science* **2009,** 325, 590-593.

100. Nelson, P. H.; Tsapatsis, M.; Auerbach, S. M. *Journal of Membrane Science* **2001,** 184, 245-255.

101. Bonilla, G.; Tsapatsis, M.; Vlachos, D. G.; Xomeritakis, G. *Journal of Membrane Science* **2001,** 182, 103-109.

102. Xomeritakis, G.; Lai, Z. P.; Tsapatsis, M. *Industrial & Engineering Chemistry Research* **2001,** 40, 544-552.

103. Caro, J.; Noack, M.; Richtermendau, J.; Marlow, F.; Petersohn, D.; Griepentrog, M.; Kornatowski, J. *Journal of Physical Chemistry* **1993,** 97, 13685-13690.

104. Karger, J. *Journal of Physical Chemistry* **1991,** 95, 5558-5560.

105. Choi, J.; Ghosh, S.; King, L.; Tsapatsis, M. *Adsorption-Journal of the International Adsorption Society* **2006,** 12, 339-360.

106. Barrer, R. M. *Journal of the Chemical Society-Faraday Transactions* **1990,** 86, 1123-1130.

107. Xiao, J. R.; Wei, J. *Chemical Engineering Science* **1992,** 47, 1123-1141.

108. Nishiyama, N.; Gora, L.; Teplyakov, V.; Kapteijn, F.; Moulijn, J. A. *Separation and Purification Technology* **2001,** 22-3, 295-307.

109. Reid, R. C.; Prausnitz, J. M.; Poling, B.E. *The properties of gases and liquids forth edition,* McGraw-Hill, New York, 1987.

110. Cornelius, C. J. *Physical and gas permeation properties of a series of novel hybrid inorganic-organic composites based on a synthesized fluorinated polyimide,* Virginia Polytechnic Institute and State University, Blacksburg, 2000.

111. Lide, D. R., *CRC Handbook of Chemistry and Physics 89th edition*. 89th ed. CRC Press, Florida, 2008.

112. Ha, K.; Lee, Y. J.; Lee, H. J.; Yoon, K. B. *Advanced Materials* **2000,** 12, 1114-1117.

113. Bonilla, G.; Diaz, I.; Tsapatsis, M.; Jeong, H.-K.; Lee, Y. J.; Vlachos, D. G. *Chem. Mater.* **2004,** 16, 5697-5705.

114. Choi, J.; Ghosh, S.; Lai, Z. P.; Tsapatsis, M. *Angewandte Chemie-International Edition* **2006,** 45, 1154-1158.

115. Alfaro, S.; Arruebo, M.; Coronas, J.; Menendez, M.; Santamaria, J. *Microporous and Mesoporous Materials* **2001,** 50, 195-200.

116. Jeong, H. K.; Lai, Z. P.; Tsapatsis, M.; Hanson, J. C. *Microporous and Mesoporous Materials* **2005,** 84, 332-337.

117. Dong, J. H.; Lin, Y. S.; Hu, M. Z. C.; Peascoe, R. A.; Payzant, E. A. *Microporous and Mesoporous Materials* **2000,** 34, 241-253.

118. Madou, M. J., *Fundamentals of Microfabrication: The Science of Miniaturization*. 2nd ed.; CRC Press: New York, 2002.

119. Coronas, J.; Falconer, J. L.; Noble, R. D. *Aiche Journal* **1997,** 43, 1797-1812.

120. Parvelescu, V.; Tablet, C.; Su, B. L. *Colloids and Surfaces a-Physicochemical and Engineering Aspects* **2007,** 300, 94-98.

121. van den Berg, A. W. C.; Gora, L.; Jansen, J. C.; Makkee, M.; Maschmeyer, T. *Journal of Membrane Science* **2003,** 224, 29-37.

122. Lai, R.; Yan, Y. S.; Gavalas, G. R. *Microporous and Mesoporous Materials* **2000,** 37, 9-19.

123. Liu, Q.; Noble, R. D.; Falconer, J. L.; Funke, H. H. *Journal of Membrane Science* **1996,** 117, 163-174.

124. Sano, T.; Yanagishita, H.; Kiyozumi, Y.; Mizukami, F.; Haraya, K. *Journal of Membrane Science* **1994,** 95, 221-228.

125. Cejka J.; Bekkum, H. V.; Corma, A.; Schuth, F. *Introduction to zeolite science and practice volume 168 3rd edition*. Elsevier Science B.V., Maryland Heights 2007.

126. Zhang, B. Q.; Zhou, M.; Liu, X. F. *Advanced Materials* **2008,** 20, (11), 2183-2189.

127. Trueba, M.; Trasatti, S. P. *European Journal of Inorganic Chemistry* **2005**, 3393-3403.

128. Xu, P.; Mujumdar, A. S.; Yu, B. *Drying Technology* **2009,** 27, 636-652.

129. Peng, F. B.; Lu, L. Y.; Sun, H. L.; Wang, Y. Q.; Liu, J. Q.; Jiang, Z. Y. *Chemistry of Materials* **2005,** 17, 6790-6796.

130. Sakai, H.; Tomita, T.; Takahashi, T. *Separation and Purification Technology* **2001,** 25, 297-306.

131. Baertsch, C. D.; Funke, H. H.; Falconer, J. L.; Noble, R. D. *Journal of Physical Chemistry* **1996,** 100, 7676-7679.

132. Burggraaf, A. J.; Vroon, Z.; Keizer, K.; Verweij, H. *Journal of Membrane Science* **1998,** 144, 77-86.

133. Keizer, K.; Burggraaf, A. J.; Vroon, Z.; Verweij, H. *Journal of Membrane Science* **1998,** 147, 159-172.

134. Lai, Z. P.; Tsapatsis, M. *Industrial & Engineering Chemistry Research* **2004,** 43, 3000-3007.

135. Wegner, K.; Dong, J. H.; Lin, Y. S. *Journal of Membrane Science* **1999,** 158, 17-27.

136. Gualtieri, M. L.; Anderson, C.; Jareman, F.; Hedlund, J.; Gualtieri, A. F.; Leoni, M.; Meneghini, C. *Journal of Membrane Science* **2007,** 290, 95-104.

137. Anantatmula, R. P.; Johnson, A. A.; Gupta, S. P.; Horylev, R. J. *Journal of Electronic Materials* **1975,** 4, 445-463.

138. Bagshaw, S. A.; Prouzet, E.; Pinnavaia, T. J. *Science* **1995,** 269, 1242-1244.

139. Huo, Q. S.; Margolese, D. I.; Ciesla, U.; Feng, P. Y.; Gier, T. E.; Sieger, P.; Leon, R.; Petroff, P. M.; Schuth, F.; Stucky, G. D. *Nature* **1994,** 368, 317-321.

140. Kresge, C. T.; Leonowicz, M. E.; Roth, W. J.; Vartuli, J. C.; Beck, J. S. *Nature* **1992,** 359, 710-712.

141. Lu, Y. F.; Fan, H. Y.; Stump, A.; Ward, T. L.; Rieker, T.; Brinker, C. J. *Nature* **1999,** 398, 223-226.

142. Andersson, N.; Kronberg, B.; Corkery, R.; Alberius, P. *Langmuir* **2007,** 23, 1459-1464.

143. Carroll, N. J.; Rathod, S. B.; Derbins, E.; Mendez, S.; Weitz, D. A.; Petsev, D. N. *Langmuir* **2008,** 24, 658-661.

144. Brinker, C. J. *Mrs Bulletin* **2004,** 29, 631-640.

145. Xia, Y. N.; Whitesides, G. M. *Angewandte Chemie-International Edition* **1998,** 37, 551-575.

146. Umbanhowar, P. B.; Prasad, V.; Weitz, D. A. *Langmuir* **2000,** 16, 347-351.

147. Matsuda, H.; Ochi, K. *Fluid Phase Equilibria* **2004,** 224, 31-37.

148. Cristini, V.; Tan, Y. C. *Lab on a Chip* **2004,** 4, 257-264.

149. Link, D. R.; Anna, S. L.; Weitz, D. A.; Stone, H. A. *Physical Review Letters* **2004,** 92, 054503-1-054053-4.

150. De Menech, M. *Physical Review E* **2006,** 73, 031505-1-031505-9.

VITA

Name: In Ho Lee

Address: The Dow Chemical Company
455 Forest Street
Marlborough, MA 01752

Email Address: leeih999@gmail.com

Education: B.S., Chemical Engineering, Sogang University, 1999
M.S., Chemical Engineering, Sogang University, 2001
Ph.D., Chemical Engineering, Texas A&M University, 2010